technische universität
dortmund

Arbeit zur Erlangung des akademischen Grades
Master of Science

Flavour-tagging and particle-identification calibration in key measurements with electrons at LHCb

Alex Seuthe
geboren in Hagen

2017

Lehrstuhl für Experimentelle Physik V
Fakultät Physik
Technische Universität Dortmund

Erstgutachter:	Dr. Johannes Albrecht
Zweitgutachter:	Prof. Dr. Bernhard Spaan
Abgabedatum:	29. September 2017

Abstract

The CP-violation observables C and S are measured in the study of decay-time-dependent CP violation in the $B^0 \to J/\psi K^0_S$ and $B^0 \to \psi(2S) K^0_S$ decays, where the J/ψ candidate is reconstructed from two electrons and the $\psi(2S)$ candidate from two muons. The analysis uses data recorded by the LHCb experiment at centre-of-mass energies of 7 and 8 TeV corresponding to an integrated luminosity of $3\,\mathrm{fb}^{-1}$ and was recently brought to publication [arXiv: 1709.03944]. This thesis provides the underlying flavour-tagging calibration for the $B^0 \to J/\psi K^0_S$ decay, which uses $B^+ \to J/\psi K^+$ and $B^0 \to J/\psi K^{*0}$ decays, where the J/ψ candidates are reconstructed from two electrons. It is the first systematic flavour-tagging study with electron modes included at LHCb.

Additionally, first studies with particle-identification (PID) samples with electrons of the years 2015 and 2016 are performed. An algorithm, which was used for the PID calibration in the recently published LHCb measurement [JHEP 08 (2017) 055] of the lepton flavour universality ratio R_{K^*} is implemented and validated. The algorithm determines regions of constant efficiency in the PID-calibration samples under the requirement of minimal systematic uncertainties.

Contents

1 Introduction

The Large Hadron Collider (LHC) is the world's largest and most powerful particle accelerator. It is operated by the European Organization of Nuclear Research (CERN) near Geneva, Switzerland. One of the four large experiments located at the LHC is the Large Hadron Collider beauty (LHCb) experiment, which searches for physics beyond the Standard Model (SM) of particle physics with precision measurements in the flavour sector. The LHCb experiment is designed to study decays of hadrons that contain b- and c-quarks. Two of its experimental main fields are the measurement of rare decays and high precision measurements of CP-violation parameters of the SM. Because of the detector's excellent muon reconstruction many studies focus on decays with muons in the final state. However, the inclusion of electron modes allows for an extension of the LHCb physics programme. This thesis provides first studies of the LHCb experiment of the flavour-tagging calibration with electrons in general and first studies of the particle-identification (PID) calibration with electron samples recorded in the years 2015 and 2016.

In studies of decay-time-dependent CP-violation with B mesons the knowledge of the initial flavour of the B meson is essential. Whether the B meson consists of a b- or a $\overline{b}$-quark at production time is determined with the flavour tagging at LHCb. These algorithms additionally provide a probability of mis-classification. As the tagging decision and the probability of a mis-classification is a direct input to the CP-violation measurement, the flavour tagging needs a precise calibration. The CP-violation observables C and S are measured in the study of decay-time-dependent CP violation in the $B^0 \to J/\psi K^0_S$ and $B^0 \to \psi(2S) K^0_S$ decays, where the J/ψ candidate is reconstructed from two electrons and the $\psi(2S)$ candidate from two muons. The analysis uses data recorded by the LHCb experiment at centre-of-mass energies of 7 and 8 TeV corresponding to an integrated luminosity of $3\,\text{fb}^{-1}$ and was recently brought to publication [1]. This thesis provides the underlying flavour-tagging calibration for the $B^0 \to J/\psi K^0_S$ decay, which uses $B^+ \to J/\psi K^+$ and $B^0 \to J/\psi K^{*0}$ decays, where the J/ψ candidates are reconstructed from two electrons. It is the first systematic flavour-tagging study with electron modes included at LHCb.

The PID is a main requirement of LHCb physics analyses, that search for physics beyond the SM in rare decays. Recent studies measured hints of deviations from the SM in lepton flavour universality (LFU) ratios like $R_{K^*} = \frac{\mathcal{B}(B \to K^* \mu^+ \mu^-)}{\mathcal{B}(B \to K^* e^+ e^-)}$ [2, 3]. Here, the PID is essentially needed to distinguish between the different final states of the decays. As the PID variables are not well described in simulation, a calibration with dedicated calibration samples has to be performed. It allows for their correct usage in the training of multivariate classifiers and for the determination of PID efficiencies. This thesis provides first studies with PID samples with electrons of the years 2015 and 2016.

2 The Standard Model of particle physics

The Standard Model of particle physics (SM) is a relativistic quantum field theory, that describes the fundamental particles and interactions. Particles are created and annihilated through fields $\phi(x)$ and their dynamics are described by the Lagrangian $\mathcal{L}(\phi(x), \partial_\mu \phi(x))$ [4]. The theory allows for high precision predictions and is in excellent agreement with current experimental results. However it does not include the theory of gravity and bears open questions about the nature of dark matter, dark energy, the hierarchy of particle masses [5], and the extent of the baryon asymmetry in the universe [6]. Deviations from the SM could be observed experimentally in direct searches with high energy experiments. It is also possible to perform searches for effects of physics beyond the SM with indirect searches with high precision experiments like the LHCb detector.

The elementary constituents of matter are fermions with half-integer spins. The fundamental forces, which are described by the SM are the electromagnetic force, the weak force, and the strong force. They are mediated by particles with integer spin, called bosons. The elementary particles with their masses, electromagnetic charges and spins can be found in Fig. 2.1. The fundamental fermions of the SM are represented by six leptons and six quarks and their associated antiparticles, where antiparticles have the same mass but opposite charges. The leptons can be divided into three families, where the charged leptons are the electron, the muon and the tau. To each of them a neutral neutrino (ν_e, ν_μ, ν_τ) is assigned. Similarily, the quark sector can be subdivided into three families as can be seen in Fig. 2.1. The doublets are formed by the up- (u) and down-quark (d), the charm- (c) and strange-quark (s), and the top- (t) and beauty-quark (b). The antiparticles of the six quarks have the same masses but inverted quantum numbers. The group of up-type quarks has an electromagnetic charge of $+\frac{2}{3}$e and consists of the u-, c-, and t-quark. Here, e is the elementary charge. The group of down-type quarks with an electromagnetic charge of $-\frac{1}{3}$e contains the d-, s-, and b-quark. Quarks carry colour charge, with the possible colours red, green, and blue. Antiquarks carry anticolours, respectively. No isolated colour charges occur in nature, thus quarks only exist in the form of composite particles, called hadrons. Quark systems consisting of a quark and an antiquark ($q\bar{q}$) are named mesons and three-quark systems (qqq or $\overline{qqq}$) are called baryons. Tetraquarks are quark systems with four valence quarks. Recently, the LHCb collaboration published results consistent with pentaquarks [7], which consist of four quarks and an antiquark. Quarks can couple to the electroweak and the strong interaction. The Higgs boson is the quantum excitation of the Higgs field and interacts with all massive particles. The Higgs mechanism [8] is responsible for the masses of the $W^\pm$ and the Z^0 boson.

The SM describes fundamental forces and their force carriers. The electromagnetic, weak, and strong force represent three of the four fundamental forces of nature. A description of gravity is not included in the SM. The massless photon γ is the force carrier of the

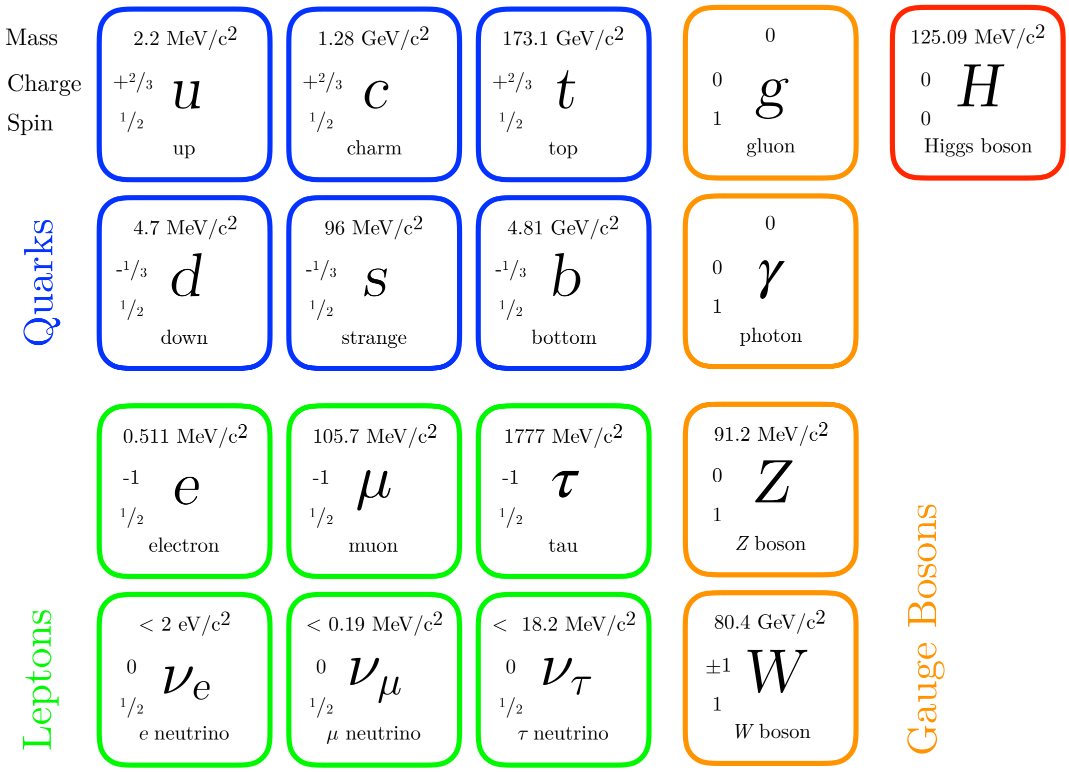

Figure 2.1: Fundamental particles of the Standard Model with masses, electromagnetic charges, and spins with values from Ref. [9].

electromagnetic force. It couples to the electromagnetic charge and thus neutrinos as the only chargeless elementary fermions are not affected by the electromagnetic force. Eight massless gluons, which are coupling to the colour charge, medidate the strong force. The quarks are the only fermions that carry colour charge and thus couple to the strong force. Because gluons carry a colour and an anticolour, gluon-gluon coupling is possible. The electroweak interaction is the unified description of the electromagnetic and weak interaction. The weak interaction is mediated by the W^+, W^-, and Z^0 bosons, which couple to the weak isospin, as a quantum number relating to the weak interaction. In contrast to the other bosons they are massive and couple to all twelve fermions. The weak interaction couples to the left-handed doublets of the quarks and leptons. In contrast to the electromagnetic and strong force the weak interaction does not conserve the quark flavour. Thus, transitions between up-type and down-type quarks under emission of a $W^\pm$ boson can occur. Under the assumption of massless neutrinos the weak eigenstates of the charged leptons can easily be transformed to their mass eigenstates. In the quark sector this is not possible for both quark types. Conventionally the up-type quarks are chosen such that the Cabibbo-Kobayashi-Maskawa (CKM) [10] quark mixing matrix V_{CKM} transforms the eigenstates of the weak interaction, d', s', b', into the mass eigenstates, d, s, b, as can be seen in Eq. (2.1). The CKM matrix is a complex and unitary matrix with three rows and three columns. The squared entries $|V_{\mathrm{ij}}|^2$ describe the probability of the transition from the quark q_{j} to the quark q_{i} [11], with

$$\begin{pmatrix} d \\ s \\ b \end{pmatrix} = \begin{pmatrix} V_{\mathrm{ud}} & V_{\mathrm{us}} & V_{\mathrm{ub}} \\ V_{\mathrm{cd}} & V_{\mathrm{cs}} & V_{\mathrm{cb}} \\ V_{\mathrm{td}} & V_{\mathrm{ts}} & V_{\mathrm{tb}} \end{pmatrix} \begin{pmatrix} d' \\ s' \\ b' \end{pmatrix} . \tag{2.1}$$

Transitions within quarks families are more probable than changes between families. This is represented by the dimension of the CKM matrix entries, where the diagonal elements have a greater nominal value than the off-diagonal elements.

2.1 *CP* violation

The SM of particle physics is based on two types of symmetries. On the one hand continuous gauge symmetries are the foundation of the gauge bosons as generators of gauge transformations in the SM formalism. On the other hand there are three fundamental types of discrete symmetries in the SM. The parity operator P describes a space inversion. The charge conjugation operator C changes the sign of all additive quantum numbers and thus transforms a particle to its antiparticle. The time reversal operator T inverts the sign of the time component. Because *CPT* is conserved for all interactions, particles and antiparticles have the same masses and lifetimes. The weak interaction violates parity [12] as well as the combination *CP*, which was reported by Fitch and Cronin in 1964 for neutral kaons [13]. The effects of *CP* asymmetry that can be observed in current particle physics experiments are well described by the SM. However, its description is not able to explain the global baryon asymmetry in the visible universe [6]. In 2001, *CP* violation in neutral B meson decays was reported by the BaBar and Belle collaborations [14, 15]. In contrast to the kaon system, where the effects of *CP* violation are small in relatively common decays, the effects of *CP* violation tend to be large for rare B decays [11].

In the following, the mixing of B mesons and *CP* violation are introduced. As shown before, the mass eigenstates and the eigenstates of the weak interaction, also called flavour eigenstates, are not identical in the quark sector. This is also the case for composed particles like B mesons, for example for the B^0 ($\bar{b}d$) and its antiparticle $\overline{B}^0$ ($b\bar{d}$). The time evolution of a two-particle system consisting of a B^0 and a $\overline{B}^0$ meson is described by the Schrödinger equation

$$\mathrm{i}\frac{d}{dt}\begin{pmatrix} B^0 \\ \overline{B}^0 \end{pmatrix} = \mathcal{H}\begin{pmatrix} B^0 \\ \overline{B}^0 \end{pmatrix} = (M - \frac{\mathrm{i}}{2}\Gamma)\begin{pmatrix} B^0 \\ \overline{B}^0 \end{pmatrix} , \tag{2.2}$$

where M and Γ are hermitian matrices as part of the Hamiltonian $\mathcal{H}$ [16]. As a result of the *CPT* theorem, the matrix elements obey the condition $m_{11} = m_{22}$ and $\Gamma_{11} = \Gamma_{22}$. The eigenvalues of the diagonalized matrix are $\mu_{1,2} = m_{1,2} - \frac{\mathrm{i}}{2}\Gamma_{1,2}$ with the corresponding masses $m_{1,2}$ and decay widths $\Gamma_{1,2}$. Thus it is possible to define the mass eigenstates B_L

and B_H in the B^0 system with the masses, m_L and m_H, and decay widths Γ_L and Γ_H [17] as

$$|B_H\rangle = p\,|B^0\rangle - q\,|\overline{B}^0\rangle \text{ and } |B_L\rangle = p\,|B^0\rangle + q\,|\overline{B}^0\rangle \ , \tag{2.3}$$

with the normalization condition $|p|^2 + |q|^2 = 1$ for the parameters p and q. The differences of the masses and the decay widths are defined as

$$\Delta m = m_\mathrm{H} - m_\mathrm{L} \text{ and } \Delta\Gamma = \Gamma_\mathrm{H} - \Gamma_\mathrm{L} \, . \tag{2.4}$$

The time evolution of the flavour eigenstates with the operator $g_\pm = \mathrm{e}^{-\mu_\mathrm{H} t} \pm \mathrm{e}^{-\mu_\mathrm{L} t}$ is

$$|B^0(t)\rangle = \frac{1}{2}\,|B^0\rangle\, g_+ - \frac{q}{2p}\,|\overline{B}^0\rangle\, g_- \, , \tag{2.5a}$$

$$|\overline{B}^0(t)\rangle = \frac{1}{2}\,|\overline{B}^0\rangle\, g_- - \frac{q}{2p}\,|\overline{B}^0\rangle\, g_+ \, . \tag{2.5b}$$

The probability of a B^0 meson produced a the time $t = 0$ to oscillate in a $\overline{B}^0$ meson at the time t can be calculated as

$$|\langle \overline{B}^0 | B^0(t)\rangle|^2 = \frac{1}{4}\left|\frac{q}{p}\right|^2 \left(\mathrm{e}^{-\Gamma_\mathrm{H} t} + \mathrm{e}^{-\Gamma_\mathrm{L} t} - 2\mathrm{e}^{\frac{1}{2}(\Gamma_\mathrm{H}+\Gamma_\mathrm{L})t} \cos\left(\Delta m t\right)\right) \, . \tag{2.6}$$

The lowest order Feynman diagrams of this oscillation process are illustrated in Fig. 2.2.

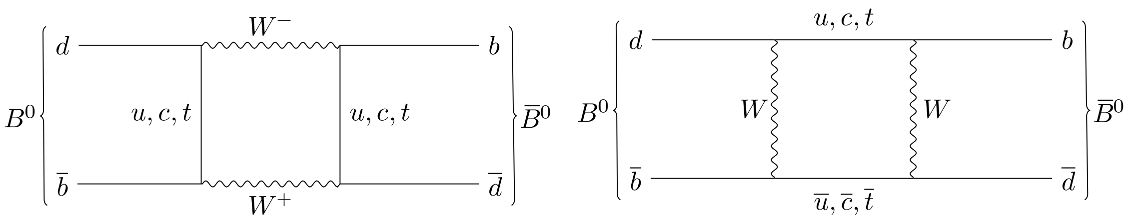

Figure 2.2: Lowest order Feynman diagrams of the oscillation of neutral B mesons.

Without *CP* violation and under the approximation $\Gamma_\mathrm{H} \approx \Gamma_\mathrm{L}$ this results in a mixing asymmetry

$$\begin{aligned}\mathcal{A}_\mathrm{mix} &= \frac{(\Gamma(B^0(t)\to B^0) + \Gamma(\overline{B}^0(t)\to\overline{B}^0)) - (\Gamma(\overline{B}^0(t)\to B^0) + \Gamma(B^0(t)\to\overline{B}^0))}{(\Gamma(B^0(t)\to B^0) + \Gamma(\overline{B}^0(t)\to\overline{B}^0)) + (\Gamma(\overline{B}^0(t)\to B^0) + \Gamma(B^0(t)\to\overline{B}^0))} \\ &= \frac{N_\mathrm{unmixed}(t) - N_\mathrm{mixed}(t)}{N_\mathrm{unmixed}(t) + N_\mathrm{mixed}(t)} = \cos\left(\Delta m t\right) \, .\end{aligned} \tag{2.7}$$

Here, $N_{\text{unmixed}}(t)$ is the number of B mesons not oscillated at the time t, and $N_{\text{mixed}}(t)$ is the number of B mesons where the oscillation at time t has already occured.

To introduce *CP* violation to this formalism it is useful to define the decay amplitudes as follows

$$\mathcal{A}_f = \langle f|T|B^0\rangle \, , \, \mathcal{A}_{\overline{f}} = \langle \overline{f}|T|B^0\rangle \, , \, \overline{\mathcal{A}}_f = \langle f|T|\overline{B}^0\rangle \, , \, \overline{\mathcal{A}}_{\overline{f}} = \langle \overline{f}|T|\overline{B}^0\rangle \, , \tag{2.8}$$

where the matrix T describes the transition between the B meson and the final states f or $\overline{f}$, where $\overline{f}$ is the charge conjugation of f. *CP* violation can be classified into three types. In the case of direct *CP* violation or *CP* violation in decay, the decay amplitudes of B^0 and $\overline{B}^0$ differ, thus $|\mathcal{A}_f| \neq |\overline{A}_{\overline{f}}|$ and $|\mathcal{A}_{\overline{f}}| \neq |\overline{A}_f|$. For indirect *CP* violation or *CP* violation in mixing, the transition probabilities $B^0 \to \overline{B}^0$ and $\overline{B}^0 \to B^0$ are different, thus $|\langle \overline{B}^0|B^0(t)\rangle| \neq |\langle B^0|\overline{B}^0\rangle|$ and $|\frac{q}{p}| \neq 1$. The third type of *CP* violation is *CP* violation in the interference of decay and decay after mixing, where in general $\langle f|T|B^0(t)\rangle \neq \langle \overline{f}|T|\overline{B}^0(t)\rangle$, when the direct $B^0 \to f$ decay interferes with the mixing $B^0 \to \overline{B}^0$, even without the existence of direct or indirect *CP* violation. In the SM, *CP* violation is described by the complex phase of the CKM matrix, as the weak force does not couple to flavour eigenstates. Thus asymmetries between particles and antiparticles occur. Nine conditions for the matrix elements follow from the unitarity of the CKM matrix with $V_{\text{CKM}}^{\dagger} V_{\text{CKM}} = 1$. Three of these equations can be written as

$$\sum_{i \in \{u,c,t\}} |V_{ij}|^2 = 1 \, , \, j \in \{d, s, b\} \, . \tag{2.9}$$

The six other equations can be interpreted as triangles in the complex plane, with their area as a measure of *CP* violation. The most common of these unitarity triangles is described by the condition

$$V_{ud} V_{ub}^* + V_{cd} V_{cb}^* + V_{td} V_{tb}^* = 0 \, . \tag{2.10}$$

Dividing the equation by $V_{cd} V_{cb}^*$ results in a new scaled triangle shown in Fig. 2.3 with the apex $\overline{\rho} + \mathrm{i}\overline{\eta} = -\frac{V_{ud} V_{ub}^*}{V_{cd} V_{cb}^*}$. The coloured bands show the experimental constraints on the triangle's parameters.

The triangle's angles are

$$\alpha = \arg\left(-\frac{V_{td} V_{tb}^*}{V_{ud} V_{ub}^*}\right) \, , \, \beta = \arg\left(-\frac{V_{cd} V_{cb}^*}{V_{td} V_{tb}^*}\right) \, , \, \gamma = \arg\left(-\frac{V_{ud} V_{ub}^*}{V_{cd} V_{cb}^*}\right) \, . \tag{2.11}$$

The unitarity of the CKM matrix has to be tested experimentally, hence is has to be verified that the CKM triangles close. Deviations from the previous studies could hint at effects of physics beyond the Standard Model. Decays with the quark level transition $b \to c\overline{c}s$ allow for clean measurements of the angle β due to the negligible higher-order contributions [19, 20, 21]. The $B^0 \to c\overline{c}K_{\text{S}}^0$ decay was recently studied by the LHCb

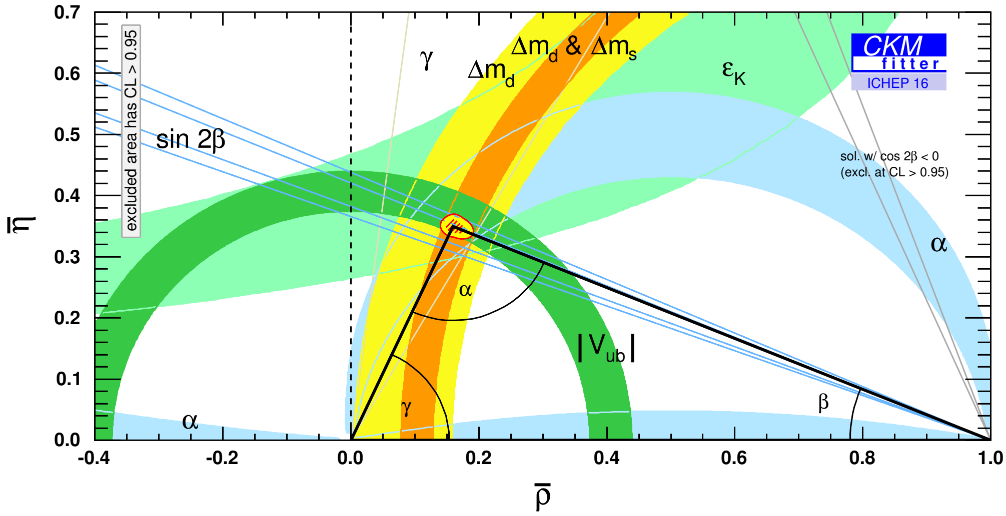

Figure 2.3: CKM triangle in the complex $(\overline{\rho}, \overline{\eta})$-plane. Corresponding to the unitary condition of the CKM matrix $V_{ud}V^*_{ub} + V_{cd}V^*_{cb} + V_{td}V^*_{tb} = 0$ divided by $V_{cd}V^*_{cb}$. The coloured bands show the experimental constraints on the triangle's parameters from different measurements [18].

experiment [1] with charmonium resonances such as the J/ψ reconstructed from two electrons and the K^0_S reconstructed from two charged pions in the final state. Because the B^0 and $\overline{B}^0$ mesons decay into the same final state, *CP* violation in the interference of direct decay and decay after mixing is possible. The decay width difference $\Delta\Gamma$ with $|\frac{\Delta\Gamma}{\Gamma}| = (0.1 \pm 1.0) \times 10^{-2}$ and also *CP* violation in mixing can be considered to be neglibible [22]. It follows for the normalization constants $|\frac{q}{p}| = 1$. The time-dependent *CP* asymmetry in the interference of direct decay and mixing in this decay is

$$\begin{aligned}\mathcal{A}_{c\bar{c}K^0_\mathrm{S}}(t) &\equiv \frac{\Gamma(\overline{B}^0(t)\to c\bar{c}K^0_\mathrm{S}) - \Gamma(B^0(t)\to c\bar{c}K^0_\mathrm{S})}{\Gamma(\overline{B}^0(t)\to c\bar{c}K^0_\mathrm{S}) + \Gamma(B^0(t)\to c\bar{c}K^0_\mathrm{S})} \\ &= \frac{S\sin(\Delta m\, t) - C\cos(\Delta m\, t)}{\cosh(\Delta\Gamma t/2) + A_{\Delta\Gamma}\sinh(\Delta\Gamma t/2)} \\ &\approx S\sin(\Delta m\, t) - C\cos(\Delta m\, t)\,,\end{aligned} \tag{2.12}$$

with B^0 as a B^0 meson produced at time $t = 0$ [1]. The factor C represents direct *CP* violation and is compatible with zero due to the supression of higher-order contributions and current experimental results [22]. Thus, the decay rate asymmetry in the $B^0 \to J/\psi K^0_\mathrm{S}$ decay gives access to the CKM angle β to a very high precision. In this approximation and with $S \approx \sin(2\beta)$, the asymmetry can be written as

$$\mathcal{A}_{c\bar{c}K^0_\mathrm{S}}(t) = \sin(2\beta)\sin(\Delta m t)\,. \tag{2.13}$$

As a result of previous measurements of *CP* violation in interference by the BaBar [23] and Belle [24] collaboration in the $B^0 \to J/\psi K^0_S$ decay, the world average [22] of $\sin(2\beta)$ is $\sin 2\beta = 0.679 \pm 0.020$.

A measurement by the LHCb experiment with reconstructed $B^0 \to J/\psi\ (\to\mu^+\mu^-)K^0_S\ (\to\pi^+\pi^-)$ decays [25] measured

$$\begin{aligned} S^{\mathrm{LHCb}}_{B^0\to J/\psi(\mu^+\mu^-)K^0_S(\pi^+\pi^-)} &= 0.731 \pm 0.035\,(\mathrm{stat.}) \pm 0.020\,(\mathrm{syst.})\ , \\ C^{\mathrm{LHCb}}_{B^0\to J/\psi(\mu^+\mu^-)K^0_S(\pi^+\pi^-)} &= -0.038 \pm 0.032\,(\mathrm{stat.}) \pm 0.005\,(\mathrm{syst.})\ , \end{aligned}$$

where the results are compatible with those of the B factories. The current world averages [22] of S and C measured from decays with the $b \to c\bar{c}s$ transition are

$$S^{\mathrm{HFLAV}}_{b\to c\bar{c}s} = 0.691 \pm 0.017, \quad C^{\mathrm{HFLAV}}_{b\to c\bar{c}s} = -0.004 \pm 0.015.$$

2.2 Lepton flavour universality violation

The dataset recorded by the LHCb experiment has the world's largest number of $b\bar{b}$-pairs. Thus it allows for high precision measurements of *CP* violation and flavour violation with rare leptonic and semi-leptonic b-hadron decays. Flavour-changing neutral currents (FCNCs) are processes where the flavour of a fermion current is changed without altering its electric charge. Although these processes are forbidden at tree level in the SM, they can occur at loop level under the exchange of a W boson. FCNC decays at loop level are suppressed by the GIM mechanism [26] and thus provide a sensitive environment for SM tests, for example quantum corrections with heavy particles above the electroweak scale [2]. One extensively tested FCNC decay is the transition $b \to s\ell^+\ell^-$ with muons or electrons in the final state, as they are practically free of hadronic uncertainties [27]. Here, a b-quark transitions to an s-quark under emission of two charged leptons. Observables that are studied in $b \to s\ell^+\ell^-$ decays are for example branching ratios, angular distributions, and lepton flavour universality (LFU) ratios. Such a ratio was proposed [28] with

$$R_H = \frac{\int_{q^2_{\min}}^{q^2_{\max}} \frac{d\mathcal{B}(B^0\to H\mu^+\mu^-)}{dq^2} dq^2}{\int_{q^2_{\min}}^{q^2_{\max}} \frac{d\mathcal{B}(B^0\to He^+e^-)}{dq^2} dq^2}\ . \tag{2.14}$$

Here, H represents a hadron containing an s-quark, like a K^+ or a K^* meson. The decay width is integrated over the squared invariant mass, q^2, of the two leptons. Using the ratios allows for a cancellation of the hadronic uncertainties and thereby reduces systematic uncertainties. The only sources of lepton flavour violation in the SM are neutrino masses, which are negligible, and the masses and Higgs interactions of the charged leptons. No observable effects follow from the Higgs interactions in the sector of rare b decays [27]. The effect of the mass difference between the muon and electron is only relevant for a kinematic limit of $q^2 \approx 4m^2_\ell$. So for a broad range of q^2 the SM predictions are $R_K = R_{K^*} = 1$

with an uncertainty of $\mathcal{O}(1\,\%)$ [27, 29]. From several physics beyond the Standard Model models deviations from the SM can be expected, for example models with a new gauge boson Z' [30] or leptoquarks [31]. Feynman diagrams of the $B^0 \to K^{*0}\ell^+\ell^-$ decay are shown in Fig. 2.4. Presented are the electroweak SM penguin and box diagram and physics beyond the Standard Model decays with a new gauge boson Z', and a leptoquark, which couples to quarks and leptons.

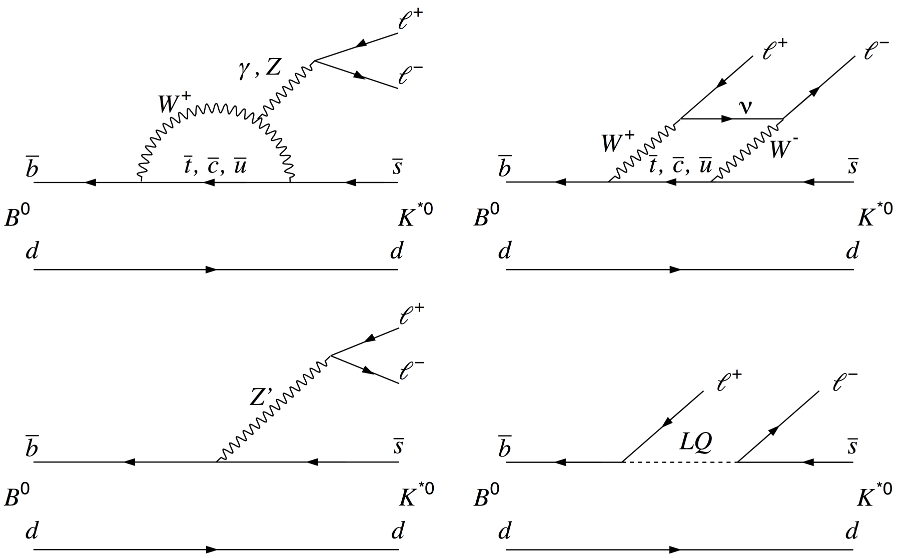

Figure 2.4: Feynman diagrams of the $B^0 \to K^{*0}\ell^+\ell^-$decay with the (top left) electroweak penguin and the (top right) box diagram. Possible physics beyond the Standard Model decays that violate lepton universality are shown below with (bottom left) a new gauge boson (Z') and (bottom right) a leptoquark (LQ). [2]

Measurements by the LHCb collaboration show hints of deviations from the SM of R_K and R_{K^*}. The measurement of the R_K ratio [3] shows a 2.6σ deviation from the SM prediction in the invariant dilepton mass region of $1\,\mathrm{GeV}^2 < q^2 < 6\,\mathrm{GeV}^2$ with a value of

$$R_K^{[1,6]} = 0.745^{+0.090}_{-0.074}\,(\mathrm{stat}) \pm 0.036\,(\mathrm{syst})\ . \tag{2.15}$$

A recently published measurement of the R_{K^*} ratio [2] shows a tension of 2.4σ with the SM in the dilepton-mass region of $0.045\,\mathrm{GeV}^2 < q^2 < 1.1\,\mathrm{GeV}^2$ and 2.5σ in the region of $1.1\,\mathrm{GeV}^2 < q^2 < 6\,\mathrm{GeV}^2$. Here, σ is defined as the standard deviation. The ratios are

$$\begin{aligned} R_{K^*}^{[0.045,1.1]} &= 0.66^{+0.11}_{-0.07}\,(\mathrm{stat}) \pm 0.03\,(\mathrm{syst}) \\ R_{K^*}^{[1.1,6]} &= 0.69^{+0.11}_{-0.07}\,(\mathrm{stat}) \pm 0.05\,(\mathrm{syst})\ . \end{aligned} \tag{2.16}$$

A comparison of the results with SM predictions from BIP [29], CDHMV [32, 33, 34], `EOS` [35, 36], `flav.io` [37, 38, 39], and JC [40] and previous experimental results from the B factories BaBar and Belle is shown in Fig. 2.5.

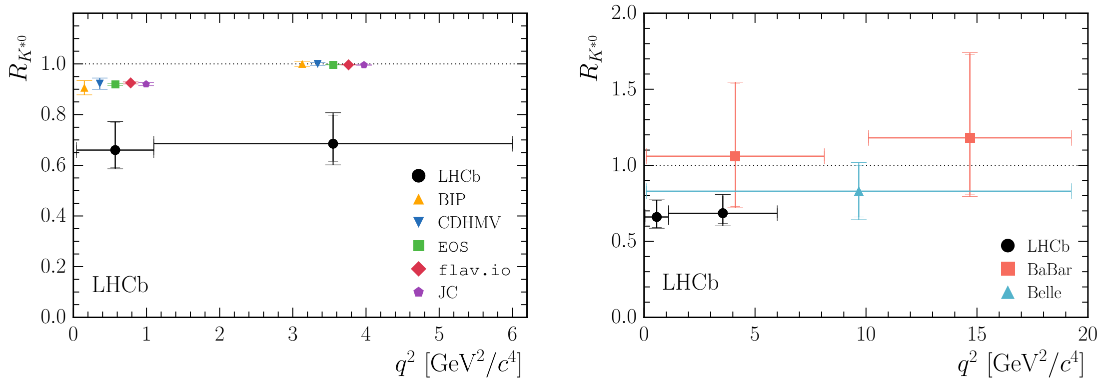

Figure 2.5: Comparison of the LHCb R_{K^*} measurements with (left) SM predictions by BIP [29], CDHMV [32, 33, 34], `EOS` [35, 36], `flav.io` [37, 38, 39], and JC [40] and (right) previous experimental results from the B factories BaBar and Belle. [2]

A series of other measurements with $b \to s\ell^+\ell^-$ decays hints at deviations from the SM, which are compatible with the deviations of R_K and R_{K^*} [27]. This calls for further studies in the field of lepton flavour universality violation.

3 The LHCb experiment

The Large Hadron Collider beauty experiment (LHCb) is one of the four large experiments at the Large Hadron Collider (LHC) at the European Organization of Nuclear Research (CERN) near Geneva. The experiment is designed for high precision searches for physics beyond the Standard Model in the sector of flavour physics, mainly with hadrons containing b- and c-quarks. Two of the main fields of the experiment's searches are studies of CP violating decays, which may hint at experimental deviations from the SM predictions, and the studies of rare decays, where small contributions of physics beyond the Standard Model effects could lead to significant deviations from the SM. In the following the LHC, the LHCb detector, and the LHCb software framework is described. The description of the LHCb detector mainly follows the Refs. [41, 42], unless otherwise stated.

3.1 The Large Hadron Collider

The LHC [43] is a circular particle accelerator and collider at CERN. It is the world's largest particle accelerator providing the world's highest collision energies. The LHC is located in a 26.7 km long tunnel below the surface and collides protons with a maximum centre-of-mass energy of up to $\sqrt{s} = 13\,\text{TeV}$ [44]. Two oppositely accelerated proton beams are brought to collision at four collision points in the accelerator tunnel where the LHCb, CMS, ATLAS, and ALICE detectors are located. The proton bunches have a spacing of 50 ns instead of the previously targeted 25 ns to improve the beam stability [45]. In 2015 it was again decreased to 25 ns. In 2011 and 2012, the single beams consisted of up to 2808 proton bunches with approximately 1.15×10^{11} protons contained in each bunch. Prior to the acceleration within the LHC, the protons are passing a pre-acceleration chain of different linear and circular particle accelerators as shown in Fig. 3.1. After being accelerated in the Linear Accelerator 2 (LINAC2) the protons pass the Proton Synchrotron Booster (PSB), the Proton Synchrotron (PS), and the Super Proton Synchrotron (SPS) to reach an energy of 450 GeV. Finally, the protons are accelerated with the LHC from a centre-of-mass energy of 450 GeV up to a centre-of-mass energy of 7 TeV in 2011. The centre-of-mass energy was raised to 8 TeV in 2012 and 13 TeV in 2015. The proton beams are aligned and accelerated by 1232 superconducting dipole magnets cooled with suprafluid helium and a field strength of up to 8.3 T. The ATLAS and CMS detectors are multi-purpose detectors constructed to cover the entire solid-angle and work with a maximum luminosity. Through their construction as ”discovery experiments” they were able to observe the Higgs boson in 2012 [46, 47]. The ALICE experiment primarily analyses quark-gluon plasmas. The LHCb experiment is designed for high-precision experiments with b- and c-hadrons in the field of flavour physics.

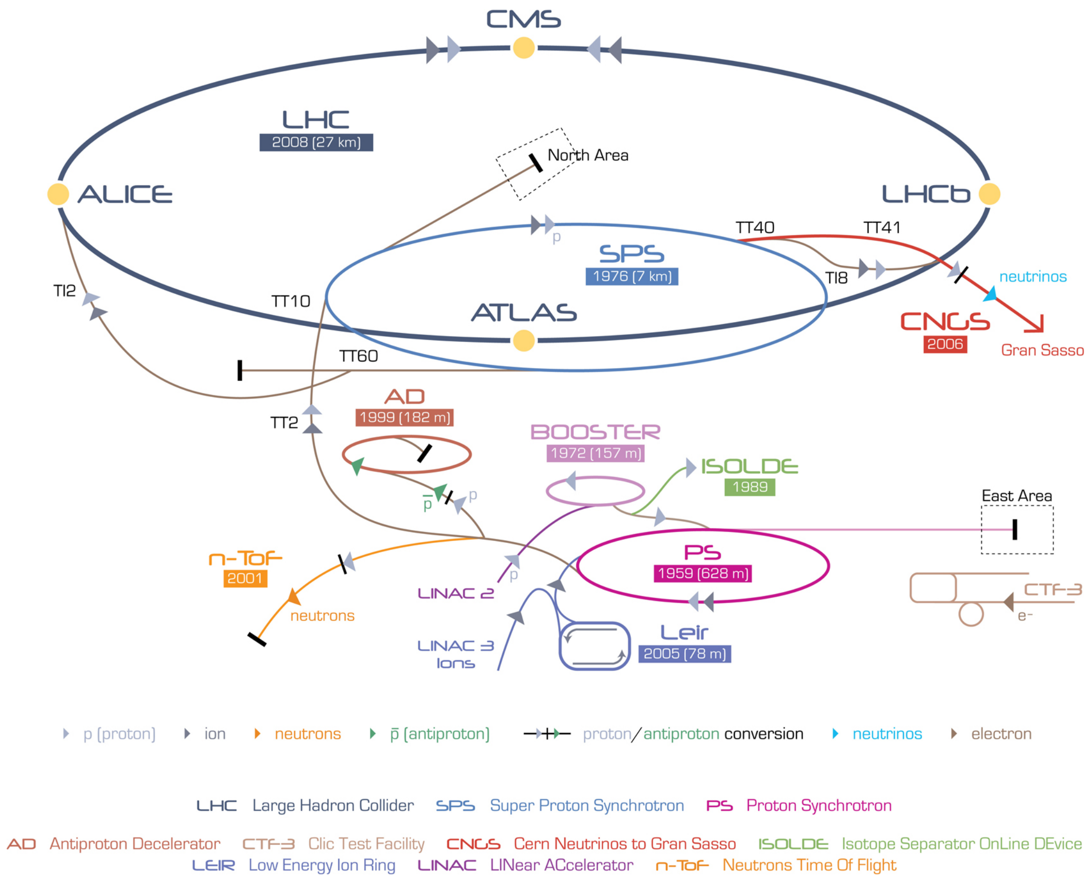

Figure 3.1: Schematic illustration of the CERN accelerator complex. Protons that are accelerated in the LHC pass a pre-acceleration chain consisting of the LINAC2, the PSB, the PS, and the SPS [48].

3.2 The LHCb detector

The LHCb detector is a single-arm forward spectrometer with an angular acceptance of 10 mrad to 300 mrad in the horizontal plane and 10 mrad to 250 mrad in the vertical plane. A schematic view of the detector can be found in Fig. 3.3.Hereby a pseudorapidity of $2 < \eta < 5$ is covered. Besides multiple different contributions the production of b-quarks at the LHC is dominated by gluon-gluon fusion, where two gluons create a $b\bar{b}$-pair. Due to the nature of pp collisions at the energies of the LHC, the two gluons have a high probability to have a high momentum difference. Thus, the produced $b\bar{b}$-pair is likely to be heavily boosted along the beam axis, as can be seen in Fig. 3.2. To allow for high-precision measurements the LHCb experiment uses only a fraction of about $4 \times 10^{32}\,\mathrm{cm^{-2}s^{-1}}$ [42] of constant luminosity of proton-proton collisions of the LHC.

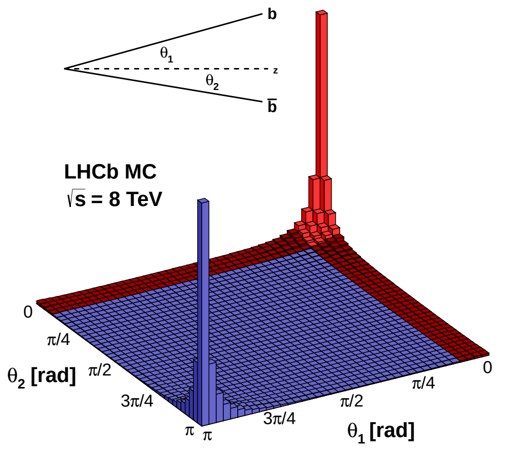

Figure 3.2: Angular distribution of the $b\bar{b}$-pair production probability in proton-proton collisions at the LHC with a centre-of-mass energy of $\sqrt{s} = 8\,\text{TeV}$. The red area represents the geometric acceptance of the LHCb experiment [49].

3.2.1 Tracking system

To fulfil the experimental requirements to achieve high-precision measurements in the hadron sector with a high track multiplicity, the LHCb experiment provides an excellent vertex reconstruction, tracking, and momentum measurement. The Vertex Locator (VELO) is a silicon-strip detector surrounding the proton-proton interaction point and allows for a high spatial resolution. The Tracker Turicensis (TT) is a large-area silicon-strip detector followed by the detector's dipole magnet with an magnetic field of 4 T m and the three tracking stations (T1,T2,T3) with an inner silicon-strip Tracker (IT) and an Outer Tracker (OT) consisting of straw tubes. Tracks are reconstructed for charged particles passing the detector. The momentum resolution $\frac{\Delta p}{p}$ of the LHCb tracking system is in the range of 0.4 % to 0.6 % depending on the track energy.

The VELO is surrounding the interaction point as the first part of the tracking system. It is designed to reconstruct the production and decay vertices of the b-hadrons. The b-hadrons have a typical flight distance of several millimeters before they decay. A precise measurement of these vertices allows for an excellent resolution of the decay time. To cover the entire detector accpetance the VELO has a cylindrical construction. It is build of 21 semi-circular silicon disc stations. The discs have a radius of 42 mm and can be moved in the direction of the beam axis up to a distance of 8 mm close to the beam.

The TT and the three tracking stations T1,T2, and T3 are part of the LHCb tracking system. The TT is positioned behind the first ring-imaging Cherenkov detector (RICH1). The stations are divided into the Inner Tracker (IT), which is located in the proximinity of the beam axis and the Outer Tracker (OT) around. Both the IT and the TT are silicon detectors each consisting of four rotated layers of silicon strips. A magnet with a

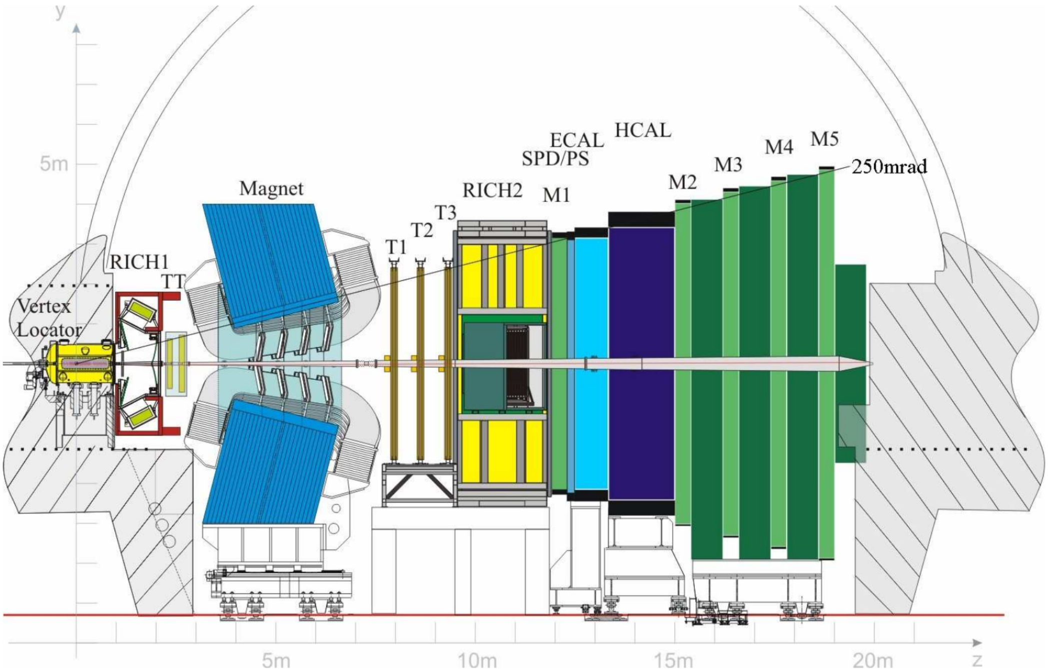

Figure 3.3: Schematic view of the LHCb detector. The following detector components can be seen from left to right: the Vertex Locator, which encloses the proton-proton interaction point, the two Cherenkov detectors, the tracking system with magnet, the calorimeters, and the muon chambers. [41]

magnetic field of 4 T m bends the tracks of charged particles. For the studies of detection asymmetries the polarity of the dipole magnet is reversed during the data taking (*MagDown* and *MagUp*). The OT is a drift detector consisting of straw tubes that are filled with a gas mixture of 70 % Argon, 28.5 % CO_2, and 1.5 % O_2.

3.2.2 Particle identification system

To allow for a precise distinction of different final states of the decays of b-hadrons, the LHCb experiment is instrumented with a multi-stage particle identification (PID) system. It consists of two ring-imaging Cherenkov detectors to especially distinguish between kaons, pions, and protons and a system of calorimeters to detect photons, electrons, and hadrons. Muons are identified by hits in the muon system.

The two Cherenkov detectors cover the full detector acceptance allowing for a broad range of particle momenta. They exploit the Cherenkov effect, where a charged particle emits electromagnetic radiation passing through material with the refractive index, n, at a speed of v. The speed, v, has to be higher than the speed of light, $c' = \frac{c}{n}$, in the medium, with c as the speed of light in vacuum. The radiation is emitted in a cone with an angle θ

depending on the particle's speed with

$$\cos\theta = \frac{1}{n\beta} \text{ with } \beta = \frac{v}{c}. \tag{3.1}$$

In combination with the particle's momentum this allows for a precise distinction between different particles. The RICH1 is located between the VELO and the TT. It employs a combination of aerogel with a refractive index of $n = 1.03$ allowing for kaon identification and π-K-separation for low momenta and a C_4F_{10} radiator to separate particles with higher momenta. The aerogel was removed from the detector in 2013-2014 to improve its particle identification abilities. The RICH2 is installed between the T3 and the first muon chamber M1 behind the magnet. Using a CF_4 radiator it allows for a separation between pions and kaons in a high momentum range. Inside the RICH detectors, the Cherenkov light is mirrored with spherical mirrors resulting in rings of light. Additional mirrors reflect the Cherenkov light out of the detector acceptance where it is measured with hybrid silicon photon detectors.

The calorimeter system of the LHCb experiment is designed to perform particle identification of electrons, photons, hadrons, and partly muons. Additionally, it provides information about particle energies and track positions as an input to the trigger system. The calorimeter system is located between the two muon stations M1 and M2 and consists of the scintillating pad detector (SPD), the preshower (PS), an electromagnetic calorimeter (ECAL), and a hadronic calorimeter (HCAL). The ECAL resembles a sampling calorimeter with segments of alternating material. Scintillating tiles alternate with absorbing lead segments. Thus photons deposit their entire energy in the ECAL. The HCAL is a sampling calorimeter with layers of scintillating material and iron to measure the energy of hadrons.The wavelength of the emitted radiation is shifted via wavelength-shifting fibres. The calorimeters are segmented in the xy-plane, where the segment size increases in the proximity of the beam axis, considering a higher hit multiplicity in this region. The SPD consists of scintillating segments and allows for a distinction of photons, neutral pions, and electrons and positrons. The PS also consists of scintillating tiles and is separated from the SPD by a layer of lead where electrons are likely to shower. Thus the PS allows for a distinction between electrons and charged hadrons and supression of background consisting of charged pions.

Muon detection is a fundamental part of the LHCb experiment as many b-hadron decays include final states with muons. The LHCb detector is instrumented with the five muon stations M1-M5. The station M1 is located upstream of the calorimeter system, whereas M2-M5 are positioned downstream of the calorimeter system. As the stations are separated by 80 cm thick iron absorbers only muons with a momentum higher than 5 GeV/c are able to pass the whole muon system. The muon chamber M1 consists of gas-electron multipliers and the stations M2-M5 are equipped with 1380 multi-wire proportional chambers (MWPCs).

3.2.3 Trigger system

To be able to efficiently store the data from the LHCb detector a data rate reduction is performed through a two level trigger system. The Level 0 trigger (L0) is a hardware trigger that identifies the maximum transerval energy, E_{T}, of hadrons, electrons, and photons and the maximum transverse momentum, p_{T}, of muons and dimuons. Thus it uses information from the calorimeters and the muon detection system to filter relevant events. The second trigger stage is the High Level Trigger (HLT), which performs a first selection of relevant decays with a supression of backgrounds. The HLT is a software trigger with two levels, where the HLT1 reconstructs particle candidates with information from the L0 trigger, the VELO, and the tracking system and HLT2 performs an offline reconstruction and a second filtering with events triggered by HLT1.

3.2.4 LHCb software

The LHCb software is based on the software framework Gaudi [50]. The HLT is implemented with the software package Moore [51]. The reconstruction of the raw data is performed by the software package Brunel [52]. The resulting Data Summary Tape files (DST) are further processed with the software package DaVinci [53] where a first analysis-dependent offline selection (stripping) is performed. The LHCb flavour-tagging software is part of the software package DaVinci and determines the inital flavour of the B mesons at production time. In further studies, common software packages are the Root [54] and RooFit [55] software package. The software package Gauss [56] is employed for event simulation. It makes use of the software packages EvtGen [57], Pythia [58], and Geant4 [59], which simulate the proton-proton collision, the hadronization process and the detector interaction. The digitization of the data is performed by the software package Boole [60], that makes the simulation samples appear as raw data from the detector. Then the simulated samples are processed like data as described before.

4 Flavour tagging at the LHCb experiment

In decay-time-dependent measurements of *CP* violation it is essential to know the inital flavour of the decaying B meson candidate. Thus the goal of the flavour tagging at LHCb is to distinguish for example between B^0 and $\overline{B}^0$ or B_s^0 and $\overline{B}_s^0$ particles. The initial flavour of the signal B meson depends on the hadronization b-quark. Different flavour-tagging algorithms, called *taggers* classify the inital flavour of the meson. The taggers can be categorized into same-side taggers (SS taggers) and opposite-side taggers (OS taggers) [61, 62, 63]. The SS taggers use information coming from the decay of the signal B meson and the OS taggers from the decay of the fragmentation hadron, h_b, which consists of the second b-quark as can be seen in Fig. 4.1. The tagging algorithms compute a decision for the production flavour and a probability of a wrong decision.

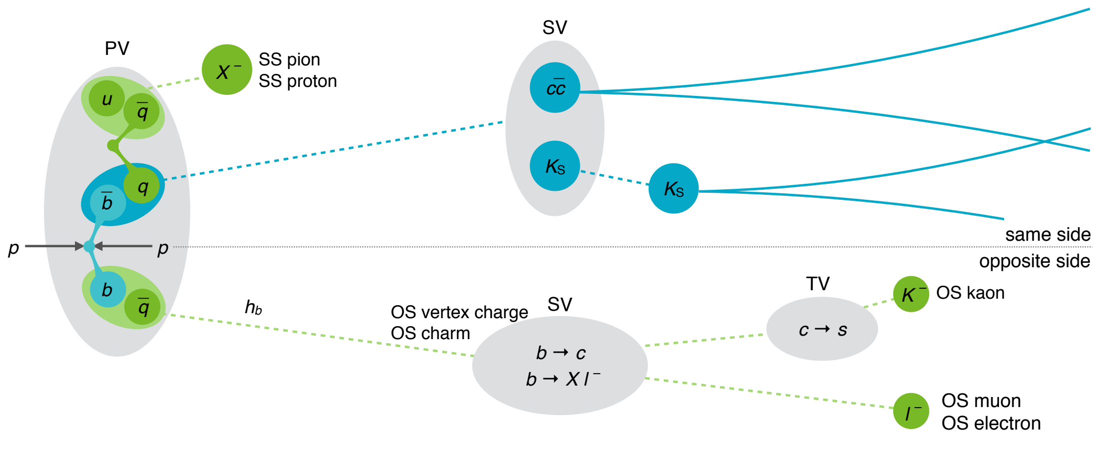

Figure 4.1: Schematic overview of the flavour tagging algorithms used in this analysis [64].

4.1 Flavour-tagging variables

Each flavour-tagging algorithm, i, provides a per-event decision, d_{i}, about the inital flavour of the reconstructed candidate and a mistag probability estimate, η_i, which is the predicted probability of mis-classification. The tagging decision, d_{i}, (tag) can take the values $-1, 1$, and 0, which stand for a b, a $\overline{b}$-quark, or no decision. Events with no assigned tag are called *untagged*. Thus, for $d_{\text{i}} = -1$ the B meson is tagged as a B^0 meson ($\overline{b}d$) an for $d_{\text{i}} = 1$ as a $\overline{B}^0$ meson ($b\overline{d}$). The corresponding predicted mistag probabilty η_i takes a continuous value between 0 and 0.5 and is calculated with a multivariate classifier, which is trained with simulated samples or flavour-specific decays taking in account transversal momenta, number of combined vertices, tracks and futher kinematic and topological observables. The false classification is mainly due to mixing or oscillation of the fragmentation hadron, wrong lepton tags, or the use of misidentified particles or particles from the background. For untagged events, the predicted mistag probability is set to 0.5. As this probabilty is only a prediction, the true mistag probabilty or raw mistag ω is calculated as

$$\omega = \frac{N_{\text{incorrect}}}{N_{\text{tagged}}} = \frac{N_{\text{incorrect}}}{N_{\text{correct}} + N_{\text{incorrect}}}. \tag{4.1}$$

where N_{correct} is number of correctly tagged candidates in a sample and $N_{\text{incorrect}}$ the number of incorrectly tagged events. The true mistag probabilty ω can be calculated with truth information on simulated samples. The calibrated mistag probability is a direct input to the measured *CP* asymmetry of the B mesons with

$$\mathcal{A}_{\text{measurement}} = (1 - 2\omega)\mathcal{A}(t)_{\text{theory}} = D\mathcal{A}(t)_{\text{theory}}\,. \tag{4.2}$$

Here, the dilution

$$D = 1 - 2\omega\,, \tag{4.3}$$

resembles the effective statistical power of the sample. The flavour-tagging efficiency differs between the flavour-tagging algorithms and is defined as

$$\varepsilon_{\text{tag}} = \frac{N_{\text{tagged}}}{N_{\text{tagged}} + N_{\text{untagged}}}, \tag{4.4}$$

where N_{tagged} is the fraction of incorrectly and correctly tagged events, and N_{untagged} is the fraction of candidates without a tag.

The effective tagging efficiency or tagging power gives the effective statistical reduction of the sample size and is the combination of the tagging efficiency and the dilution with

$$\varepsilon_{\text{eff}} = \varepsilon_{\text{tag}} D^2 = \varepsilon\,(1 - 2\omega)^2\ . \tag{4.5}$$

The product of the number of candidates and the effective tagging efficiency gives the number of candidates with the correct tag, which is needed to yield the same statistical significance as the original sample. The flavour-tagging efficiency also allows a comparison of the performances of the different flavour-tagging algorithms.

The true mistag probability can depend on the flavour of the B mesons with a tagging asymmetry $\Delta\omega = \omega_{\overline{b}} - \omega_b$, where $\omega_{\overline{b}}$ is the mistag probability for $\overline{B}^0$ mesons and ω_b for $\overline{B}^0$ mesons.

4.2 Flavour-tagging algorithms

The flavour-tagging algorithms can be divided into single-particle and multiple-particle taggers as described below. The predictions of the different taggers can be joined in combination taggers, where the combined probability of the signal B meson to contain a b-quark is

$$P(b) = \frac{p(b)}{p(b) + p(\bar{b})}\,, \tag{4.6}$$

and

$$P(\bar{b}) = 1 - P(b)\,, \tag{4.7}$$

with the probabilities $p(b)$ and $p(\bar{b})$ defined as

$$p(b) = \prod_i \left(\frac{1 + d_\mathrm{i}}{2} - d_\mathrm{i}(1 - \eta_\mathrm{i}) \right)\,, \tag{4.8}$$

and

$$p(\bar{b}) = \prod_i \left(\frac{1 - d_\mathrm{i}}{2} - d_\mathrm{i}(1 - \eta_\mathrm{i}) \right)\,. \tag{4.9}$$

Here, d_i are the tagging decisions and η_i the predicted mistag probabilities of the single taggers. The combined tagging decision d and η depend on $P(b)$ and $P(\bar{b})$ as follows

$$d = -1, \quad \eta = 1 - P(b) \qquad \text{for} \qquad P(b) > P(\bar{b})\,, \tag{4.10}$$

$$d = 1, \quad \eta = P(b) \qquad \text{for} \qquad P(b) < P(\bar{b})\,. \tag{4.11}$$

4.2.1 Opposite-side tagging

The OS taggers can be divided into single-particle taggers and multiple-particle taggers. The single-particle taggers exploit the charge of a single reconstructed particle to determine the B meson's inital flavour. The OS single-particle taggers used in this analysis are the OS muon, OS electron, OS kaon, and OS charm tagger. As a multiple-particle tagger, the OS vertex charge tagger is employed, which comprises charges of particles tracks coming from a common secondary vertex not associated with the signal B meson. [63]

The OS muon tagger uses a muon from the semileptonic $b \to Xl$ decay, where muons from the background are reduced through momentum cuts. In the case of multiple muon candidates, the one with the highest transversal momentum, p_T, is chosen.

The OS electron tagger exploits the charge of an electron also from a semileptonic decay of the b-quark. The electron selection is performed through momentum cuts, further information from the particle identification system, for example the ratio of measured energy from the electromagnetic calorimeter, and the momentum of the electron candidate. In case of multiple electron candidates, analogously to the OS muon tagger the one with the highest p_{T} is chosen.

The OS kaon tagger uses kaons hadronized through the decay chain $b \to c \to s$ and also performs a cut based selection and choses the kaon candidate with the highest p_{T}.

The OS charm tagger [61] determines the inital flavour of the signal meson from reconstructed D meson candidates coming from the $b \to c$ decay. In the presence of charged D meson candidates the decision is made directly and in case of an neutral D meson from the kaon to which the D meson decays. The D meson candidates are selected with a Boosted Decision Tree (BDT) [65].

As a multiple-particle tagger, the OS vertex charge tagger performs an inclusive reconstruction of secondary vertices of decay products. The iterative combination of tracks after a cut-based preselection results in a weighted charge, Q_{Vertex}, of the reconstructed vertex with

$$Q_{\mathrm{Vertex}} = \frac{\sum_i {p_{\mathrm{T}}}^{\mathrm{k}}(i) Q_{\mathrm{i}}}{\sum_i {p_{\mathrm{T}}}^{\mathrm{k}}(i)}\,, \tag{4.12}$$

where k is a parameter that optimizes the effective tagging efficiency, $p_{\mathrm{T}}(i)$ as the transverse momentum of the reconstructed track i, and the track charge Q_{i}. The flavour-tagging decision is consequently based on the weighted charge Q_{Vertex}.

The standard combination of the OS taggers, which is implemented in the flavour-tagging software framework, takes the results of the OS electron, the OS muon, the OS kaon, OS charm, and the OS vertex charge tagger into account.

4.2.2 Same-side tagging

The SS tagging determines a decision about the inital flavour of the signal B meson with particles corresponding to its hadronization. Through the production of a B^0 meson ($\bar{b}d$) an additional $\overline{d}$ is created, which can further hadronize into a pion or proton. The hadronization of a B_s^0 meson produces a $\overline{s}$-quark, which can form a kaon. The SS pion, the SS proton, and the SS kaon taggers exploit the formation of these particles.

The SS pion tagger uses the charge of a pion coming from the hadronization process of the B meson. The pion candidates are selected with a BDT classifier.

The SS proton tagger operates similar to the SS pion tagger and also uses a BDT to select proton candidates in contrast to the SS kaon tagger, which employs a cut based selection.

The SS standard combination makes use of the results of the SS pion and the SS proton tagger.

4.3 Flavour-tagging calibration

The predicted mistag probability, η, can be incorrect. Thus, it has to be calibrated, resulting in a true calibtrated mistag probability, $\omega(\eta)$. In this analysis a linear relation between η and $\omega(\eta)$ is assumed with

$$\omega(\eta) = p_0 + p_1(\eta - \langle\eta\rangle)\,, \tag{4.13}$$

where p_0 and p_1 are the fit parameters and $\langle\eta\rangle$ is the average predicted mistag probability. The use of the average predicted mistag probability $\langle\eta\rangle$ aims for a decorrelation of the paramters p_0 and p_1. After the calculation of the calibration parameters the calibrated mistag probability $\omega(\eta)$ is determined for each event and can be used directly as an input in the measurement of *CP* violation as shown in Eq. (4.2).

For a perfectly calibrated flavour-tagging algorithm, the calibration parameters are $p_0 = \langle\eta\rangle, p_1 = 1$.

Asymmetries in the tagging efficiencies and mistag probabilities between initial B^0 and $\overline{B}^0$ mesons, are considered with two independent calibration functions

$$\omega^{B^0}(\eta) = p_0^{B^0} + p_1^{B^0}(\eta - \langle\eta\rangle)\,, \tag{4.14}$$
$$\omega^{\overline{B}^0}(\eta) = p_0^{\overline{B}^0} + p_1^{\overline{B}^0}(\eta - \langle\eta\rangle). \tag{4.15}$$

The calibration parameters p_i (with $i = 0, 1$) can be parametrized as

$$p_\mathrm{i}^{B^0} = p_\mathrm{i} + \frac{\Delta p_\mathrm{i}}{2}, \quad p_\mathrm{i}^{\overline{B}^0} = p_\mathrm{i} - \frac{\Delta p_\mathrm{i}}{2}\,, \tag{4.16}$$

to take account for the asymmetries with the asymmetry parameters Δp_i. Thus the resulting parametrization of the mistag asymmetries becomes

$$\begin{aligned}\Delta\omega(\eta) &= \omega^{B^0}(\eta) - \omega^{\overline{B}^0}(\eta)\\ &= \Delta p_0 + \Delta p_1(\eta - \langle\eta\rangle).\end{aligned} \tag{4.17}$$

The flavour-tagging calibration is only possible with flavour-specific decay channles, where the inital flavour at production time can be reconstructed from decay products. This is the case for decays like $B^0 \to D^{*-}\mu^-\nu_\mu$, $B^0 \to J/\psi K^*$, $B^+ \to \overline{D}^0\pi^+$, or $B^+ \to J/\psi K^+$. The last two decays are called self-tagging, because the inital flavour can directly be reconstructed from the charges of the decay products, as no oscillations can occur. But for neutral B mesons, which can oscillate, a fit to the decay time is performed to reconstruct the production flavour. The calibrations of this analysis are performed with the LHCb flavour-tagging tool EspressoPerformanceMonitor [66], which uses binomial regression for the fits. For neutral decay channels, where time-dependent *CP* violation is studied, it is not possible to reconstruct the inital flavour of the signal B meson. Thus the flavour-tagging calibration parameters from similar flavour-specific decays are employed to correct the *CP* violation measurement in these decays.

5 Flavour-tagging calibration

In the following, the flavour-tagging calibration of the time-dependent *CP*-violation analysis with $B^0 \to J/\psi K^0_S$ decays [1] is performed. The overall study is a combination with a similar analysis of the $B^0 \to \psi(2S)K^0_S$ decay to determine the *CP* observables C and S. The measurement of *CP* violation in the interference of decay and mixing with the $B^0 \to J/\psi K^0_S$ decay is the first *CP* analysis of this decay with electrons in the final state. A sample of pp collision data recorded by the LHCb experiment with a centre-of-mass energy of $\sqrt{s} = 7\,\text{TeV}$ in 2011 and $\sqrt{s} = 8\,\text{TeV}$ in 2012 is used. This corresponds to an integrated luminositiy of $1\,\text{fb}^{-1}$ and $2\,\text{fb}^{-1}$, respectively. The flavour tagging plays a crucial role in the determination of asymmetries between B^0 and $\overline{B}^0$ mesons as described in Sec. 2.1. Here, the asymmetry between the decay of the B^0 and $\overline{B}^0$ mesons is described in Eq. (2.12). The decay rate, $\Gamma(t, d)$, for the B^0 mesons is decay-time and production-flavour dependent with

$$\Gamma(t, d) \propto \mathrm{e}^{-\frac{t}{\tau}} \left[\cosh(\tfrac{1}{2}\Delta\Gamma t) + A_{\Delta\Gamma} \sinh(\tfrac{1}{2}\Delta\Gamma t) - d \cdot S \sin(\Delta m t) + d \cdot C \cos(\Delta m t) \right], \quad (5.1)$$

with the decay time, t, the mean lifetime, τ, and the initial flavour of the B^0 meson at production time, d [1]. The decay candidates' final flavour-tagging decision d is calculated from a combination of the OS taggers and a combination of the SS taggers as described in Chapter 4. The flavour-tagging parameters of the signal channel are calibrated with kinematically similar and flavour-specific control channels. The calibration of the OS taggers is performed with the $B^+ \to J/\psi(\to e^+e^-)K^+$ decay channel and of the SS taggers with the $B^0 \to J/\psi(\to e^+e^-)K^{*0}$ decay. The lowest-order feynman diagrams of the control channel decays are shown in Fig. 5.1.

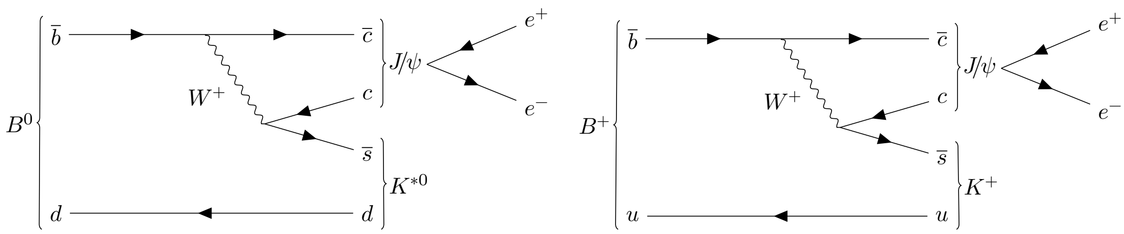

Figure 5.1: Lowest-order Feynman diagrams of the (left) $B^0 \to J/\psi(\to e^+e^-)K^{*0}$ and (right) $B^+ \to J/\psi(\to e^+e^-)K^+$ decays.

The analysis strategies for the two control channels are very similar to the analysis of the signal channel. They comprise the candidate selection, the fit to the invariant mass distribution to determine signal weights, a reweighting of the control channels to match the signal channel's kinematic distributions that are relevant for the flavour tagging and the final flavour-tagging calibration. As mentioned before, the control channels are reconstructed as $B^+ \to J/\psi(\to e^+e^-)K^+$ and $B^0 \to J/\psi(\to e^+e^-)K^{*0}$. In the following, they are abbreviated with $B^+ \to J/\psi K^+$ and $B^0 \to J/\psi K^{*0}$. The K^* candidate is reconstructed from a pion and a charged kaon. Depending on the decay channel, different trigger and stripping requirements are applied, followed by basic offline selections, including a data- and simulation-driven training and optimization of a multivariate classifier. This aims at reducing the amount of combinatorial background while retaining a high signal efficiency. Here, the final requirement on the multivariate classifiers is determined using the effective signal size as a figure of merit.

The flavour-tagging calibration on the control channels is performed as a part of this master's thesis, which provides a direct input to the determination of the *CP* observables. Besides this, the uncertainties on the *CP* observables include the systematic uncertainties of the flavour tagging determined in Sec. 5.5. The final results of the time-dependent *CP*-violation analysis are presented in Sec. 5.7.

5.1 Selection

The event selection process of the control channels $B^+ \to J/\psi K^+$ and $B^0 \to J/\psi K^{*0}$ has several stages. First, an online selection is performed with the LHCb trigger system. Then an offline selection, called stripping, is perfomed centrally. After a second preselection to further reduce the data size and suppress backgrounds, a selection using a multivariate classifier with Boosted Decision Trees [65] is applied. The cut on the BDT response is optimized using the signal efficiency as a figure of merit (FOM). In order to calculate the FOM *sWeights* [67] are calculated with a fit to the invariant mass of the B^+ and B^0 signal candidates. The *sPlot* technique allows for a discrimination of statistical contributions of different sources, like signal and background, on a data sample. Therefore an observable with a high discrimination power is needed, that is not correlated to the observable to be studied. Here, the reconstructed invariant mass of the B mesons is used. The weighted datasets are consequentially used as control channels in the flavour-tagging calibration.

The first offline selection, called stripping, is performed using the LHCb software package DaVinci [53], with stripping v21r1p1 for 2011 and v21r0p1 for 2012. The names of the the stripping lines are `Bd2JpsieeKSBu2JpsieeKFromTracksDetachedLine` and `Bd2JpsieeKSBd2JpsieeKstFromTracksDetachedLine`. In the reconstruction and processing stage of the samples a kinematic fit, called `DecayTreeFit` (DTF) [68] is employed to correctly include correlations and uncertainties of the vertex position, particle momenta, flight distances, decay times, and invariant masses. In the computation of the mass of the reconstructed B candidates the J/ψ daughter particle is constrained to its world average mass [9]. The B candidates are further constrained to originate from the primary vertex (PV). The stripping requirements on the tracks and particles are given in Table 5.1. Here, the electron candidates are required to have a high transveral momentum, p_{T}, as they originate from a J/ψ meson. The closest distance between two particle tracks (DOCA) is required to be small as the electron candidates are expected to decay from the same

J/ψ meson. Moreover, a cut on the reconstruction quality χ^2 of the track fit is required, as the fit quality is expected to be higher for electron candidates than for background. Analogously, cuts on the quality of the track fits are required for the J/ψ, K, and B candidates. A cut on the difference of the logarithmic likelihood values of the e and π hypothesis ($\mathrm{DLL}_{e\pi}$) is applied to make use of information from the particle indentification system. The J/ψ candidates are selected with an asymmetric mass window, taking the known mass of the J/ψ meson and bremsstrahlung effects into account. For B meson candidates symmetric cuts on the reconstructed invariant mass are required. Additionally, a cut on the B decay time is applied, to ensure that the candidate has a certain flight distance and is not reconstructed from arbitrary particles from the PV. Candidates in the simulation samples are further required to be correctly reconstructed as signal. No specific trigger decisions are required, because the precise knowledge of trigger efficiencies is not important in this analysis and does not need to be evaluated. Additional requirements, which are applied after the stripping, are presented in Table 5.2 and enhance the signal purity of the data. These preselection cuts are developed to match the selecton of the $B^0 \to J/\psi K^0_\mathrm{S}$ signal decay, while providing a high brackground rejection. Here, a cut on the IP χ^2 of the electrons, which is defined as the increase in χ^2 when including the track to the vertex fit, is required. A low IP χ^2 resembles incompatibility with an origin from the primary vertex, which is expected as the electrons decay from the J/ψ candidate. The same requirement is considered for the J/ψ candidate, which originates from the B candidate. Additionally, for the electrons a cut on the electron probability (ProbNNe) and on the fit qualites of the vertex fits of the B candidate is applied.

To further reduce combinatorial background a cut on the response of a multivariate classifier is applied. Here, Boosted Decision Trees (BDT) from the machine learning framework scikit-learn [69] are used. The classifiers employ the AdaBoost boosting algorithm [70] and are tuned via a hyper-parameter search. Used are 50 estimators with a learning rate of 1.0. The training is performed on a simulated signal sample and events from the data sample with a mass of the reconstructed B candidate of $m > 5600\,\mathrm{MeV}/c^2$. The classifiers are trained and tested via k-folding with six folds of the data. The BDT utilizes kinematic and topological observables and their fit qualities. Observables related to the particles identification of the detector are not employed because of the differences between simulation and data, which are not corrected in this analysis. The variables are chosen from a set of variables, which describe the decay topology and the reconstruction qualities, to optimize the feature importance of the classifiers. The feature selection is performed with a grid search optimization as a systematic test of combinations of variables. For the $B^+ \to J/\psi K^+$ decay channel the BDT input variables are the B^+ decay vertex reconstruction quality, the p_T of the B^+, electrons, and J/ψ candidates, the impact parameter (IP) of the B^+ candidate, the minimum and the maximum of the logarithm of the IP χ^2 of the electrons, the IP χ^2 of the second-best minimum IP, the IP χ^2 of the B^+ candidate, and the electrons, and the minimum IP χ^2 of the K^+ candidates. For the $B^0 \to J/\psi K^{*0}$ decay the chosen features are the minimum and the maximum of the logarithm of the IP χ^2 of the electrons, the fit quality of the B^0-decay vertex reconstruction, the transverse momentum of the B^0 candidate, the IP χ^2 of the B^0 candidates and the electrons, the minimum IP χ^2 of the pion candidates, and the minimum IP of the J/ψ candidates. The BDT input variables are listed in Table A.1.

Table 5.1: Requirements on the particle candidates as applied in the stripping for the $B^+ \to J/\psi K^+$ and $B^0 \to J/\psi K^{*0}$ decays. $\mathrm{DLL}_{e\pi}$ is the difference of logarithmic likelihood values of the e and π hypothesis. DOCA is the closest distance between two particle tracks. χ^2 is a measure of the quality of the performed fit.

	$B^+ \to J/\psi K^+$	$B^0 \to J/\psi K^{*0}$
e candidates		
p_{T}	$> 500\,\mathrm{MeV}/c$	$> 500\,\mathrm{MeV}/c$
$\mathrm{DLL}_{e\pi}$	> 0	> 0
χ^2 of the track fit	< 5	< 5
DOCA χ^2	< 30	< 30
J/ψ candidates		
$m(ee)_{\mathrm{min}}$	$2300\,\mathrm{MeV}/c^2$	$2300\,\mathrm{MeV}/c^2$
$m(ee)_{\mathrm{max}}$	$3300\,\mathrm{MeV}/c^2$	$3300\,\mathrm{MeV}/c^2$
χ^2 of the vertex fit	< 15	< 15
K candidates		
χ^2 of the vertex fit	< 20	-
p_{T}	$> 800\,\mathrm{MeV}/c$	$> 1500\,\mathrm{MeV}/c$
B candidates		
decay time t	$> 0.2\,\mathrm{ps}$	$> 0.2\,\mathrm{ps}$
$m(B^+)_{\mathrm{min}}$	$4400\,\mathrm{MeV}/c^2$	$4400\,\mathrm{MeV}/c^2$
$m(B^+)_{\mathrm{max}}$	$6000\,\mathrm{MeV}/c^2$	$6000\,\mathrm{MeV}/c^2$
χ^2 of the vertex fit	< 7	< 20
π candidates		
p_{T}	-	$> 600\,\mathrm{MeV}/c$

Table 5.2: Preselection requirements applied to reconstructed $B^+ \to J/\psi K^+$ and $B^0 \to J/\psi K^{*0}$ candidates. IP χ^2 is defined as the increase in χ^2 when including the track to the vertex fit and ProbNNe is the probability of the particle to be an electron.

	$B^+ \to J/\psi K^+$	$B^0 \to J/\psi K^{*0}$
$\max(\ln(\mathrm{IP}\ \chi^2))$ of the electrons	> 2.5	> 2.5
$\min(\ln(\mathrm{IP}\ \chi^2))$ of the electrons	> -0.5	> -0.5
ProbNNe of the electron	> 0.01	> 0.01
$\ln(\mathrm{IP}\ \chi^2)$ of the J/ψ	> 0.5	> 0.5
χ^2 of the vertex fit of the B	< 20	< 40
χ^2 of the primary vertex DTF fit of the B	< 120	< 120

The Receiver Operating Characteristics (ROC) curves for the k-folding are shown in Fig. 5.2. The distributions of the BDT response on the training and testing part of the data sample for the first iteration of the k-folding are given in Fig. 5.3 and for all six iterations in Figs. A.1 and A.2. No significant overtraining is observed. The BDT response for the candiates in the resulting data sample with a mass of $m_B < 5600\,\mathrm{MeV}/c^2$ is an average of the BDT outputs of the k-folding iterations. The cut on the BDT output is optimized such that it maximizes the effective signal size S_{eff}. The signal *sWeights*, s_{w_i}, are calculated with mass fits to the signal candidates as described in Sec. 5.2. The figure of merit is defined as

$$S_{\mathrm{eff}} \equiv \frac{\left(\sum_i s_{w_i}\right)^2}{\sum_i s_{w_i}^2} \tag{5.2}$$

and finds its maximum at a BDT cut of 0.04 in both control channels.

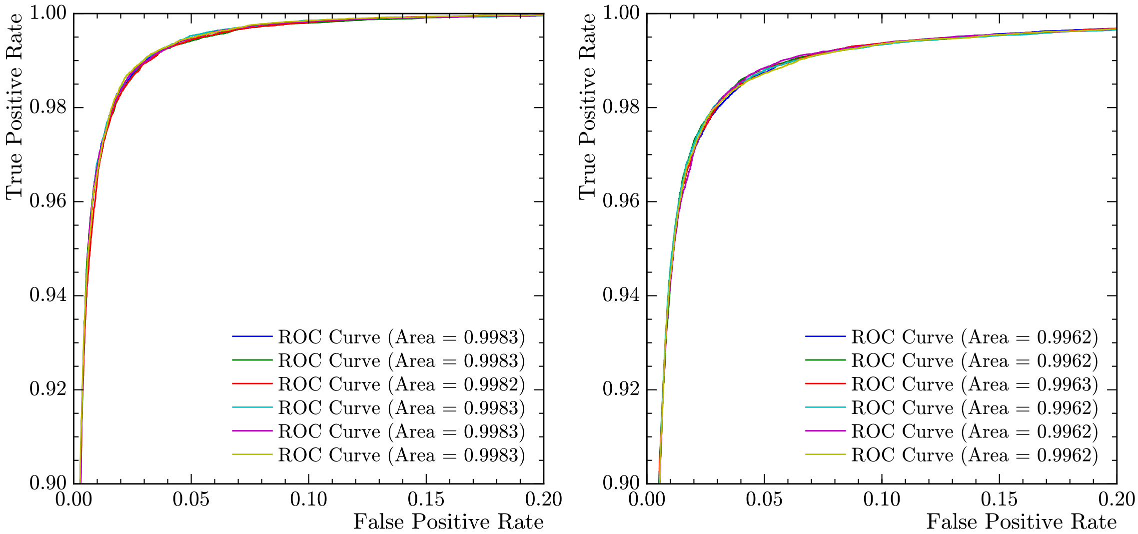

Figure 5.2: ROC curves for the first fold of the trained BDT as evaluated on the testing part for the (left) $B^+ \to J/\psi K^+$ and (right) $B^0 \to J/\psi K^{*0}$ decay channel.

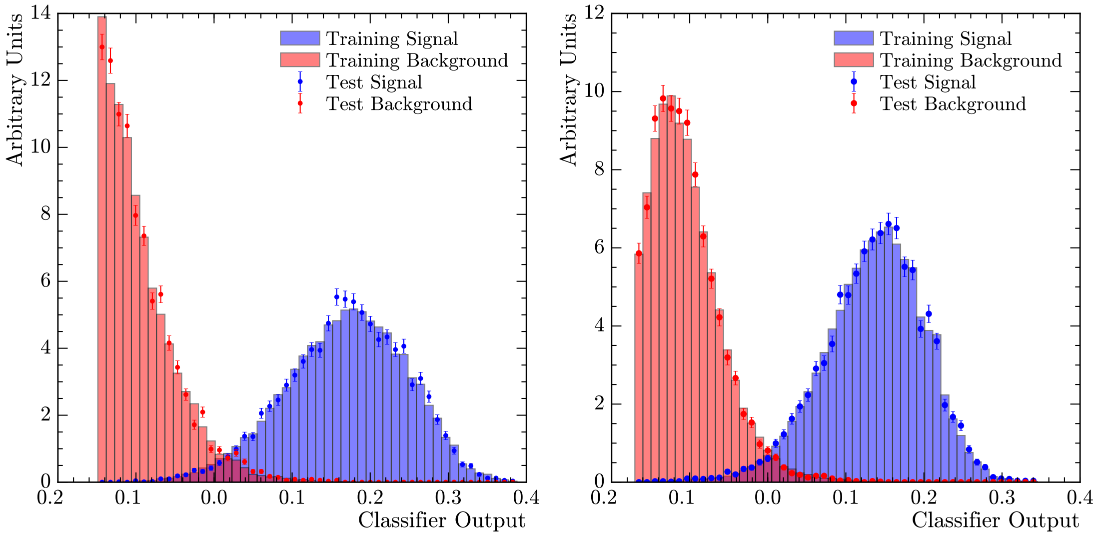

Figure 5.3: BDT classifier output distributions for the first iteration of the k-folding for the (left) $B^+ \to J/\psi K^+$ and (right) $B^0 \to J/\psi K^{*0}$ decay.

5.2 Mass fit

A maximum likelihood fit to the reconstructed invariant mass m of the B candidates is performed after the full selection chain. After the fit *sWeights* are calculated, the FOM is calculated and optimized according to Eq. (5.2). The invariant mass observable is computed with the DecayTreeFitter [68], where the mass of the J/ψ candidates is constrained to the known J/ψ mass. Both considered control channels use the same model for the signal and the combinatorial background as for the $B^0 \to J/\psi K^0_\mathrm{S}$ signal decay channel. The fit model describes the signal component with an Hypatia function [71], and the remaining combinatorial background component with an exponential function. The parameters of the signal shape are obtained from a fit to the simulation sample after a cut on the BDT response of 0.1 has been applied. The corresponding fits to the simulation can be found in Fig. 5.4. The Hypatia PDF is described by

$$
\mathcal{I}(m;\mu,\sigma,\lambda,\zeta,\beta,a_1,n_1,a_2,n_2) \propto
\begin{cases}
((m-\mu)^2 + A^2_\lambda(\zeta)\sigma^2)^{\frac{1}{2}\lambda-\frac{1}{4}} e^{\beta(m-\mu)} K_{\lambda-\frac{1}{2}}\left(\zeta\sqrt{1+\left(\frac{m-\mu}{A_\lambda(\zeta)\sigma}\right)^2}\right) & , -a_1 < \frac{m-\mu}{\sigma} < a_2 \\
\frac{G(\mu-a_1\sigma,\mu,\sigma,\lambda,\zeta,\beta)}{\left(1-m/\left(n\frac{G(\mu-a_1\sigma,\mu,\sigma,\lambda,\zeta,\beta)}{G'(\mu-a_1\sigma,\mu,\sigma,\lambda,\zeta,\beta)}-a_1\sigma\right)\right)^{n_1}} & , -a_1 > \frac{m-\mu}{\sigma} \\
\frac{G(\mu-a_2\sigma,\mu,\sigma,\lambda,\zeta,\beta)}{\left(1-m/\left(n\frac{G(\mu-a_2\sigma,\mu,\sigma,\lambda,\zeta,\beta)}{G'(\mu-a_2\sigma,\mu,\sigma,\lambda,\zeta,\beta)}-a_2\sigma\right)\right)^{n_2}} & , \quad a_2 < \frac{m-\mu}{\sigma} ,
\end{cases}
\tag{5.3}
$$

with

$$G(m;\mu,\sigma,\lambda,\zeta,\beta) = \\ ((m-\mu)^2 + A_\lambda^2(\zeta)\sigma^2)^{\frac{1}{2}\lambda-\frac{1}{4}} e^{\beta(m-\mu)} K_{\lambda-\frac{1}{2}}\left(\zeta\sqrt{1+\left(\frac{m-\mu}{A_\lambda(\zeta)\sigma}\right)^2}\right) , \quad (5.4)$$

and

$$A_\lambda^2(\zeta) = \frac{\zeta K_\lambda(\zeta)}{K_{\lambda+1}(\zeta)}. \quad (5.5)$$

Here, G is the generalized hyperbolic distribution, G' the derivative of G, and K_λ are cylindrical harmonics. The distribution is described by a mean, μ, and a width, σ, and the parameters a_{i}, n_{i} which take account for possible exponential tails. The parameters ζ and β are set to zero to obtain an analytically integrable function. The parameters, which were determined with the fit to the signal simulation, are fixed except a_1 and a_2 to describe the distributions' tails on data. Combinatorial background is modeled with an exponential function described by the parameter a_{exp}. The mass fits for the $B^+ \to J/\psi K^+$ and $B^0 \to J/\psi K^{*0}$ decay are shown in Fig. 5.5 and the corresponding parameters are given in Table 5.3. The number of signal candidates determined from these fits are $N_{B^+} = 226\,757 \pm 611$ for the $B^+ \to J/\psi K^+$ decay and $N_{B^0} = 82\,709 \pm 430$ for the $B^0 \to J/\psi K^{*0}$ decay.

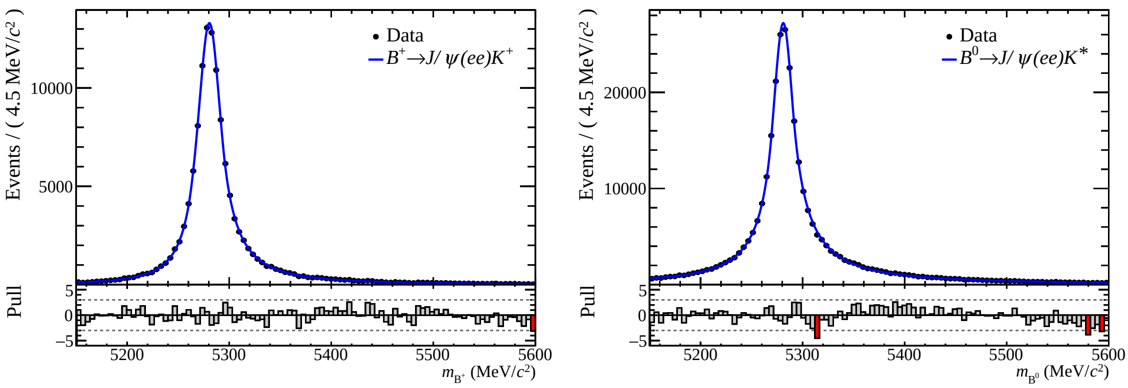

Figure 5.4: Mass fit of the constrained B mass on signal simulation to yield parameters of the signal distribution shape for the (left) $B^+ \to J/\psi K^+$ decay and the (right) $B^0 \to J/\psi K^{*0}$ decay.

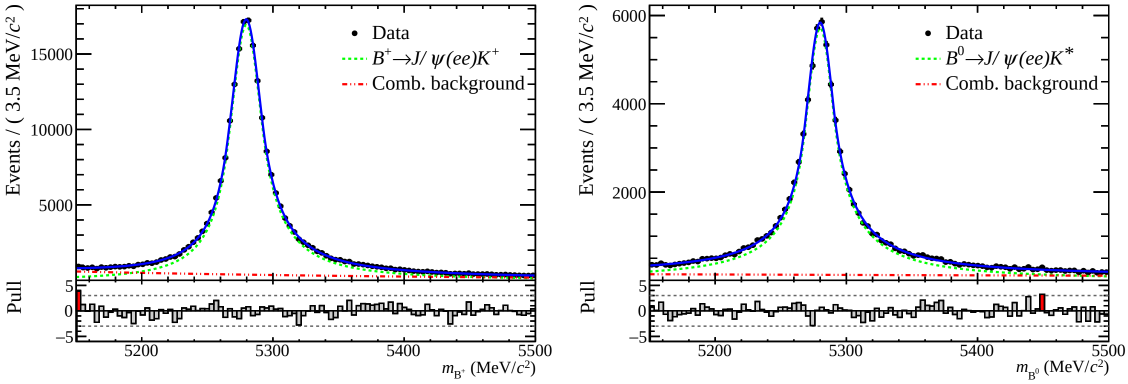

Figure 5.5: Nominal massfit to the constrained B mass to calculate $s\mathcal{W}eights$ for the (left) $B^+ \to J/\psi K^+$ decay and for the (right) $B^0 \to J/\psi K^{*0}$ decay.

Table 5.3: Results of the nominal mass fit for the $B^+ \to J/\psi K^+$ and $B^0 \to J/\psi K^{*0}$ decay channels.

	$B^+ \to J/\psi K^+$	$B^0 \to J/\psi K^{*0}$
a_1	0.226 ± 0.004	0.17069
a_2	0.2234 ± 0.0027	0.14445
n_1	2.3722	1.6907
n_2	2.0015	1.6198
β	0.0	0.0
ζ	0.0	0.0
λ	-1.061	-1.03443
σ	$(56.8 \pm 0.4)\,\mathrm{MeV}/c^2$	$(70.0 \pm 0.1)\,\mathrm{MeV}/c^2$
μ_B	$(5279.6 \pm 0.1)\,\mathrm{MeV}/c^2$	$(5280.0 \pm 0.1)\,\mathrm{MeV}/c^2$
N_B	$226\,757 \pm 611$	$82\,709 \pm 430$
$N_{\mathrm{comb.bkg}}$	$34\,043 \pm 496$	$14\,344 \pm 341$
$a_{\mathrm{exp.}}$	$(-0.00343 \pm 0.00010)\,(\mathrm{MeV}/c^2)^{-1}$	$(-0.00224 \pm 0.00013)\,(\mathrm{MeV}/c^2)^{-1}$

5.3 Flavour-tagging calibration on the control channels

The mistag correction function, $\omega(\eta)$ is determined using the self-tagged $B^+ \to J/\psi K^+$ decay channel for the OS taggers and the flavour-specific $B^0 \to J/\psi K^{*0}$ decay channel for the SS taggers.

The single taggers are first calibrated on one half of the corresponding selected calibration sample. After the single tagger calibration the taggers are combined and the combination is calibrated on the other half of the sample. The first uncertainties of the flavour-tagging parameters are statistical and the second are systematic uncertainties due to the calibration.

The calibrated flavour-tagging performances for the OS single taggers and the OS combination tagger are listed in Table 5.4. Calibration plots for the single taggers and the tagger combination are shown in Figs. 5.6 to 5.8. Here, ten categories of η are used following the standard choice of the EspressoPerformanceManager. The green band in the plots shows the error band corresponding to one standard deviation and the yellow band represents an error of two standard deviations. The corresponding calibration parameters are listed in Table 5.5 and the correlations of the calibration parameters can be found in Tables 5.6 to 5.8. The OS combination shows a calibrated tagging efficiency of $\epsilon = (37.23 \pm 0.17)\%$ and an effective tagging efficiency of $\epsilon\langle D^2\rangle = (3.432 \pm 0.026 \pm 0.115)\%$. The calibration parameters have a value of $p_0 = 0.3725 \pm 0.0028$ and $p_1 = 0.842 \pm 0.024$ with an average predicted mistag probability of $\langle\eta\rangle = 0.34$. The calibration parameters p_0 and p_1 show a deviation of 6.6 standard deviations and 11.6 standard deviations from a perfect calibration. For the single taggers the effective tagging efficiency varies beween $(0.399 \pm 0.009 \pm 0.041)\%$ for the OS electron tagger and $(1.353 \pm 0.012 \pm 0.079)\%$ for the OS vertex charge tagger. The effective tagging efficiency depends on the tagging efficiency ϵ. Due to its inclusive design approach, as described in Sec. 4.2, the OS vertex charge tagger shows the highest tagging efficiency of the OS taggers. The OS kaon tagger shows a higher tagging efficiency in comparison to the lepton taggers. This can be explained by the higher probability of a B meson to decay into a kaon than into a lepton. The OS muon tagger has a higher tagging efficiency than the OS electron tagger because of the detector's enhanced ability to detect muons with its muon system.

Table 5.4: Flavour-tagging performances for the $B^+ \to J/\psi K^+$ decay.

Tagger	ϵ	ω	$\epsilon\langle D^2\rangle = \epsilon\,(1-2\omega)^2$
OS charm	$(4.74 \pm 0.08)\%$	$(34.44 \pm 0.07 \pm 0.78)\%$	$(0.459 \pm 0.008 \pm 0.046)\%$
OS muon	$(7.64 \pm 0.09)\%$	$(29.43 \pm 0.08 \pm 0.56)\%$	$(1.293 \pm 0.018 \pm 0.071)\%$
OS electron	$(2.93 \pm 0.06)\%$	$(31.5 \pm 0.1 \pm 1.0)\%$	$(0.399 \pm 0.009 \pm 0.041)\%$
OS kaon	$(18.51 \pm 0.14)\%$	$(37.69 \pm 0.04 \pm 0.34)\%$	$(1.123 \pm 0.011 \pm 0.073)\%$
OS vertex charge	$(20.93 \pm 0.14)\%$	$(37.29 \pm 0.04 \pm 0.37)\%$	$(1.353 \pm 0.012 \pm 0.079)\%$
OS Combination	$(37.23 \pm 0.17)\%$	$(34.82 \pm 0.05 \pm 0.25)\%$	$(3.432 \pm 0.026 \pm 0.115)\%$

Table 5.5: Flavour-tagging calibration parameters for the $B^+ \to J/\psi K^+$ decay.

Tagger	p_0	p_1	Δp_0	Δp_1	$\langle\eta\rangle$
OS charm	0.352 ± 0.008	1.02 ± 0.16	0.028 ± 0.016	0.49 ± 0.33	0.4
OS muon	0.309 ± 0.006	0.86 ± 0.06	-0.020 ± 0.012	-0.13 ± 0.13	0.29
OS electron	0.32 ± 0.01	0.89 ± 0.14	0.012 ± 0.020	0.25 ± 0.28	0.29
OS kaon	0.389 ± 0.004	0.94 ± 0.07	0.036 ± 0.008	0.07 ± 0.13	0.4
OS vertex charge	0.389 ± 0.004	1.00 ± 0.06	0.008 ± 0.008	0.01 ± 0.12	0.4
OS Combination	0.3725 ± 0.0028	0.842 ± 0.024	0.015 ± 0.006	-0.00 ± 0.05	0.34

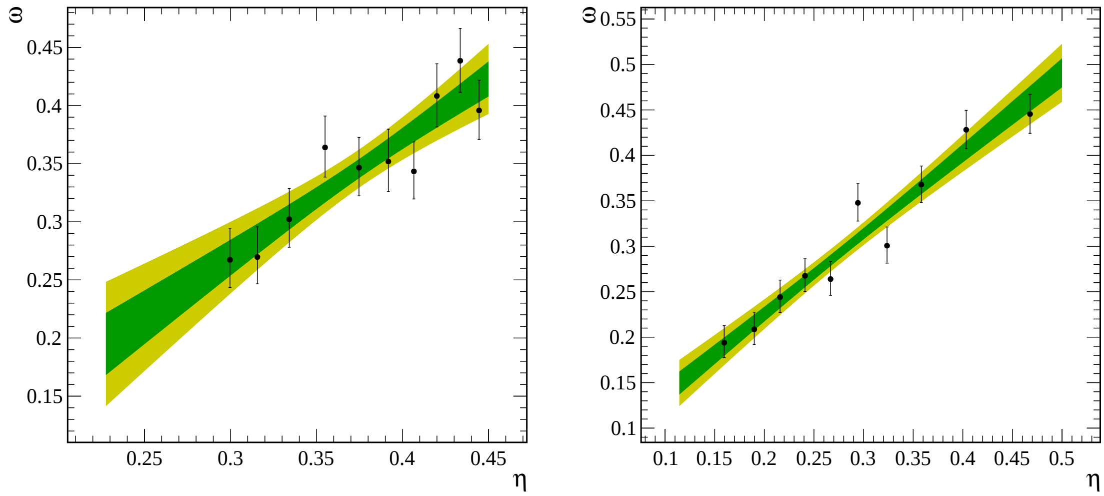

Figure 5.6: Flavour-tagging calibration for the $B^+ \to J/\psi K^+$ decay for the (left) OS charm tagger and the (right) OS muon tagger.

Table 5.6: Correlation matrix of the flavour-tagging parameters of the (left) OS charm tagger and the (right) OS muon tagger for the $B^+ \to J/\psi K^+$ decay.

	p_0	p_1	Δp_0	Δp_1
p_0	1	0.06	0.032	0.027
p_1		1	0.027	0.034
Δp_0			1	0.06
Δp_1				1

	p_0	p_1	Δp_0	Δp_1
p_0	1	0.13	-0.015	0.014
p_1		1	0.014	-0.016
Δp_0			1	0.13
Δp_1				1

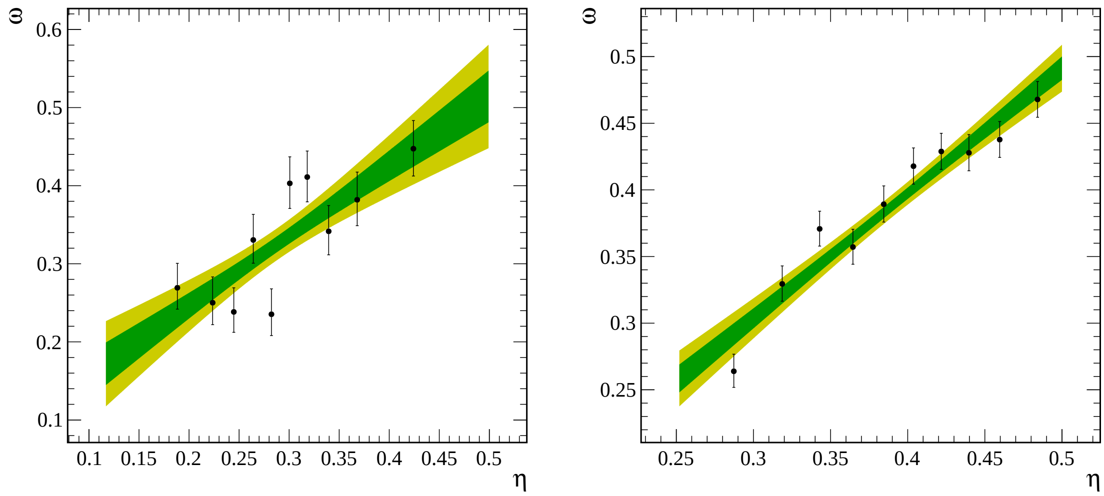

Figure 5.7: Flavour-tagging calibration with the $B^+ \to J/\psi K^+$ decay for the (left) OS electron tagger and the (right) OS kaon tagger.

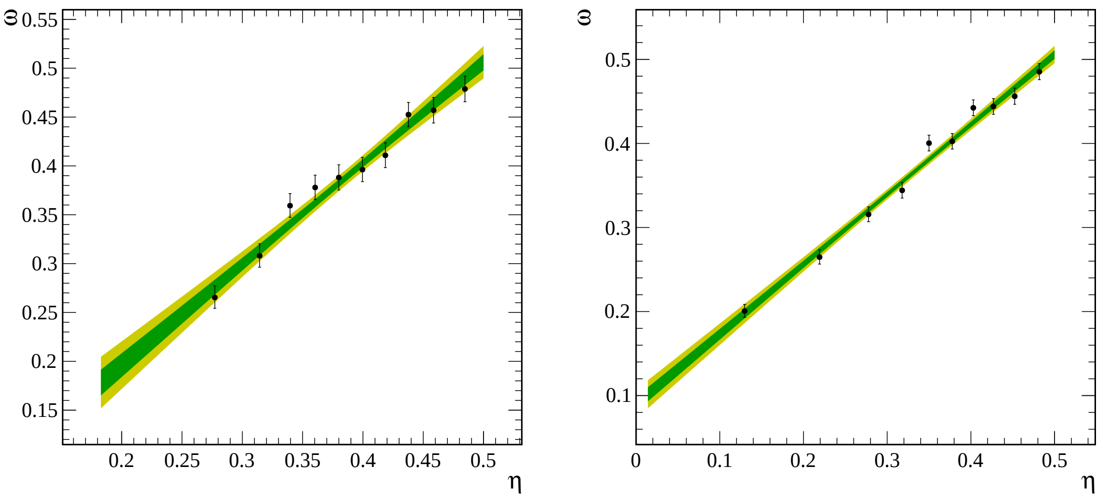

Figure 5.8: Flavour-tagging calibration for the $B^+ \to J/\psi K^+$ decay for the (left) OS vertex charge tagger and the (right) OS combination tagger.

Table 5.7: Correlation matrix of the flavour-tagging parameters of the (left) OS electron tagger and for the (right) OS kaon tagger for the $B^+ \to J/\psi K^+$ decay.

	p_0	p_1	Δp_0	Δp_1
p_0	1	0.10	0.028	0.015
p_1		1	0.015	0.09
Δp_0			1	0.10
Δp_1				1

	p_0	p_1	Δp_0	Δp_1
p_0	1	0.035	0.008	0.005
p_1		1	0.005	0.008
Δp_0			1	0.035
Δp_1				1

Table 5.8: Correlation matrix of the flavour-tagging parameters of the (left) OS vertex charge tagger and the (right) OS combination tagger for the $B^+ \to J/\psi K^+$ decay.

	p_0	p_1	Δp_0	Δp_1
p_0	1	0.05	−0.0035	0.013
p_1		1	0.013	0.0007
Δp_0			1	0.005
Δp_1				1

	p_0	p_1	Δp_0	Δp_1
p_0	1	0.13	0.006	−0.015
p_1		1	−0.015	0.05
Δp_0			1	0.13
Δp_1				1

The calibrated flavour-tagging performances for the SS single taggers and the SS combination tagger are listed in Table 5.9. The calibration plots of the single taggers and the tagger combination are shown in Figs. 5.9 and 5.10. The corresponding calibration parameters are listed in Table 5.10 and the correlations of the calibration parameters can be found in Tables 5.11 and 5.12. The SS combination has a calibrated tagging efficiency of $\epsilon = (74.35 \pm 0.28)\%$ and a effective tagging efficiency of $\epsilon\langle D^2\rangle = (2.275 \pm 0.026 \pm 0.255)\%$. The calibration parameters p_0 and p_1 show a deviation of 2.63 standard deviations and 0.1 standard deviations from a perfect calibration. The SS pion tagger shows an effective tagging efficiency $\epsilon\langle D^2\rangle$ of $(1.566 \pm 0.016 \pm 0.214)\%$ with a high tagging efficiency ϵ of $(70.61 \pm 0.28)\%$, compared to the OS tagger tagging efficiencies. The SS proton tagger has a lower effective tagging efficiency of $(0.325 \pm 0.007 \pm 0.101)\%$ and a tagging efficiency of $(36.02 \pm 0.30)\%$. This can be explained by the lower hadronization probability of a proton, compared to a pion. In comparison to the OS taggers the tagging efficiency of the SS taggers is significantly higher, because of their inclusive design, as described in Sec. 4.2.

Table 5.9: Flavour-tagging performances for the $B^0 \to J/\psi K^{*0}$ decay.

Tagger	ϵ	ω	$\epsilon\langle D^2\rangle = \epsilon\,(1-2\omega)^2$
SS pion	$(70.61 \pm 0.28)\%$	$(42.55 \pm 0.04 \pm 0.51)\%$	$(1.566 \pm 0.016 \pm 0.214)\%$
SS proton	$(36.02 \pm 0.30)\%$	$(45.25 \pm 0.05 \pm 0.74)\%$	$(0.325 \pm 0.007 \pm 0.101)\%$
SS Combination	$(74.35 \pm 0.28)\%$	$(41.25 \pm 0.05 \pm 0.49)\%$	$(2.275 \pm 0.026 \pm 0.255)\%$

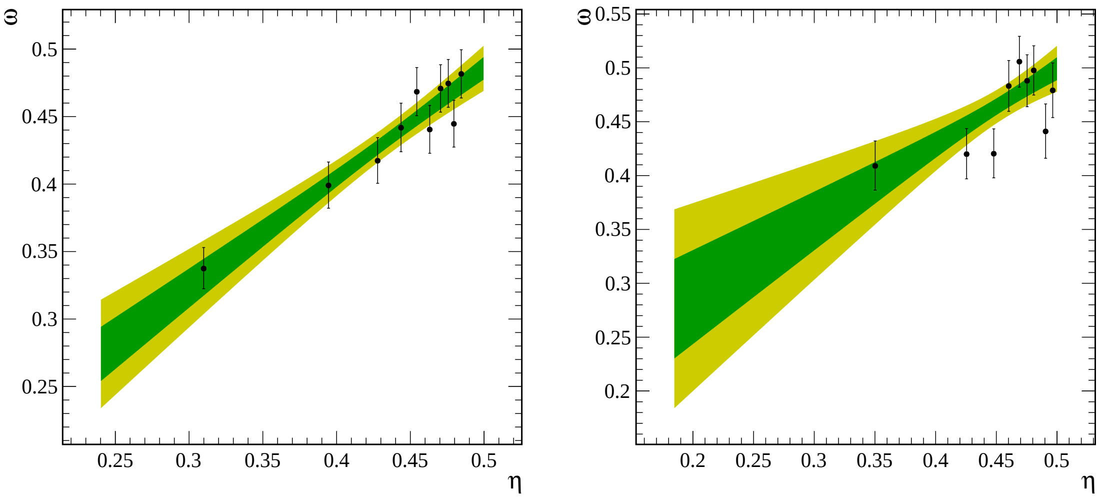

Figure 5.9: Flavour-tagging calibration for the $B^0 \to J/\psi K^{*0}$ decay for the (left) SS pion tagger and the (right) SS proton tagger.

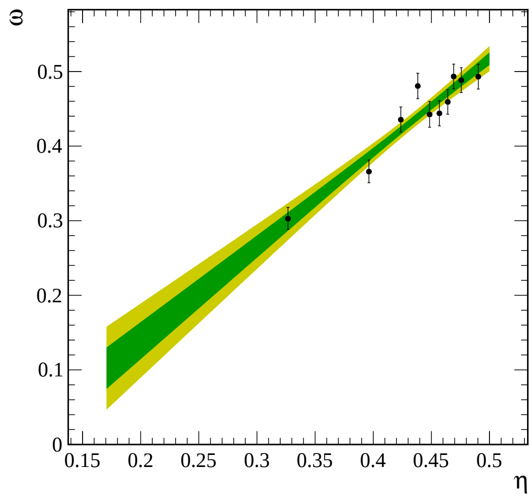

Figure 5.10: Flavour-tagging calibration for the $B^0 \to J/\psi\, K^{*0}$ decay for the SS combination tagger.

Table 5.10: Flavour-tagging calibration parameters for the $B^0 \to J/\psi\, K^{*0}$ decay.

Tagger	p_0	p_1	Δp_0	Δp_1	$\langle\eta\rangle$
SS pion	0.441 ± 0.005	0.83 ± 0.09	0.006 ± 0.007	0.21 ± 0.13	0.4
SS proton	0.470 ± 0.007	0.78 ± 0.16	0.021 ± 0.010	-0.23 ± 0.22	0.5
SS Combination	0.441 ± 0.005	1.26 ± 0.10	0.008 ± 0.007	0.05 ± 0.14	0.4

Table 5.11: Correlation matrix of the flavour-tagging parameters of the (left) SS pion tagger and the (right) SS proton tagger for the $B^0 \to J/\psi\, K^{*0}$ decay.

	p_0	p_1	Δp_0	Δp_1
p_0	1	0.07	0.0031	−0.008
p_1		1	−0.008	0.014
Δp_0			1	0.028
Δp_1				1

	p_0	p_1	Δp_0	Δp_1
p_0	1	0.04	0.006	−0.022
p_1		1	−0.023	0.07
Δp_0			1	0.018
Δp_1				1

Table 5.12: Correlation matrix of the flavour-tagging parameters of the SS combination tagger for the $B^0 \to J/\psi\, K^{*0}$ decay.

	p_0	p_1	Δp_0	Δp_1
p_0	1	0.7	−0.026	0.012
p_1		1	0.013	−0.07
Δp_0			1	0.029
Δp_1				1

5.4 Flavour-tagging calibration for $B^0 \to J/\psi K^0_S$

The flavour-tagging results of the control channels depend on kinematic observables, which are the pseudo-rapidity, η, the angle, ϕ, the number of primary vertices, nPV, the number of tracks, nTracks, and the transverse momentum of the B candidate, p_T. In order to employ the flavour-tagging calibration from the control channels to calibrate the signal channel a reweighting in these observables has to be performed. A multidimensional reweighting algorithm which works with Boosted Decision Trees is used [72].

The typical approach for reweighting is to split the variables' phase spaces into bins and calculate a multiplier w to compensate the difference between the target and the original distributions. The method of Gradient Boosting Reweighting uses Boosted Decision Trees to find phase space regions in which the reweighting is performed. They are represented as leaves of the Decision Trees where the symmetrized χ^2 gives a measure of the difference between the target and the original distribution with

$$\chi^2 = \sum_{\text{leaf}} \frac{(w_{\text{leaf,original}} - w_{\text{leaf,target}})^2}{w_{\text{leaf,original}} + w_{\text{leaf,target}}} . \tag{5.6}$$

Because a high χ^2 indicates that reweighting is needed, it is maximized with the Boosted Decision Tree. The original distribution is reweighted iteratively: A shallow tree to maximize the χ^2 and thus to find the bins where reweighting is needed is build. Then the original distribution is reweighting using the weight w and the procedure is repeated. After the training of the Decision Trees the predictions for each tree are summed. The final weight is obtained as the product of the contributions of the various trees.

A comparison between the $B^0 \to J/\psi K^0_S$ signal channel and the reweighted $B^+ \to J/\psi K^+$ and $B^0 \to J/\psi K^{*0}$ control channels is shown in Fig. 5.11 and Fig. 5.12. After the reweighting the distributions are in good agreement. See Sec. 5.5 for a determination of the systematic uncertainties coming from the reweighting.

The calibrated flavour-tagging performances for the OS single taggers and the OS combination tagger for the reweighted control channels are listed in Table 5.13. The calibration plots of the single taggers and the tagger combination are shown in Figs. 5.13 to 5.15. The corresponding calibration parameters are listed in Table 5.14 and the correlations of the calibration parameters can be seen in Tables 5.15 to 5.17. The reweighted OS combination has a calibrated tagging efficiency of $\epsilon = (36.52 \pm 0.18)\%$ and a effective tagging efficiency of $\epsilon\langle D^2\rangle = (3.414 \pm 0.026 \pm 0.118)\%$. The calibration parameters p_0 and p_1 show a deviation of 7.3 standard deviations and 11.0 standard deviations from a perfect calibration.

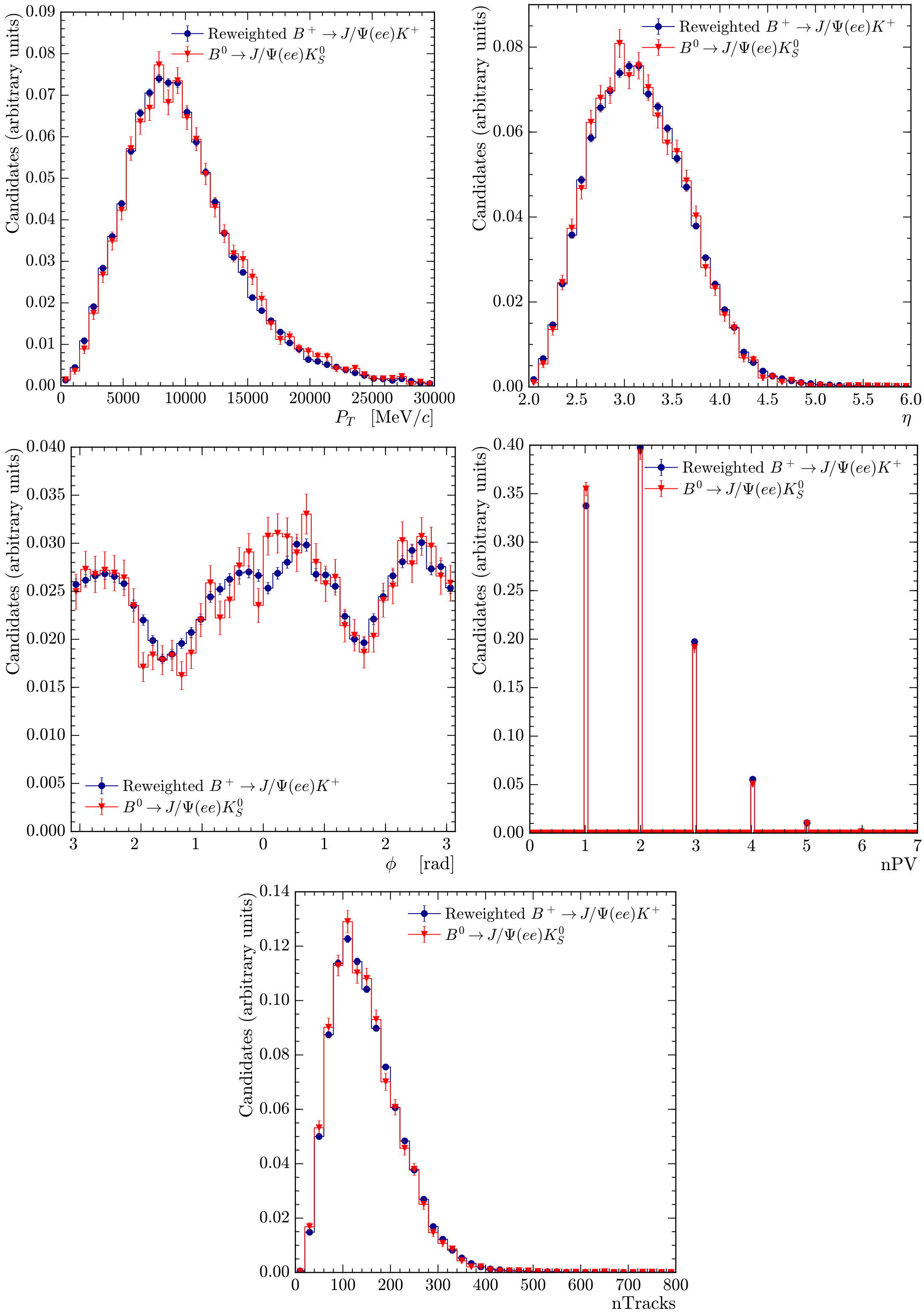

Figure 5.11: Flavour-tagging related observables of the (blue) reweighted $B^+ \to J/\psi K^+$ decay channel to match the (red) $B^0 \to J/\psi K^0_S$ signal channel .

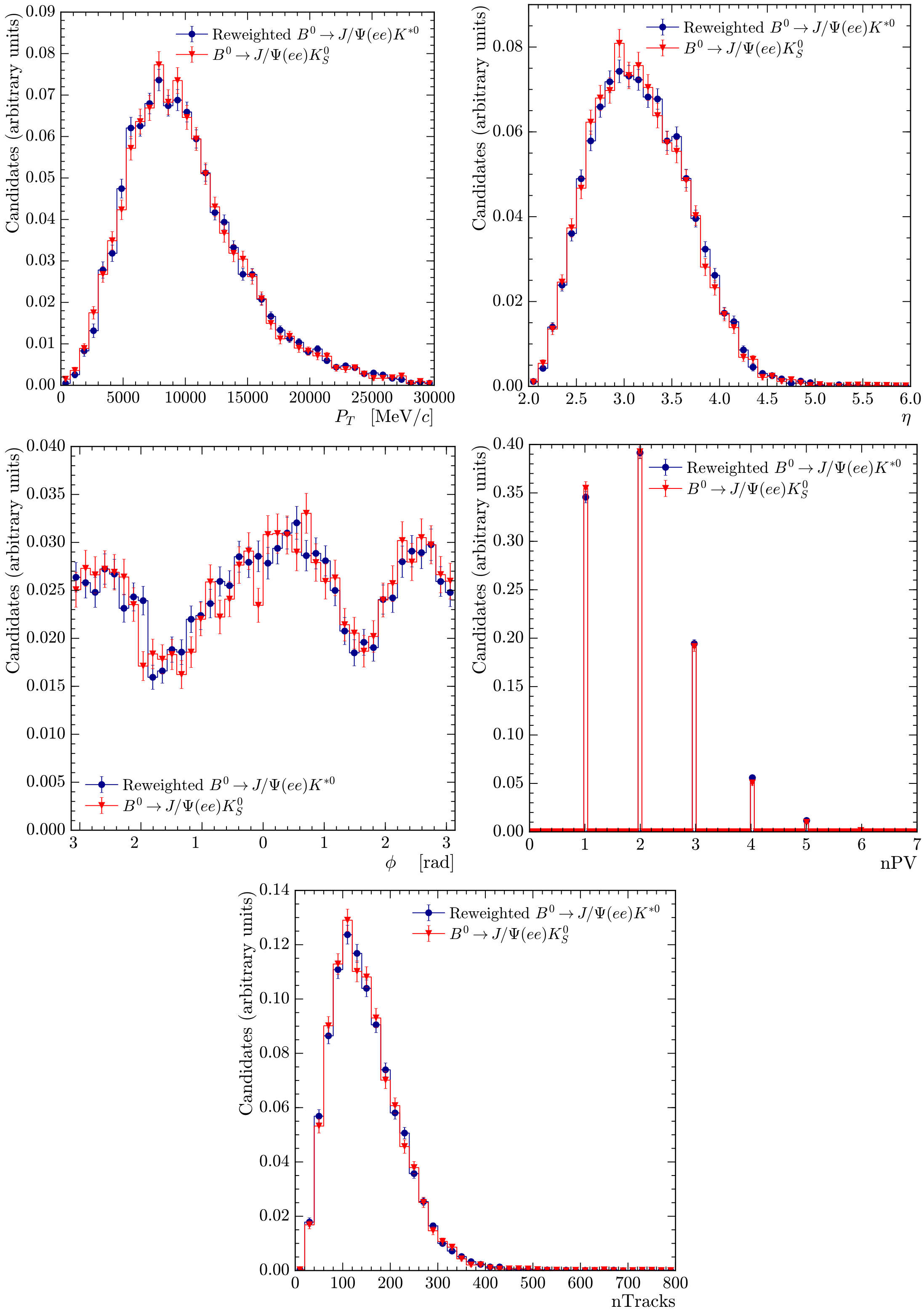

Figure 5.12: Flavour-tagging related observables of the (blue) reweighted $B^0 \to J/\psi\, K^{*0}$ decay channel to match the (red) $B^0 \to J/\psi\, K^0_S$ signal channel .

Table 5.13: Flavour-tagging performances for the reweighted $B^+ \to J/\psi K^+$ decay.

Tagger	ε	$\langle\omega\rangle$	$\varepsilon\langle D^2\rangle = \varepsilon\,(1-2\omega)^2$
OS charm	$(4.69 \pm 0.08)\%$	$(34.12 \pm 0.06 \pm 0.81)\%$	$(0.473 \pm 0.009 \pm 0.049)\%$
OS muon	$(7.16 \pm 0.10)\%$	$(29.29 \pm 0.08 \pm 0.58)\%$	$(1.228 \pm 0.019 \pm 0.069)\%$
OS electron	$(2.88 \pm 0.06)\%$	$(31.94 \pm 0.09 \pm 0.99)\%$	$(0.376 \pm 0.009 \pm 0.041)\%$
OS kaon	$(18.166 \pm 0.142)\%$	$(37.536 \pm 0.036 \pm 0.417)\%$	$(1.129 \pm 0.011 \pm 0.076)\%$
OS vertex charge	$(20.15 \pm 0.15)\%$	$(36.98 \pm 0.04 \pm 0.39)\%$	$(1.367 \pm 0.013 \pm 0.082)\%$
OS Combination	$(36.52 \pm 0.18)\%$	$(34.71 \pm 0.04 \pm 0.26)\%$	$(3.414 \pm 0.026 \pm 0.118)\%$

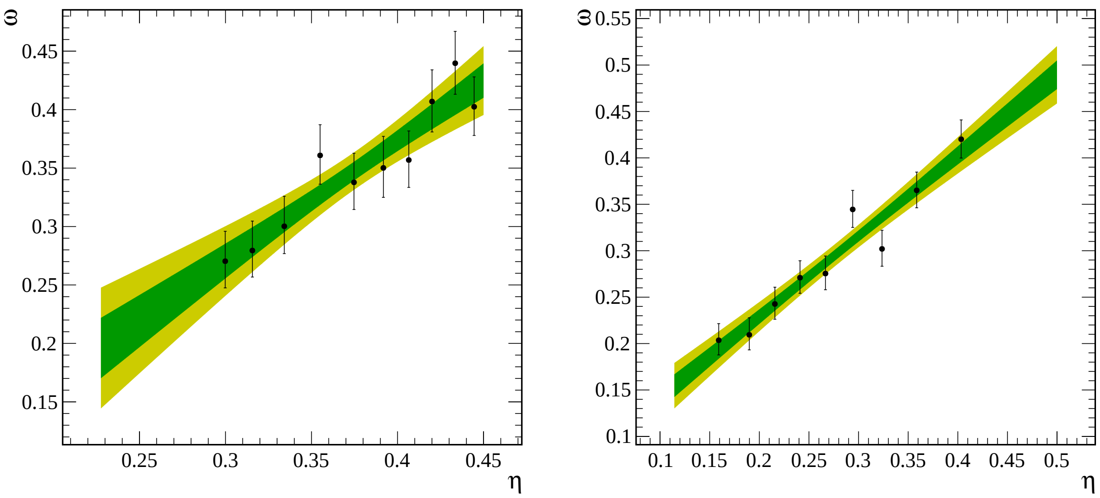

Figure 5.13: Flavour-tagging calibration for the reweighted $B^+ \to J/\psi K^+$ decay for the (left) OS charm tagger and the (right) OS muon tagger.

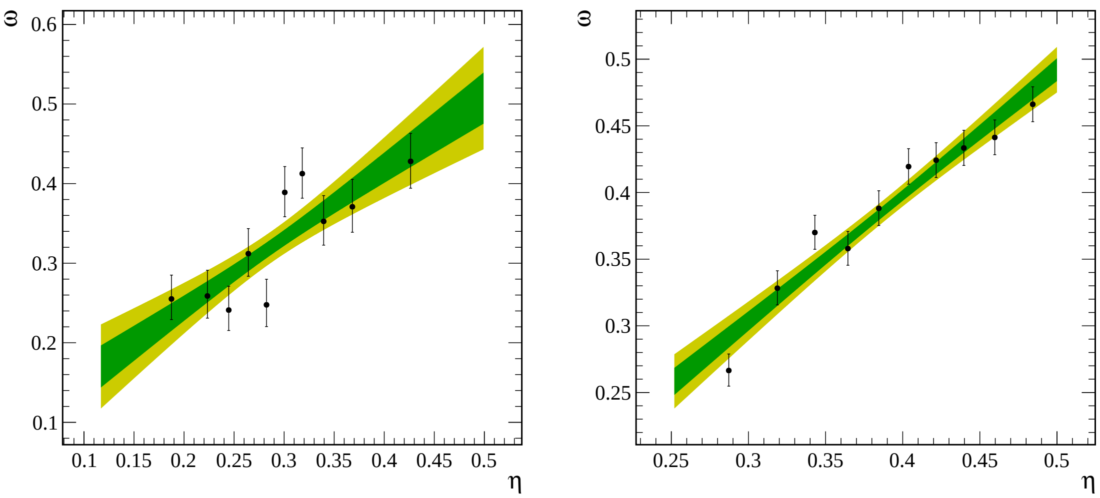

Figure 5.14: Flavour-tagging calibration for the reweighted $B^+ \to J/\psi K^+$ decay for the (left) OS electron tagger and the (right) OS kaon tagger.

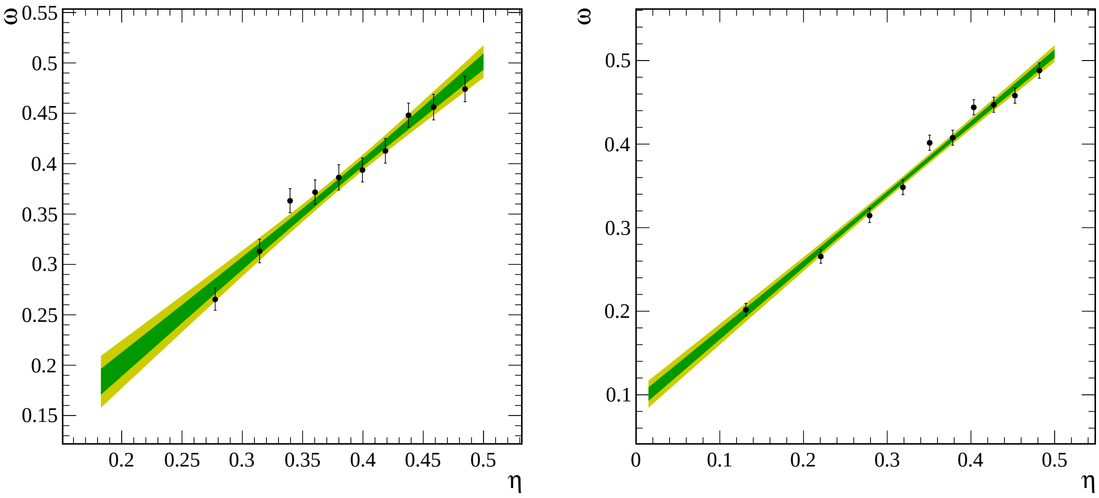

Figure 5.15: Flavour tagging calibration for the reweighted $B^+ \to J/\psi\, K^+$ decay for the (left) OS vertex charge tagger and the (right) OS combination tagger.

Table 5.14: Flavour-tagging calibration parameters for the reweighted $B^+ \to J/\psi\, K^+$ decay.

Tagger	p_0	p_1	Δp_0	Δp_1	$\langle\eta\rangle$
OS charm	0.349 ± 0.008	1.03 ± 0.17	0.028 ± 0.016	0.4 ± 0.3	0.4
OS muon	0.314 ± 0.006	0.89 ± 0.07	-0.022 ± 0.012	-0.10 ± 0.13	0.30
OS electron	0.327 ± 0.010	0.90 ± 0.15	0.002 ± 0.020	0.09 ± 0.30	0.29
OS kaon	0.389 ± 0.004	0.94 ± 0.07	0.036 ± 0.008	0.06 ± 0.14	0.4
OS vertex charge	0.388 ± 0.004	1.03 ± 0.06	0.006 ± 0.008	0.02 ± 0.13	0.4
OS Combination	0.3760 ± 0.0029	0.832 ± 0.025	0.016 ± 0.006	-0.02 ± 0.05	0.34

Table 5.15: Correlation matrix of flavour-tagging parameters of the (left) OS charm Tagger and the (right) OS muon tagger for the reweighted $B^+ \to J/\psi\, K^+$ decay.

	p_0	p_1	Δp_0	Δp_1
p_0	1	0.04	0.024	0.028
p_1		1	0.028	0.026
Δp_0			1	0.04
Δp_1				1

	p_0	p_1	Δp_0	Δp_1
p_0	1	0.16	-0.021	0.012
p_1		1	0.012	-0.021
Δp_0			1	0.16
Δp_1				1

Table 5.16: Correlation matrix of flavour-tagging parameters of the (left) OS electron tagger and the (right) OS kaon tagger for the reweighted $B^+ \to J/\psi K^+$ decay.

	p_0	p_1	Δp_0	Δp_1
p_0	1	0.09	0.019	0.009
p_1		1	0.009	0.09
Δp_0			1	0.09
Δp_1				1

	p_0	p_1	Δp_0	Δp_1
p_0	1	0.024	0.004	−0.004
p_1		1	−0.004	−0.011
Δp_0			1	0.024
Δp_1				1

Table 5.17: Correlation matrix of flavour-tagging parameters of the (left) OS vertex charge tagger and the (right) OS combination tagger for the reweighted $B^+ \to J/\psi K^+$ decay.

	p_0	p_1	Δp_0	Δp_1
p_0	1	0.031	−0.012	0.014
p_1		1	0.014	−0.0017
Δp_0			1	0.04
Δp_1				1

	p_0	p_1	Δp_0	Δp_1
p_0	1	0.13	0.009	−0.021
p_1		1	−0.021	0.06
Δp_0			1	0.13
Δp_1				1

The calibrated flavour-tagging performances for the SS single taggers, and the SS combination tagger for the reweighted control channels are listed in Table 5.18. The calibration plots of the single taggers and the tagger combination are shown in Figs. 5.16 and 5.17. The corresponding calibration parameters are listed in Table 5.19 and the correlations of the calibration parameters can be seen in Tables 5.20 and 5.21. The reweighted SS combination has a calibrated tagging efficiency of $\epsilon = (73.66 \pm 0.30)\%$ and a effective tagging efficiency of $\epsilon\langle D^2\rangle = (2.223 \pm 0.024 \pm 0.258)\%$. The calibration parameters p_0 and p_1 show a deviation of 2.6 standard deviations and 0.1 standard deviations from a perfect calibration.

Table 5.18: Flavour-tagging performances for the reweighted $B^0 \to J/\psi K^{*0}$ decay.

Tagger	ε	$\langle\omega\rangle$	$\varepsilon\langle D^2\rangle = \varepsilon\,(1-2\omega)^2$
SS pion	$(69.4 \pm 0.3)\%$	$(42.505 \pm 0.032 \pm 0.524)\%$	$(1.559 \pm 0.015 \pm 0.218)\%$
SS proton	$(38.54 \pm 0.32)\%$	$(45.72 \pm 0.04 \pm 0.74)\%$	$(0.282 \pm 0.006 \pm 0.098)\%$
SS Combination	$(73.66 \pm 0.30)\%$	$(41.31 \pm 0.04 \pm 0.503)\%$	$(2.223 \pm 0.024 \pm 0.258)\%$

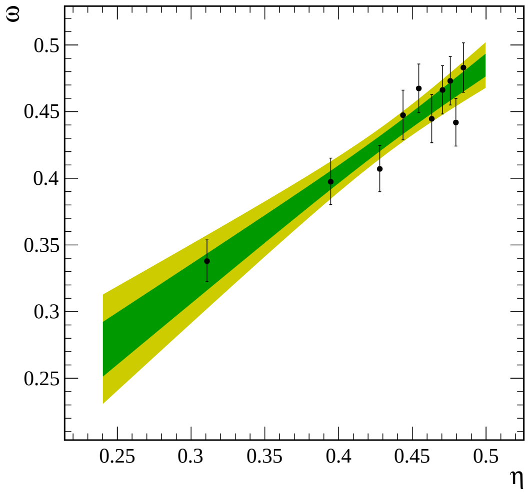

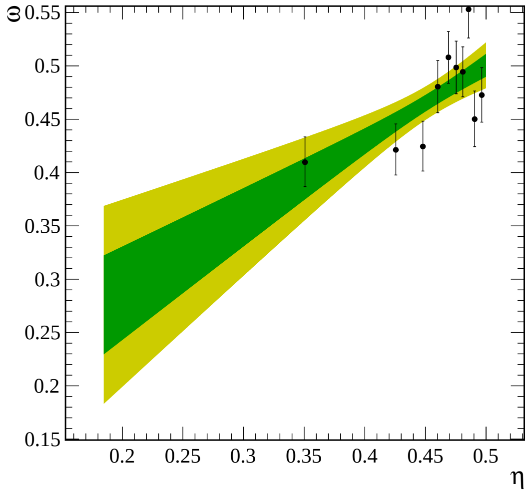

Figure 5.16: Flavour-tagging calibration for the reweighted $B^0 \to J/\psi\, K^{*0}$ decay for the (left) SS pion tagger and the (right) SS proton tagger.

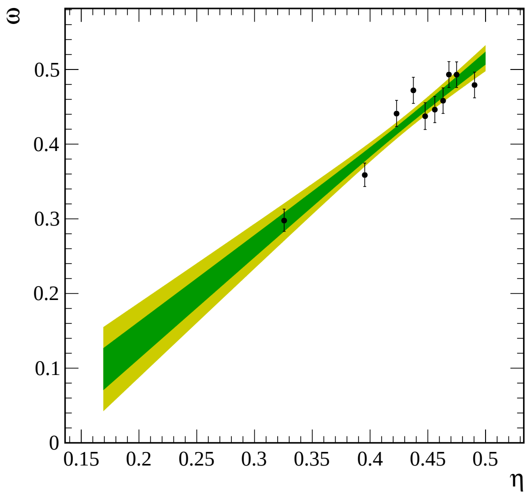

Figure 5.17: Flavour-tagging calibration for the reweighted $B^0 \to J/\psi\, K^{*0}$ decay for the SS combination tagger.

Table 5.19: Flavour-tagging calibration parameters for the reweighted $B^0 \to J/\psi\, K^{*0}$ decay.

Tagger	p_0	p_1	Δp_0	Δp_1	$\langle\eta\rangle$
SS pion	0.438 ± 0.006	0.82 ± 0.10	0.006 ± 0.008	0.22 ± 0.14	0.4
SS proton	0.472 ± 0.008	0.71 ± 0.17	0.027 ± 0.011	-0.30 ± 0.23	0.5
SS Combination	0.440 ± 0.005	1.26 ± 0.10	0.006 ± 0.007	0.06 ± 0.15	0.4

Table 5.20: Correlation matrix of the flavour-tagging parameters of the (left) SS pion tagger and the (right) SS proton tagger for the reweighted $B^0 \to J/\psi K^{*0}$ decay.

	p_0	p_1	Δp_0	Δp_1
p_0	1	0.11	0.005	−0.009
p_1		1	−0.009	0.018
Δp_0			1	0.07
Δp_1				1

	p_0	p_1	Δp_0	Δp_1
p_0	1	0.06	0.006	−0.021
p_1		1	−0.022	0.08
Δp_0			1	0.034
Δp_1				1

Table 5.21: Correlation matrix of the flavour-tagging parameters of the SS combination tagger for the reweighted $B^0 \to J/\psi K^{*0}$ decay.

	p_0	p_1	Δp_0	Δp_1
p_0	1	0.11	−0.025	0.016
p_1		1	0.017	−0.08
Δp_0			1	0.07
Δp_1				1

To propagate the uncertainties of the flavour-tagging calibration to the *CP* fit, constraints on the flavour-tagging calibration parameters are introduced. This leads to the effect that some tagged events are shifted to higher mistag probabilities. Here, they change from a tagged to an untagged state leading to discontinuities of the likelihood function. This results to fit problems, which can be avoided by setting a boundary on the mistag distributions. Every candidate with a mistag probability greater than the threshold is assigned a tag of 0 and a mistag probability of 0.5. The thresholds are determined by varying the calibration parameters within one standard deviation in the *CP* fit. This is done until no candidate has a mistag probability greater than 0.5. The resulting thresholds for the two combinations of tagging algorithms are

$$\omega_{\mathrm{OS}}^{B^+ \to J/\psi K^+} > 0.450,$$
$$\omega_{\mathrm{SS}}^{B^0 \to J/\psi K^{*0}} > 0.468.$$

The calibration plots of the the OS and the SS tagger combination for the resulting decay distributions after the cut are shown in Fig. 5.18. The corresponding calibration parameters can be found in Table 5.22 and the correlations of the calibration parameters in Table 5.23. Their calibrated performances are given in Table 5.24. The reweighted OS combination has a calibrated tagging efficiency of $\epsilon = (32.40 \pm 0.17)\%$ and a effective tagging efficiency of $\epsilon\langle D^2\rangle = (3.385 \pm 0.026 \pm 0.118)\%$. The reweighted SS combination has a calibrated tagging efficiency of $\epsilon = (57.59 \pm 0.33)\%$ and a effective tagging efficiency of $\epsilon\langle D^2\rangle = (2.219 \pm 0.025 \pm 0.256)\%$. The calibration parameters p_0 and p_1 of the OS combination show a deviation of 5.7 standard deviations and 14.3 standard deviations from a perfect calibration, where the parameters of the SS combination have deviations of 2.4 and 0.6 standard deviations.

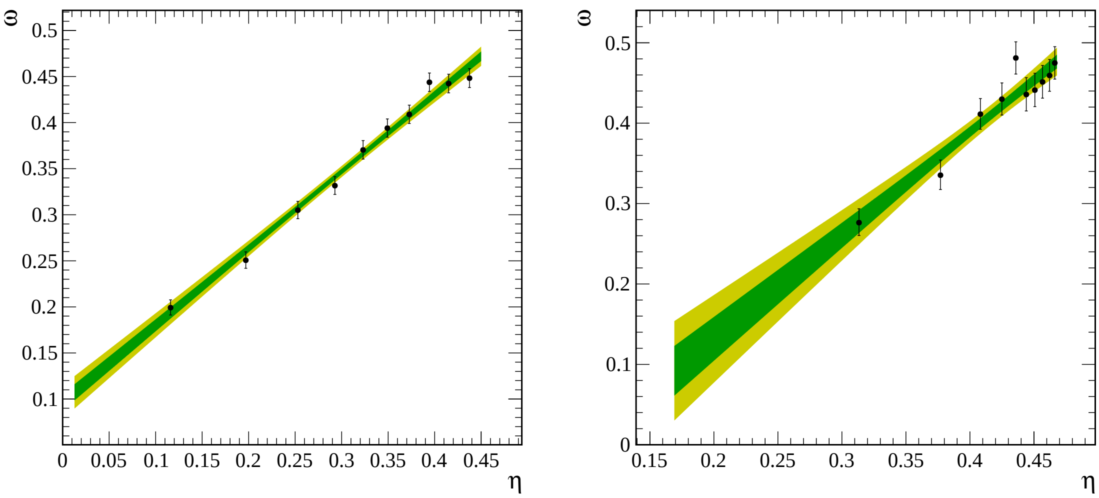

Figure 5.18: Flavour-tagging calibration for the (left) reweighted $B^+ \to J/\psi K^+$ decay for the OS combination tagger and for the (right) reweighted $B^0 \to J/\psi K^{*0}$ decay for the SS combination tagger.

Table 5.22: Flavour-tagging calibration parameters for the reweighted $B^+ \to J/\psi K^+$ decay for the OS combination and for the reweighted $B^0 \to J/\psi K^{*0}$ decay for the SS combination.

	p_0	p_1	Δp_0	Δp_1	$\langle\eta\rangle$
OS combination	0.3603 ± 0.0031	0.834 ± 0.029	0.016 ± 0.006	-0.02 ± 0.06	0.32
SS combination	0.421 ± 0.006	1.29 ± 0.12	0.003 ± 0.009	0.04 ± 0.18	0.4

Table 5.23: Correlation matrix of the flavour-tagging parameters of the (left) OS combination tagger for the reweighted $B^+ \to J/\psi K^+$ decay and of the (right) SS combination tagger for the reweighted $B^0 \to J/\psi K^{*0}$ decay.

	p_0^{OS}	p_1^{OS}	Δp_0^{OS}	Δp_1^{OS}
p_0^{OS}	1	0.14	0.010	-0.023
p_1^{OS}		1	-0.023	0.07
Δp_0^{OS}			1	0.14
Δp_1^{OS}				1

	p_0^{SS}	p_1^{SS}	Δp_0^{OS}	Δp_1^{SS}
p_0^{SS}	1	0.12	-0.028	0.019
p_1^{SS}		1	0.020	-0.08
Δp_0^{SS}			1	0.08
Δp_1^{SS}				1

Table 5.24: Flavour-tagging performances of the inclusive OS combination for the reweighted $B^+ \to J/\psi K^+$ decay, and of the inclusive SS combination tagger for the reweighted $B^0 \to J/\psi K^{*0}$ decay.

Tagger	ε	$\langle\omega\rangle$	$\varepsilon\langle D^2\rangle = \varepsilon\,(1-2\omega)^2$
$\mathrm{OS}^{B^+ \to J/\psi K^+}$	$(32.40 \pm 0.17)\%$	$(33.84 \pm 0.04 \pm 0.28)\%$	$(3.385 \pm 0.026 \pm 0.118)\%$
$\mathrm{SS}^{B^0 \to J/\psi K^{*0}}$	$(57.59 \pm 0.33)\%$	$(40.19 \pm 0.05 \pm 0.57)\%$	$(2.219 \pm 0.025 \pm 0.256)\%$

5.5 Evaluation of systematic uncertainties

For the flavour-tagging calibration parameters two sources of systematic uncertainties are taken into account. The first type is a systematic uncertainty corresponding to the method of determining the parameters on the control channels. The second type considers the transfer of the calibration parameters from a control channel to the signal channel. All absolute values of the calibration parameters are given in the convention of the EspressoPerformanceMonitor, which is calculated from the standard convention as follows $e_0 = p_0 - \langle\eta\rangle$ and $e_1 = p_1 - 1$.

5.5.1 Calibration method

To calculate possible systematic uncertainties due to the calibration method, the calibration parameters are determined with subsets of the calibration samples. The samples are split into years of data taking and magnet polarities. The absolute values of the parameters, the differences between the two values, the uncertainties on the difference, and the significance of the difference being different from zero are listed in Tables 5.25 and 5.26. With a maximum deviation of 2.1σ no significant deviation can be found, so no systematic uncertainty due to the calibration method is assigned.

Table 5.25: Test for systematic uncertainties due to the calibration method for the OS combination tagger on $B^+ \to J/\psi K^+$ and the SS combination tagger on $B^0 \to J/\psi K^{*0}$. The absolute parameter values e for the subsamples split by years, their differences Δ, and the significance Δ/σ_Δ of the difference to deviate from zero are listed.

	2011	2012	Δ	Δ/σ_Δ
e_0^{OS}	0.041 ± 0.005	0.046 ± 0.004	-0.005 ± 0.007	-0.8
e_1^{OS}	-0.15 ± 0.05	-0.176 ± 0.035	0.03 ± 0.15	0.2
Δe_0^{OS}	0.011 ± 0.011	0.019 ± 0.007	-0.007 ± 0.013	-0.6
Δe_1^{OS}	-0.056 ± 0.100	-0.009 ± 0.069	-0.047 ± 0.124	-0.4
e_0^{SS}	0.007 ± 0.011	-0.009 ± 0.008	0.015 ± 0.013	1.1
e_1^{SS}	0.25 ± 0.22	0.29 ± 0.15	-0.04 ± 0.26	-0.2
Δe_0^{SS}	0.012 ± 0.015	-0.002 ± 0.010	0.014 ± 0.019	0.7
Δe_1^{SS}	0.27 ± 0.32	-0.06 ± 0.21	0.3 ± 0.4	0.9

Table 5.26: Test for systematic uncertainties due to the calibration method for the OS combination tagger on $B^+ \to J/\psi K^+$ and the SS combination tagger on $B^0 \to J/\psi K^{*0}$. The absolute parameter values e for the subsamples split by magnet polarities, their differences Δ, and the significance Δ/σ_Δ of the difference to deviate from zero are listed.

	MagUp	MagDown	Δ	Δ/σ_Δ
e_0^{OS}	0.046 ± 0.004	0.043 ± 0.004	0.004 ± 0.006	0.6
e_1^{OS}	-0.23 ± 0.04	-0.11 ± 0.04	-0.12 ± 0.06	-2.1
Δe_0^{OS}	0.008 ± 0.009	0.023 ± 0.008	-0.015 ± 0.012	-1.2
Δe_1^{OS}	-0.01 ± 0.09	-0.03 ± 0.08	0.02 ± 0.12	0.2
e_0^{SS}	-0.005 ± 0.009	-0.003 ± 0.009	-0.002 ± 0.013	-0.2
e_1^{SS}	0.33 ± 0.19	0.26 ± 0.16	0.07 ± 0.25	0.3
Δe_0^{SS}	-0.004 ± 0.013	0.008 ± 0.012	-0.012 ± 0.017	-0.7
Δe_1^{SS}	0.07 ± 0.26	0.01 ± 0.24	0.05 ± 0.35	0.2

5.5.2 Portability from the control channels to the signal channel

The second type of possible systematic uncertainties is through the transfer of the calibration parameters from the control channels to the signal channel. The parameters are compared for samples with and without reweighting. The error on the difference is calculated as the fully correlated error, $\sigma_\Delta = \sqrt{{\sigma_1}^2 - {\sigma_2}^2}$, [73] as the comparison is performed on the same data sample. The results can be found in Table 5.27. From this, systematic uncertainties are assigned as half of the computed differences between the calibration parameters obtained with and without reweighting. The calibration parameters for the OS and SS combination tagger for the $B^0 \to J/\psi K^0_{\mathrm{S}}$ decay with their statistical and systematic uncertainties are listed in Eqs. (5.7) and (5.8). As a crosscheck it is possible to apply and calibrate the OS combination tagger on the reweighted $B^0 \to J/\psi K^{*0}$ decay and compare the results with the OS combination tagger calibrated on the reweighted $B^+ \to J/\psi K^+$ decay. Table 5.28 shows that with a maximum of the parameters' deviation of 1.5σ the reweighting method is valid.

Table 5.27: Comparison of the calibration parameters for the reweighted and not reweighted $B^+ \to J/\psi K^+$ decay for the OS combination tagger, and for the $B^0 \to J/\psi K^{*0}$ decay for the SS combination tagger. Listed are the absolute values, the difference between the two values, the uncertainty on the difference, and the significance Δ/σ_Δ.

	$B^+ \to J/\psi K^+$(rew.)	$B^+ \to J/\psi K^+$(not rew.)	Δ	Δ/σ_Δ
e_0^{OS}	0.044 ± 0.003	0.046 ± 0.003	0.0012 ± 0.0008	1.6
e_1^{OS}	-0.166 ± 0.029	-0.162 ± 0.028	0.004 ± 0.007	0.5
Δe_0^{OS}	0.016 ± 0.006	0.016 ± 0.006	-0.0007 ± 0.0015	-0.4
Δe_1^{OS}	-0.02 ± 0.06	-0.02 ± 0.06	0.008 ± 0.015	0.5
	$B^0 \to J/\psi K^{*0}$(rew.)	$B^0 \to J/\psi K^{*0}$(not rew.)	Δ	Δ/σ_Δ
e_0^{SS}	-0.004 ± 0.006	-0.002 ± 0.006	-0.0018 ± 0.0015	-1.2
e_1^{SS}	0.29 ± 0.12	0.26 ± 0.12	0.030 ± 0.019	1.6
Δe_0^{SS}	0.003 ± 0.009	0.004 ± 0.008	-0.0018 ± 0.0020	-0.9
Δe_1^{SS}	0.04 ± 0.18	0.00 ± 0.17	0.031 ± 0.029	1.1

Table 5.28: Comparison of the calibration parameters for the reweighted $B^+ \to J/\psi K^+$ and $B^0 \to J/\psi K^{*0}$ samples for the OS combination tagger. Listed are the absolute values, the difference between the two values, the uncertainty on the difference, and the significance Δ/σ_Δ.

	$B^+ \to J/\psi K^+$	$B^0 \to J/\psi K^{*0}$	Δ	Δ/σ_Δ
e_0^{OS}	0.044 ± 0.003	0.030 ± 0.009	-0.015 ± 0.009	-1.5
e_1^{OS}	-0.166 ± 0.029	-0.10 ± 0.10	0.06 ± 0.10	0.6
Δe_0^{OS}	0.016 ± 0.006	-0.001 ± 0.012	-0.017 ± 0.014	-1.3
Δe_1^{OS}	-0.02 ± 0.06	-0.02 ± 0.14	0.00 ± 0.15	0.01

The flavour-tagging parameters for the reweighted decay channels with their statistical and systematic uncertainties are as follows

$$
\begin{aligned}
p_0^{\mathrm{OS}} &= 0.3603 \pm 0.0031\,(\mathrm{stat}) \pm 0.0006\,(\mathrm{syst})\ , \\
p_1^{\mathrm{OS}} &= 0.834 \pm 0.029\,(\mathrm{stat}) \pm 0.002\,(\mathrm{syst})\ , \\
\langle \eta^{\mathrm{OS}} \rangle &= 0.316\ , \\
\Delta p_0^{\mathrm{OS}} &= 0.016 \pm 0.006\,(\mathrm{stat}) \pm 0.0004\,(\mathrm{syst})\ , \\
\Delta p_1^{\mathrm{OS}} &= -0.02 \pm 0.06\,(\mathrm{stat}) \pm 0.004\,(\mathrm{syst})\ ,
\end{aligned}
\tag{5.7}
$$

$$
\begin{aligned}
p_0^{\mathrm{SS}} &= 0.421 \pm 0.006\,(\mathrm{stat}) \pm 0.0009\,(\mathrm{syst})\ , \\
p_1^{\mathrm{SS}} &= 1.29 \pm 0.12\,(\mathrm{stat}) \pm 0.015\,(\mathrm{syst})\ , \\
\langle \eta^{\mathrm{SS}} \rangle &= 0.4\ , \\
\Delta p_0^{\mathrm{SS}} &= 0.003 \pm 0.009\,(\mathrm{stat}) \pm 0.0009\,(\mathrm{syst})\ , \\
\Delta p_1^{\mathrm{SS}} &= 0.04 \pm 0.18\,(\mathrm{stat}) \pm 0.016\,(\mathrm{syst}).
\end{aligned}
\tag{5.8}
$$

5.6 Performance on the signal channel

The effective tagging efficiency for the two tagging algorithms, OS and SS, on the signal decay channel is listed in Table 5.29. The effective tagging efficiency for the combination of OS and SS divided into subsets of OS exclusively tagged events, SS exclusively tagged events and events that are tagged by both algorithms, called overlap, is shown in Table 5.30.

Table 5.29: Effective tagging efficiency of the two different tagging algorithms and the combination on the complete data sample for the $B^0 \to J/\psi K^0_S$ decay.

Algorithm	$\varepsilon_{\text{eff}}^{B^0 \to J/\psi K^0_S}$ [%]
OS	3.60
SS	2.40
OS + SS	5.93

Table 5.30: Effective flavour-tagging efficiency of the combination (OS + SS) divided into OS exclusively tagged events, SS exclusively tagged events and events that are tagged by both algorithms (Overlap).

Category	$\varepsilon_{\text{eff}}^{B^0 \to J/\psi K^0_S}$ [%]
OS excl.	0.77
SS excl.	1.33
Overlap	3.83
Total	5.93

Table 5.31: Effective tagging efficiency of the two different tagging algorithms and the combination on the complete data sample for the $B^0 \to \psi(2S) K^0_S$ decay.

Algorithm	$\varepsilon_{\text{eff}}^{B^0 \to \psi(2S) K^0_S}$ [%]
OS	2.46
SS	1.07
OS + SS	3.42

The effective tagging efficiency in the $B^0 \to J/\psi K^0_S$ is 3.60 % for the OS combination tagger and 2.40 % for the SS combination taggers. The effective tagging efficiencies for the $B^0 \to \psi(2S) K^0_S$ decay, where the $\psi(2S)$ candidate is reconstructed from two muons, are shown in Table 5.31. here, it can be seen that the effective tagging efficiency of the OS combination tagger with 2.46 % and the SS combination tagger with 1.07 % is lower than for the electron mode. The higher performance of the OS combination tagger in the electron mode can be explained by the enhanced fraction of events for which the rest of the event is sufficient to generate a positive trigger decision, called triggered independent of signal (TIS). Triggered on signal (TOS) classifies events for which the signal part of the event alone is sufficient to generate a positive trigger decision [74]. Here, the global decision of the L0 trigger is taken into account. For the muon mode no candidates are selected that are exclusively categorized as TIS. For the electron mode the fraction of TIS events is 25.12 %. As can be seen in Table A.2 the tagging efficiency ϵ is higher and the mistag fraction ω is lower for the exclusive TIS category of the electron data sample compared to the exclusive TOS events. The resulting effective tagging efficiency for the TIS events is $5.219 \pm 0.070 \pm 0.301\%$ and for the TOS events $1.777 \pm 0.023 \pm 0.118\%$. The lower performances of the SS combination taggers can not be explained by the different populations in TIS/TOS categories, as shown in Table A.3, where these large deviations of the tagging efficiencies can not be observed. Here, the deviation is caused by different distributions of the transverse momentum, p_{T}, of the B candidate. The effective tagging efficiency of the two decays in bins of the transverse momentum is shown in Figs. A.3 and A.4. The corresponding transverse momentum distributions of the two decay modes can be seen in Fig. A.5. After a reweighting of the distribution for the electron mode to match the p_{T} distribution of the muon mode, a subsequent determination of the flavour-tagging performances results in a decrease of the effective tagging efficiency of the electron mode to $\epsilon = 1.3\,\%$. The reweighted distribution to match the muon mode can be found in Fig. A.6.

5.7 Results of the time-dependent *CP*-violation measurement

Finally the results of the flavour tagging are applied in the time-dependent *CP*-violation measurement [1]. The following section presents the results of this measurement. With an unbinned weighted maximum likelihood fit to the decay-time distributions of the signal decays the *CP* observables S and C are determined. The probability density function describes the mesons' decay times, the flavour-tagging decisions $\vec{d'} = (d'_{\mathrm{OS}}, d'_{\mathrm{SS}})$, the decay-time uncertainties σ_t and predicted mistag probabilities. The reconstructed decay-time distributions with the corresponding fit for the $B^0 \to J/\psi K^0_{\mathrm{S}}$ and $B^0 \to \psi(2\mathrm{S})K^0_{\mathrm{S}}$ decays are shown in Fig. 5.19 [1].

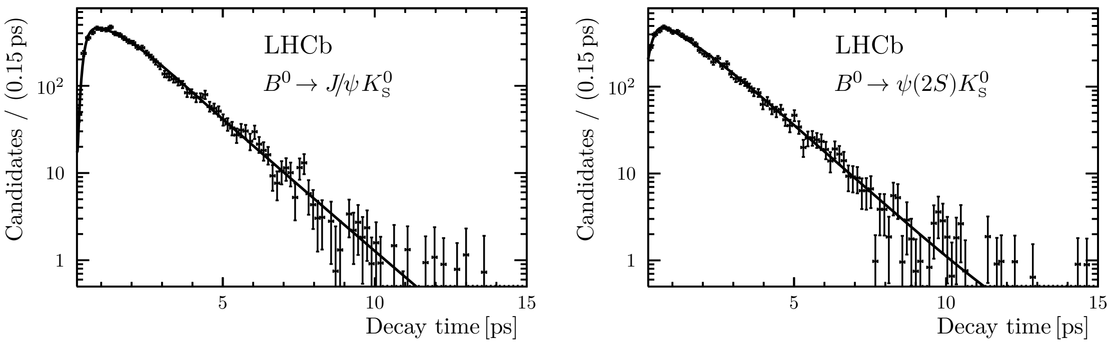

Figure 5.19: Projections of the decay-time fit to weighted (left) $B^0 \to J/\psi K^0_{\mathrm{S}}$ and (right) $B^0 \to \psi(2S)K^0_{\mathrm{S}}$ candidates [1].

With $10\,630 \pm 140$ $B^0 \to J/\psi K^0_{\mathrm{S}}$ decay candidates and $7\,970 \pm 100$ $B^0 \to \psi(2S)K^0_{\mathrm{S}}$ decay candidates the resulting *CP*-violation observables with its statistical and systematic uncertainties are

$$
\begin{aligned}
C(B^0 \to J/\psi K^0_S) &= 0.12 \pm 0.07\ (\text{stat}) \pm 0.02\ (\text{syst})\,, \\
S(B^0 \to J/\psi K^0_S) &= 0.83 \pm 0.08\ (\text{stat}) \pm 0.01\ (\text{syst})\,, \\
C(B^0 \to \psi(2S) K^0_S) &= -0.05 \pm 0.10\ (\text{stat}) \pm 0.01\ (\text{syst})\,, \\
S(B^0 \to \psi(2S) K^0_S) &= 0.84 \pm 0.84\ (\text{stat}) \pm 0.01\ (\text{syst})\,,
\end{aligned}
$$

The signal yield asymmetries $(N_{\overline{B}^0} - N_{B^0})/(N_{\overline{B}^0} + N_{B^0})$ as a function of decay time are shown in Fig. 5.20 [1]. The symbol N_{B^0} ($N_{\overline{B}^0}$) is the number of decays with a B^0 ($\overline{B}^0$) flavour tag. The solid curves are the projections of the PDF with the combined flavour-tagging decision

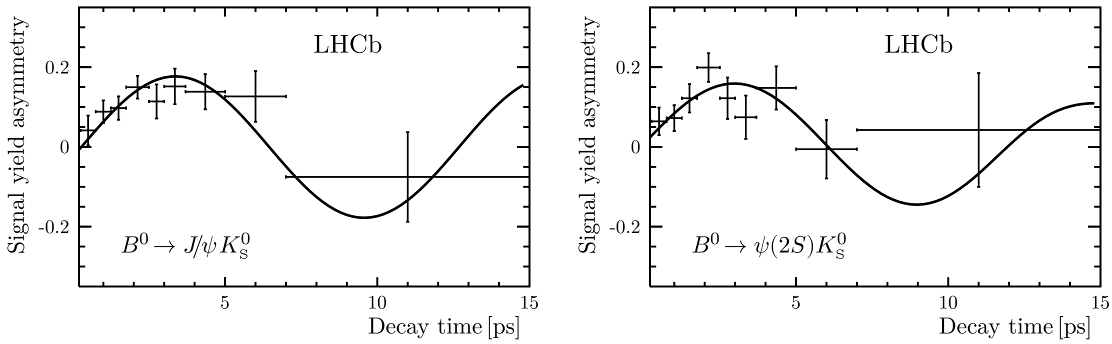

Figure 5.20: Signal yield asymmetries $(N_{\overline{B}^0} - N_{B^0})/(N_{\overline{B}^0} + N_{B^0})$ versus the decay time for (left) $B^0 \to J/\psi K^0_S$ and (right) $B^0 \to \psi(2S) K^0_S$ decays. The symbol N_{B^0} ($N_{\overline{B}^0}$) is the number of decays with a B^0 ($\overline{B}^0$) flavour tag. The solid curves are the projections of the PDF with the combined flavour-tagging decision[1].

The resulting updated LHCb average of the *CP*-violation observables using the results from all $B^0 \to c\bar{c}K^0_S$ modes, *i.e.* $B^0 \to J/\psi(\mu^+\mu^-)K^0_S$, $B^0 \to J/\psi K^0_S$, and $B^0 \to \psi(2S)K^0_S$, is

$$
\begin{aligned}
C(B^0 \to c\bar{c}K^0_S) &= -0.017 \pm 0.029\,, \\
S(B^0 \to c\bar{c}K^0_S) &= 0.760 \pm 0.034\,.
\end{aligned}
$$

These results improve the precision of $\sin 2\beta$ at LHCb by 20 %, and are expected to improve the precision of the world average [1] accordingly.

6 Particle identification at the LHCb experiment

One of the main experimental challenges of the measurements of the ratios R_K and R_{K^*}, as described in Sec. 2.2 and in general in flavour physics, is the reduction of combinatorial background and the distinction between otherwise topological identical final states with for example pions, kaons, protons, electrons and muons [75]. Furthermore, the particle identification is a major part of the flavour tagging as described in Chapter 4. The PID system of the LHCb experiment is described in Sec. 3.2.2.

6.1 Particle-identification variables

The muon, RICH, and calorimeter systems provide PID information, which can be combined to more powerful PID variables. The first approach to combine PID information is a linear multiplication of the log-likelihood of each subsystem. This results in a combined log-likelihood $\mathcal{L}$ with

$$\mathcal{L} = \mathcal{L}_{\text{RICH}} \cdot \mathcal{L}_{\text{CALO}} \cdot \mathcal{L}_{\text{MUON}} \,. \tag{6.1}$$

The combined differential log-likelilhood (DLL) is defined as the log-likelihood difference between the particle and pion hypotheses [76]. For kaon tracks (K) the variable

$$\text{DLL}_{K\pi}$$

is defined as

$$\text{DLL}_{K\pi} = \ln \mathcal{L}(K) - \ln \mathcal{L}(\pi) \,. \tag{6.2}$$

The second approach is a more complex combination of information from the PID subsystems. Here, the PID variables are calcualated with multivariate techniques, whereby information from the tracking system and correlations between the detector systems are considered. The training of the multivariate classifier is performed with simulated B meson events. There are different artificial neural networks for electrons, muons, pions, kaons, protons, and misidentified tracks. The output variable ProbNN(K, π, p, μ, e) is a normalized probability distribution of values between 0 and 1. Depending on the training and data sample, different versions (tunings) of the variables are available. For data recorded in the years 2011 and 2012 the ProbNN version `MC12TuneV2` and `MC12TuneV3`is used. The version `MC12TuneV3` results in a better performance for leptons and `MC12TuneV2` for hadrons [2]. For the years 2015 and 2016 the ProbNN version `MC15TuneV1` is chosen. Whether DLL or ProbNN variables are employed depends on the particular analysis. In the most cases the discrimination power is enhanced by using a combination of ProbNN and DLL variables.

6.2 Particle-identification calibration

In general, information from the PID system is used to reject background and select signal candidates. The number of signal candidates N_{raw} has to be efficiency corrected to compute the true number of event candidates N_{true} with

$$N_{\mathrm{true}} = \epsilon \cdot N_{\mathrm{raw}} \, , \tag{6.3}$$

with the efficiency ϵ. A typical way to calculate efficiencies in particle physics is through the usage of simulated samples. The agreement between data and simulation is not optimal for PID variables, because the simulation has to take account for the precise detector response including the occupancy of the detectors and experimental conditions, like the temperature and gas pressures. In the case of PID, a different method is employed. Here, calibration samples from recorded data are used to determine the efficiency ϵ_{PID}.

6.2.1 Selection of the calibration samples

The PID calibration samples are recorded from decays, which allow for an unambiguous identification of daughter particles without using PID information. The calibration samples are pure samples of the five most common charged, long-lived particle species produced in the LHCb detector (kaons, pions, protons, electron, and muons). Low-multiplicity decay modes with large branching fractions and high purities are chosen. The decays are listed in Table 6.1. The calibration samples are used to measure the efficiency and background rejection of applied PID requirements [76]. Details about the selection requirements of the calibration samples can be found in Ref. [75].

Table 6.1: Overview of decay modes that are selected as calibration samples. Soft (hard) means low (high) momentum, p, and transversal momentum, p_{T}, respectively. [75]

Species	Soft	Hard
$e^{\pm}$	-	$J/\psi \to e^+e^-$
$\mu^{\pm}$	$D_s^+ \to \mu^+\mu^-\pi^+$	$J/\psi \to \mu^+\mu^-$
$\pi^{\pm}$	$K_{\mathrm{S}}^0 \to \pi^+\pi^-$	$D^{*+} \to D^0\pi^+$, $D^0 \to K^-\pi^+$
$K^{\pm}$	$D_s^+ \to K^+K^-\pi^+$	$D^{*+} \to D^0\pi^+$, $D^0 \to K^-\pi^+$
$p^{\pm}$	$\Lambda \to p\pi^-$	$\Lambda \to p\pi^-$, $\Lambda_c^+ \to pK^-\pi^+$

In the years 2011 and 2012 the calibration samples were selected with specific stripping lines. Although this resulted in samples with a large number of events, some kinematic regions were not covered sufficiently. Thus, in the years 2015 and 2016 of data taking, particular trigger lines in the HLT2, called *TurboCalib* [76] lines, were developed to select the PID calibration samples. They store the complete calibration samples, so the whole event information is available offline.

6.2.2 PIDCalib package

The PIDCalib package [77] is an LHCb software package to measure the efficiency of PID requirements and give simple access to the calibration samples. The following description of the PIDCalib methods mainly follows Ref. [77], unless otherwise stated. The package implements a data-driven technique to estimate the efficiency of PID requirements in physics analysis. As the response of the PID variables is non-uniform and depends on different observables, the data-driven calibration is performed in bins of the parametrizing observables. In the PID calibration it is assumed that the response of the PID variables is fully parametrized by a set of variables, such as the momentum p, the transverse momentum p_{T}, the number of tracks, nTracks, or the number of hits in the SPD, nSPDHits. With sufficiently fine partitions of the sample no significant variation of the PDF of the PID variable in each subset is observed. It follows that the efficiency of a given selection requirement is constant within a subset. This allows for a deduction of efficiencies of any given track, even if the track does not originate from a calibration sample. The efficiency is taken from the calibration sample's subset that corresponds to the values of the parametrizing variables of the given track. The efficiency ϵ_i of the subset i is defined as $\epsilon_i = \frac{N_i'}{N_i}$, with N_i as the number of events before and N_i' as the number of events after the PID requirement. The average efficiency over the whole space of the parametrizing variables follows as

$$\bar{\epsilon} = \frac{\sum_i \epsilon_i N_i}{\sum_i N_i} \,. \tag{6.4}$$

To determine the PID efficiency for a reference sample, that is not a calibration sample, the parametrizing variables in the calibration sample can be weighted to match the variables of the reference sample. So, the PID efficiency is computed with per-subset weights, which are calculated as the normalized ratio of reference to calibration tracks, with

$$w_i = \frac{R_i}{C_i} \cdot \frac{C}{R} \,, \tag{6.5}$$

where R_i (C_i) is the number of reference (calibration) tracks in the subset i, and R (C) as the total number of reference (calibration) tracks in the sample. The average efficiency on the weighted calibration sample is

$$\bar{\epsilon} = \frac{\sum_i \epsilon_i w_i C_i}{\sum_i w_i C_i} \,. \tag{6.6}$$

With a substitution of the weights in Eq. (6.6) with Eq. (6.5) the average efficiency of the PID requirement on the reference sample is

$$\overline{\epsilon} = \frac{\sum_i R_i \epsilon_i}{\sum_i R_i} = \frac{1}{R} \sum_i R_i \epsilon_i \,. \tag{6.7}$$

For PID requirements on multiple tracks the average efficiency $\epsilon_{\text{ensemble}}$ for an ensemble of tracks with the single efficiencies ϵ_i is defined as

$$\epsilon_{\text{ensemble}} = \prod_i \epsilon_i \,. \tag{6.8}$$

7 Particle-identification calibration

In the selection process of the recent R_{K^*} analysis [2] background contamination is reduced by using PID information. As a multivariate classifier and the determination of the PID efficiencies is based on simulated samples, these samples have to be corrected. Therefore, a data-driven calibration is performed as described in Sec. 6.2. In the study, the PIDCalib package is used to determine a per-event efficiency, w_{PID} to reweight the simulated samples recorded by the LHCb experiment in the years 2011 and 2012. After a reproduction of these studies on the PID efficiency, the PID calibration samples are validated for the years 2015 and 2016.

7.1 Selection

The efficiency determination for the samples are performed using the PID cuts given in [2], which are listed in Table 7.1. To maximize the rejection power, the probabilities of identification and misidentification information of the particles are combined. For data taken in the years 2011 and 2012 the ProbNN variables are used with tune MC12TuneV2 for hadrons and tune MC12TuneV3 for electrons, as it performs better for leptons. For the years 2015 and 2016 the ProbNN variables are used in tune MC15TuneV1 for all tracks. Distributions of the PID variables, that are employed in the analysis are shown in Figs. A.7 to A.22. To match the selection requirements of the data samples, all candidates are required to have a registered track in the RICH subsystem. Moreover, the muons (electrons) are required to have a track in the muon (calorimeter) system. To be consistent with the kinematic boundaries of the PID calibration samples, additional cuts on the transverse momentum, p_{T}, are applied.

Table 7.1: Summary PID requirements for the particles e, μ, K, and π.

Particle	Requirement
all	hasRich
μ	hasMuon
e	hasCalo
K, π	$p_{\mathrm{T}} > 250\,\mathrm{MeV}/c$
μ	$p_{\mathrm{T}} > 800\,\mathrm{MeV}/c$
e	$p_{\mathrm{T}} > 500\,\mathrm{MeV}/c$
K	ProbNNk $\cdot$ (1 − ProbNNp) > 0.05
π	ProbNNpi $\cdot$ (1 − ProbNNk) $\cdot$ (1 − ProbNNp) > 0.1
μ	ProbNNmu > 0.2
e	ProbNNe > 0.2

7.2 Efficiency calculation

During the PID calibration efficiency maps are calculated with the PIDCalib package and the simulated samples are reweighted using these maps. Therefore, the efficiencies for the given requirements are determined in partitions of the parametrizing variables of PID response. In this case only the dependency on the particle momentum and the pseudorapidity is considered as no significant dependence on variables that describe the event multiplicity, like the number of tracks in the detector, nTracks, and the number of hits in the SPD, nSPDHits, is observed, as can be seen in Figs. A.23 to A.26.

The choice of the binning scheme is important to calculate the efficiency maps and shows a large impact on the systematic uncertainties of the PID calibration [2]. The partitions for each of the parametrizing variables are chosen indepently under two conditions. First, the bins have to be chosen as small as possible, such that the PID efficiency in one partition shows no significant variation. Secondly, the partitions have to be large enough to achieve small uncertainties on the single efficiencies and to avoid unphysical values through the use of *sWeights*. Here, an algorithm to automatically determine the binning schemes has been implemented following the approach of Ref. [2]. For the each of the parametrizing variables the phase space is initially divided into iso-populated bins. Then, adjacent bins are merged iteratively as long as the difference of the efficiencies of the two bins is smaller than 5σ, where σ denotes the standard deviation. The resulting binning schemes for the track types e, μ, K, and π are shown in Figs. 7.1 to 7.4. Here, the resulting efficiencies are in blue and the parametrizing variable from the calibration data set in black. For the years 2011 and 2012 the efficiencies and binning schemes are compatible with the results of Ref. [2]. Thus, the implementation of the binning scheme algorithm could be validated. The determination of the binning schemes for the years 2015 and 2016 shows good agreement with the results of 2011 and 2012 for the pion and kaon tracks. In the case of the muon tracks a lower efficiency is determined over the whole range of the distributions. This is observed for both, 2015 and 2016 and calls for further studies. As can be seen in Fig. 7.1, the efficiencies of 2011 and 2012 and the efficiencies of 2016 are qualitatively compatible. For the data recorded in 2015 the PID efficiency significantly deviates from these results. As can bee seen in Figs. A.10, A.14, A.18 and A.22, this behaviour could originate from a deviation in the distribution of the ProbNNe variable in 2015. Further studies on these deviations are required but not performed in this study.

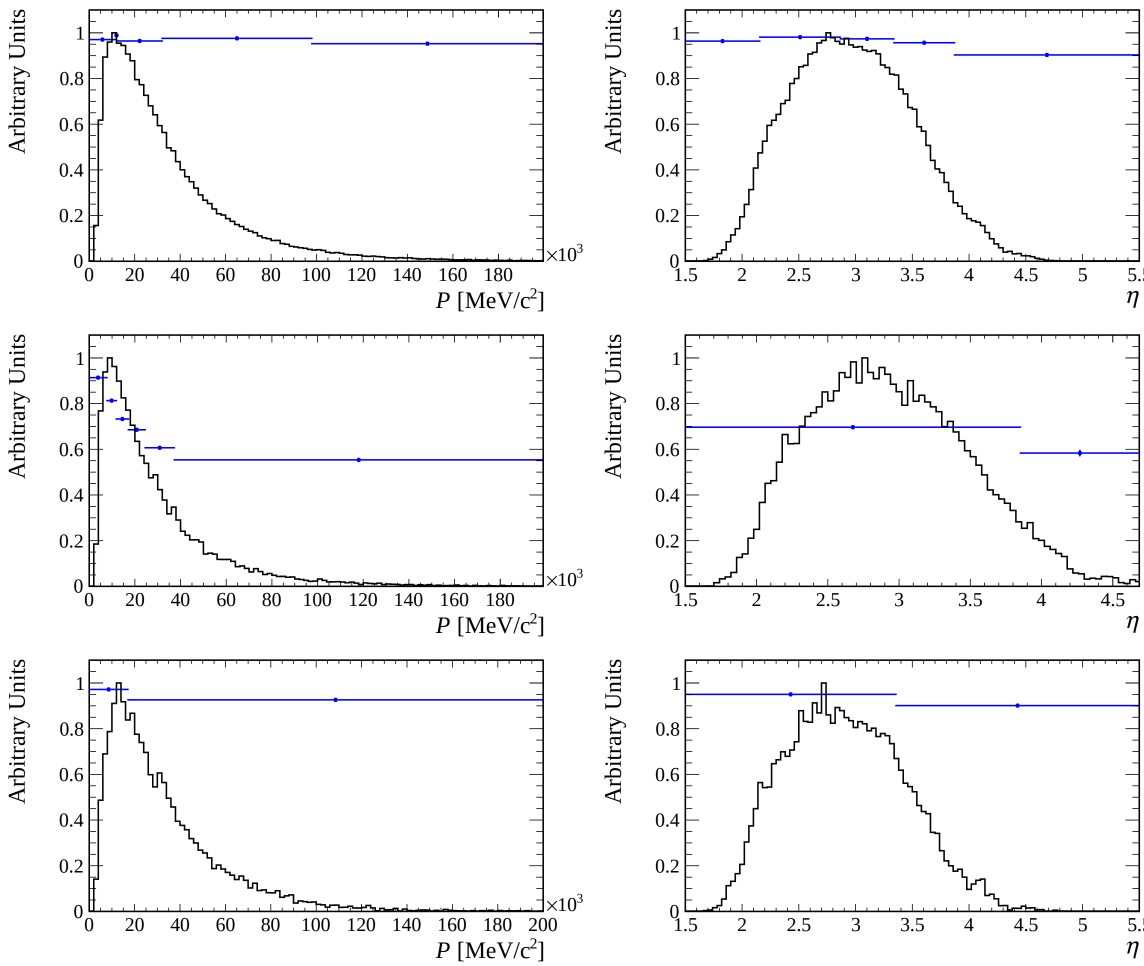

Figure 7.1: PID efficiency for electron tracks (blue) as a function of the particle (left) momentum, P, and the (right) pseudorapidity, η (black). From top to bottom 2011 and 2012, 2015, and 2016.

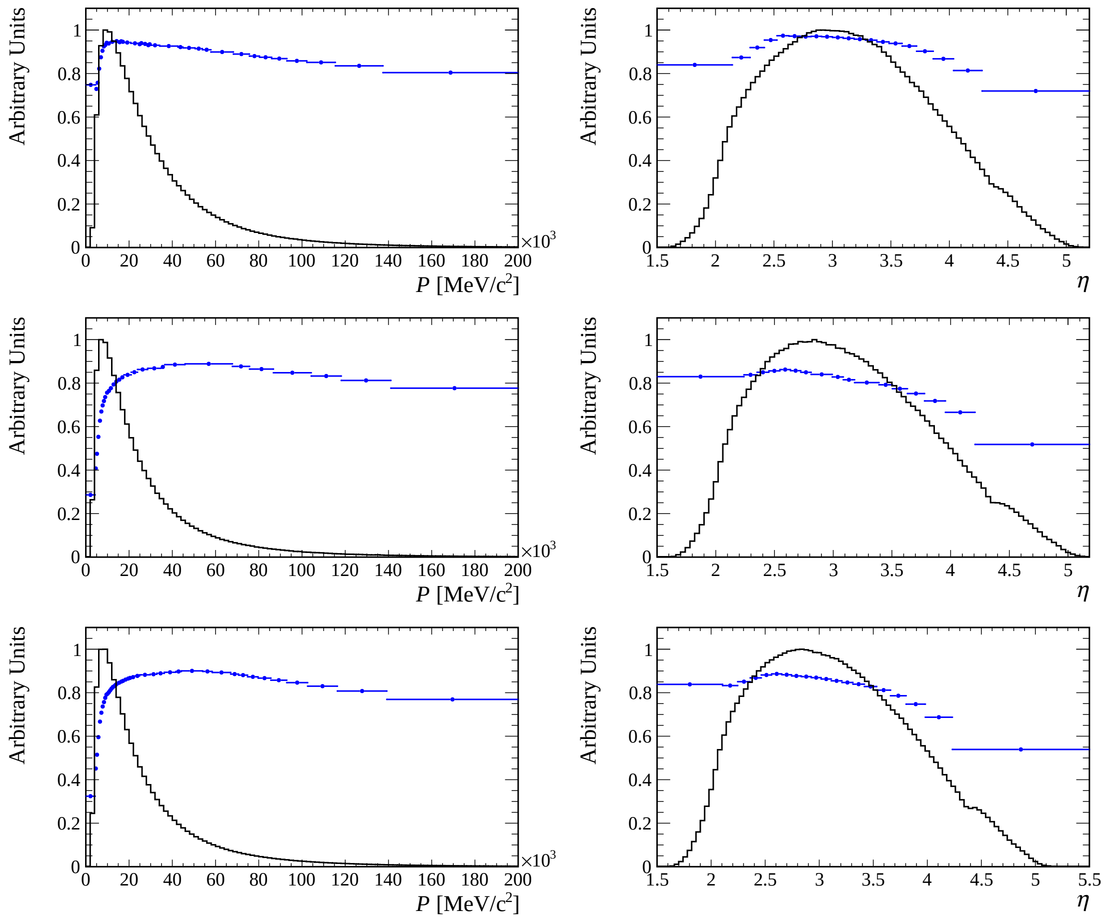

Figure 7.2: PID efficiency for muon tracks (blue) as a function of the particle (left) momentum, P, and the (right) pseudorapidity, η (black). From top to bottom 2011 and 2012, 2015, and 2016.

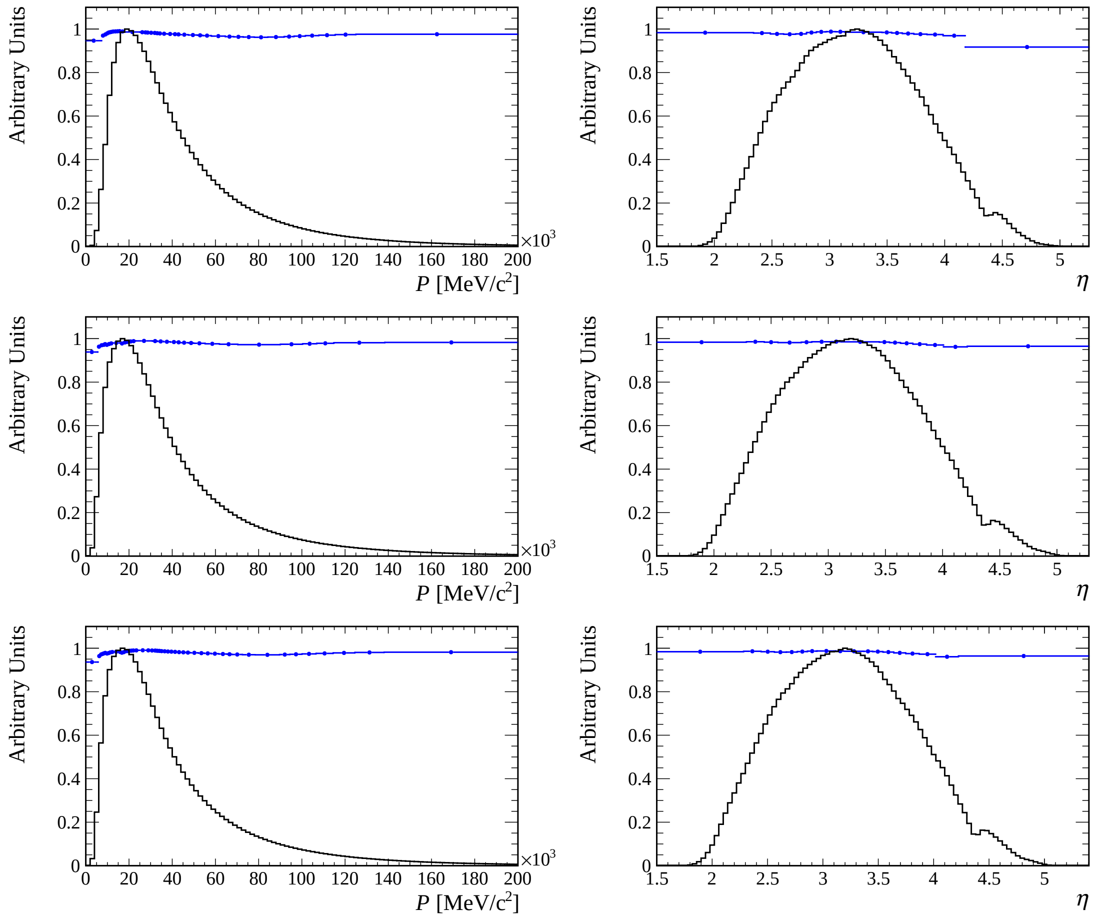

Figure 7.3: PID efficiency for kaon tracks (blue) as a function of the particle (left) momentum, P, and the (right) pseudorapidity, η (black). From top to bottom 2011 and 2012, 2015, and 2016.

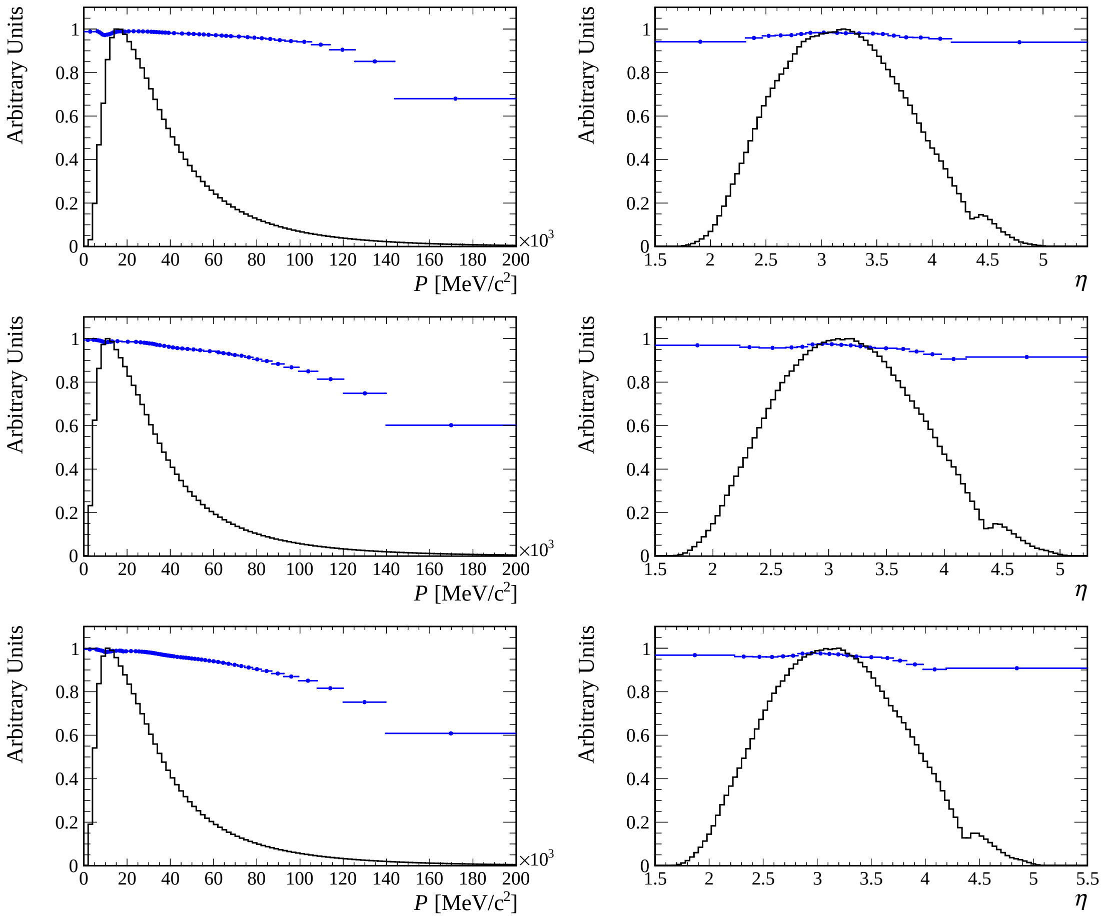

Figure 7.4: PID efficiency for pion tracks (blue) as a function of the particle (left) momentum, P, and the (right) pseudorapidity, η (black). From top to bottom 2011 and 2012, 2015, and 2016.

8 Outlook and conclusion

Many studies by the LHCb experiment focus on decays with muons in the final state, exploiting the experiment's muon reconstruction system. However, the inclusion of electron modes allows for an extension of the LHCb physics programme. This thesis provides first studies of the flavour-tagging calibration with electrons in general and first studies of the particle-identification (PID) calibration with electron samples recorded in the years 2015 and 2016.

The *CP*-violation observables C and S are measured in the study of decay-time-dependent *CP* violation in the $B^0 \to J/\psi K^0_S$ and $B^0 \to \psi(2S) K^0_S$ decays, where the J/ψ candidate is reconstructed from two electrons and the $\psi(2S)$ candidate from two muons. The analysis uses data recorded by the LHCb experiment at centre-of-mass energies of 7 and 8 TeV corresponding to an integrated luminosity of $3\,\mathrm{fb}^{-1}$ and was recently brought to publication [1]. This thesis provides the underlying flavour-tagging calibration for the $B^0 \to J/\psi K^0_S$ decay, which uses $B^+ \to J/\psi K^+$ and $B^0 \to J/\psi K^{*0}$ decays, where the J/ψ candidates are reconstructed from two electrons. It is the first systematic flavour-tagging study with electron modes included at LHCb. The calibration of the OS combination tagger with the $B^+ \to J/\psi K^+$ decay results in an effective tagging efficiency of

$$\varepsilon^{\mathrm{OS}}_{B^+ \to J/\psi K^+} = 3.385 \pm 0.026 \pm 0.118\%\,, \tag{8.1}$$

and the calibration of the SS combination tagger with the $B^0 \to J/\psi K^{*0}$ decay results in an effective tagging efficiency of

$$\varepsilon^{\mathrm{SS}}_{B^0 \to J/\psi K^{*0}} = 2.219 \pm 0.025 \pm 0.256\%\,. \tag{8.2}$$

A comparison with the results of the $B^0 \to \psi(2S) K^0_S$ decay with two muons shows an enhanced flavour-tagging performance in the electron mode. Moreover, the measurement, that uses these flavour-tagging parameters improves the precision of $\sin 2\beta$ at LHCb by 20 %. The precision could be enhanced further by taking into account the data recorded in 2015 and 2016. Here, an update of the flavour-tagging calibration is needed.

The second part of this thesis provides first systematic studies with PID calibration samples recorded in the years 2015 und 2016. Measurements of LFU ratios rely on the distinction of otherwise topological identical final states. Therefore, the validation of the PID calibration samples is an essential factor in the search of physics beyond the Standard Model. Samples recorded in the years 2011 and 2012 show results, which are consistent to previous studies. The new calibration samples show an agreement with the previous calibration results, except for the electron samples recorded in 2015 and a deviation in the efficiency of the muon samples. Here, further studies are needed to understand the observed effects.

A Appendix

A.1 Additional material of the flavour-tagging analysis

A.1.1 BDT input variables

Table A.1: BDT input variables.

$B^+ \to J/\psi K^+$
χ^2 of the B^+ vertex
p_T of the B^+
p_T of the electrons
p_T of the J/ψ
IP of the B^+
min(log(χ^2 (IP)) of the electrons
max(log(χ^2 (IP)) of the electrons
χ^2 of the second-best minimum IP of the B^+
χ^2 (IP) of the B^+
χ^2 (IP) of the electrons
$\chi^2(\mathrm{IP_{min}})$ of the K^+
$B^0 \to J/\psi K^{*0}$
min(log(χ^2 (IP)) of the electrons
max(log(χ^2 (IP)) of the electrons
χ^2_vertex of the B^0
p_T of the B^0
χ^2 (IP) of the B^0
χ^2 (IP) of the electrons
$\chi^2(\mathrm{IP_{min}})$ of the π
$\mathrm{IP_{min}}$ of the J/ψ

A.1.2 BDT responses for k-folding iterations

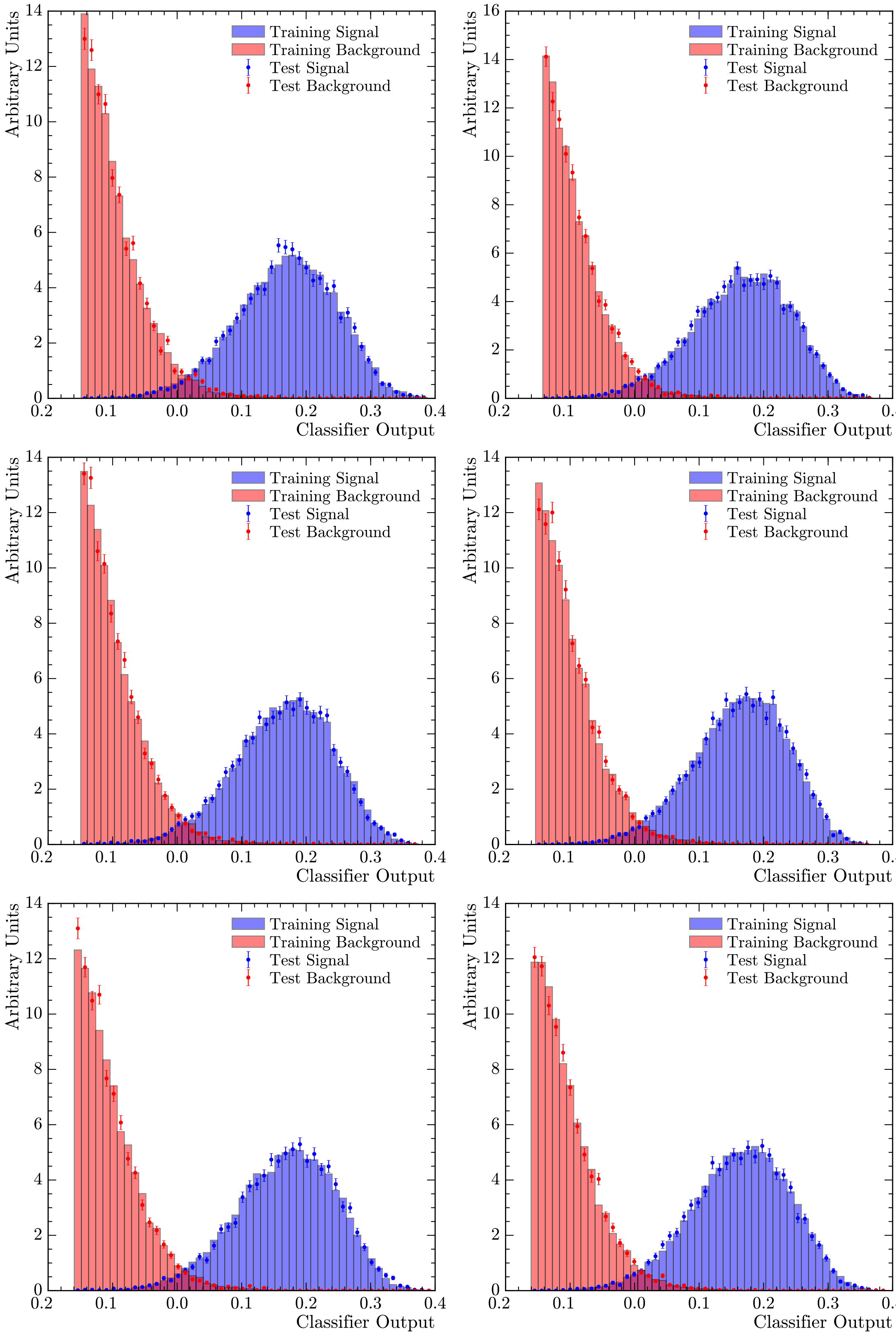

Figure A.1: BDT classifier output distributions for all six folds for $B^+ \to J/\psi(\to e^+e^-)K^+$.

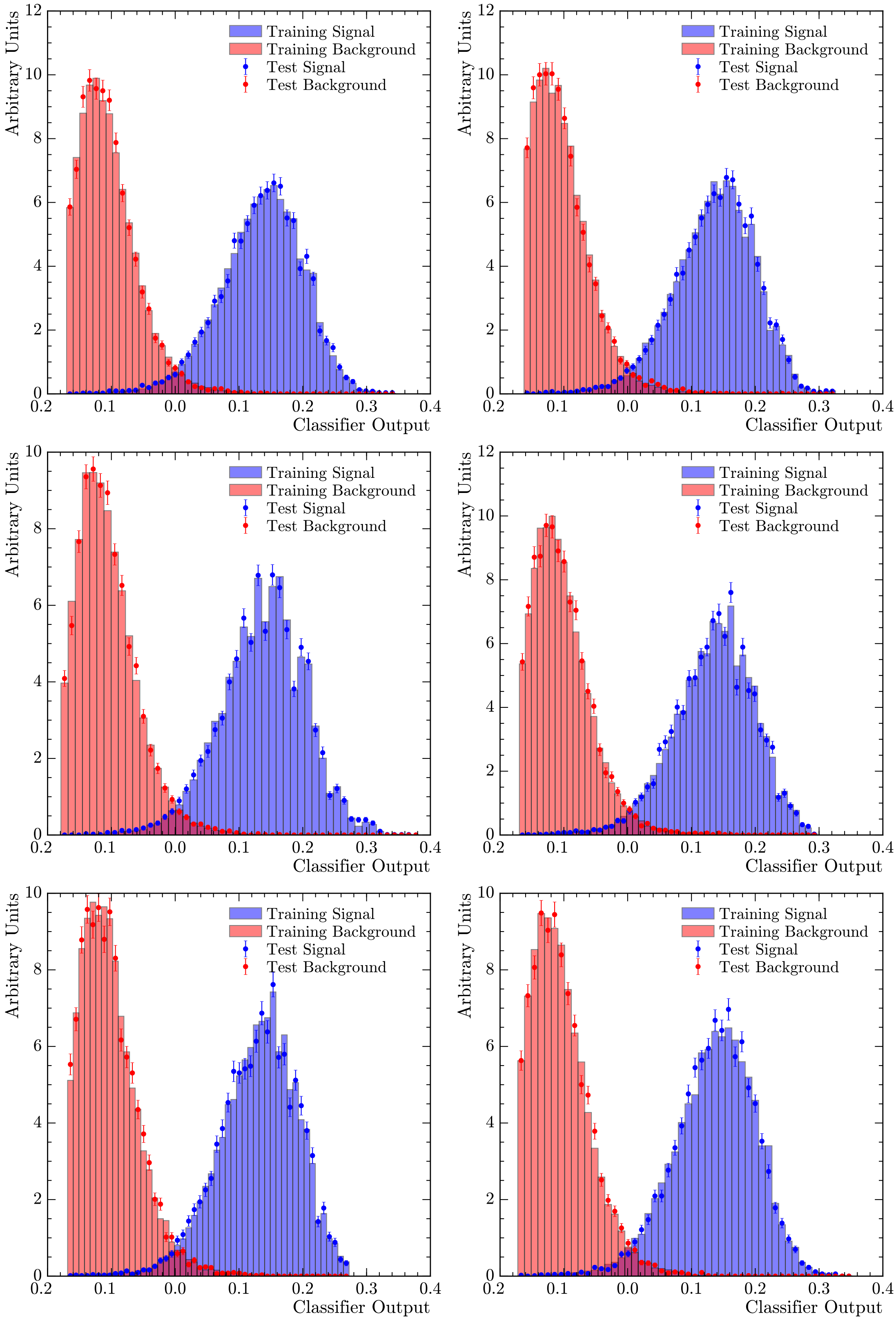

Figure A.2: BDT classifier output distributions for all six folds for $B^0 \to J/\psi(\to e^+e^-)K^{*0}$.

A.1.3 Flavour-tagging performances in categories of TIS and TOS

Table A.2: Flavour-tagging performances of the OS combination tagger for the $B^0 \to J/\psi\, K^0_\mathrm{s}$ decay in exclusive categories of TIS and TOS.

Trigger	ϵ	ω	$\epsilon\langle D^2\rangle = \epsilon\,(1-2\omega)^2$
TIS && !TOS	$(44.425 \pm 0.376)\%$	$(32.862 \pm 0.089 \pm 0.494)\%$	$(5.219 \pm 0.070 \pm 0.301)\%$
TOS && !TIS	$(28.949 \pm 0.221)\%$	$(37.612 \pm 0.063 \pm 0.411)\%$	$(1.777 \pm 0.023 \pm 0.118)\%$
TIS && TOS	$(46.657 \pm 0.350)\%$	$(33.349 \pm 0.082 \pm 0.443)\%$	$(5.174 \pm 0.064 \pm 0.276)\%$

Table A.3: Flavour-tagging performances of the SS combination tagger for the $B^0 \to J/\psi\, K^0_\mathrm{s}$ decay in exclusive categories of TIS and TOS.

Trigger	ϵ	ω	$\epsilon\langle D^2\rangle = \epsilon\,(1-2\omega)^2$
TIS && !TOS	$(73.085 \pm 0.633)\%$	$(43.162 \pm 0.085 \pm 1.164)\%$	$(1.367 \pm 0.036 \pm 0.466)\%$
TOS && !TIS	$(74.293 \pm 0.393)\%$	$(41.068 \pm 0.065 \pm 0.702)\%$	$(2.371 \pm 0.037 \pm 0.373)\%$
TIS && TOS	$(75.899 \pm 0.527)\%$	$(40.461 \pm 0.091 \pm 0.959)\%$	$(2.762 \pm 0.056 \pm 0.556)\%$

A.1.4 Effective tagging efficiency in bin of $B^0 p_\mathrm{T}$

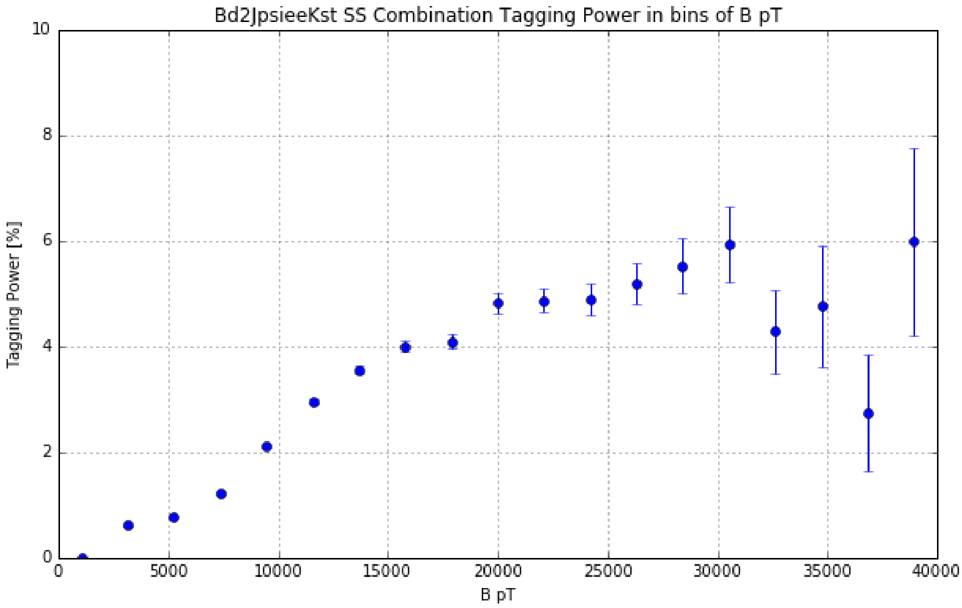

Figure A.3: Effective tagging efficiency (tagging power) in bins of the transverse momentum, p_{T}, for the $B^0 \to J/\psi\, K^0_{\mathrm{S}}$ decay.

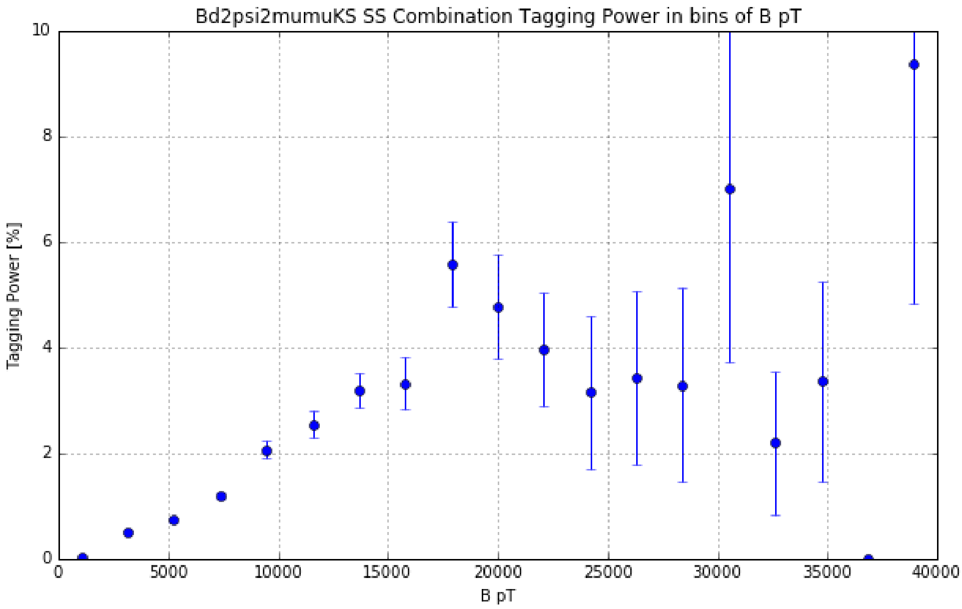

Figure A.4: Effective tagging efficiency (tagging power) in bins of the transverse momentum, p_{T}, for $B^0 \to \psi(2S)K^0_{\mathrm{S}}$ decay, where the $\psi(2S)$ is reconstructed from two muons.

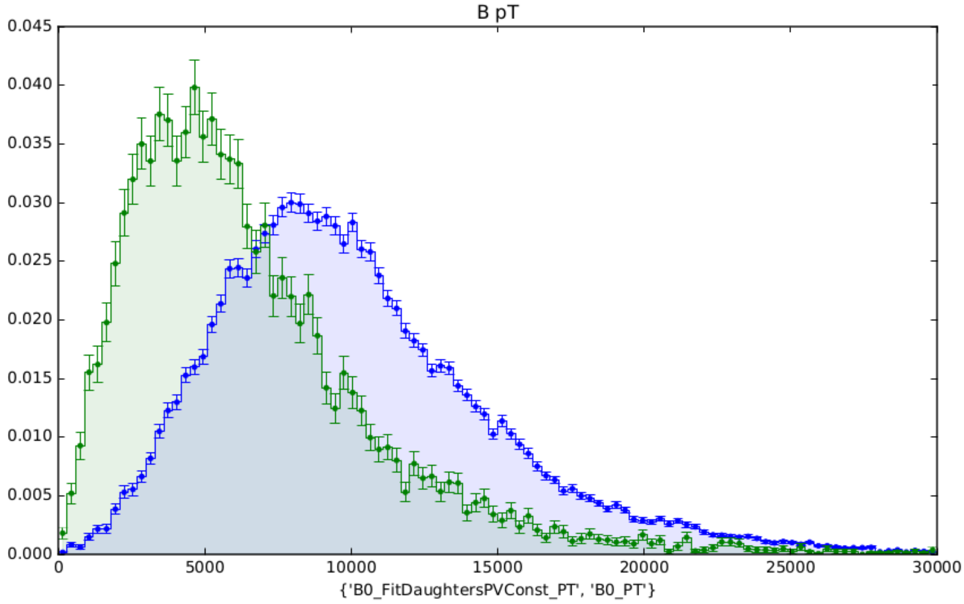

Figure A.5: Distributions of transverse momentum, p_{T}, for the (blue)$B^0 \to J/\psi\, K^0_{\mathrm{s}}$ decay and (red) $B^0 \to \psi(2S) K^0_{\mathrm{s}}$ decay.

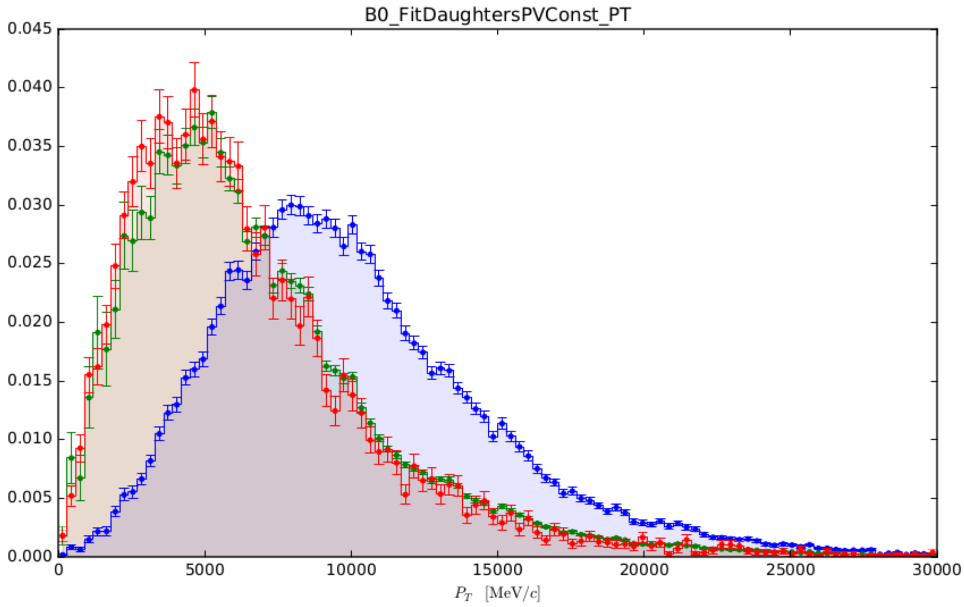

Figure A.6: Distributions of transverse momentum, p_{T}, for the (blue) $B^0 \to J/\psi\, K^0_{\mathrm{S}}$ decay and the (red) $B^0 \to \psi(2S) K^0_{\mathrm{S}}$ decay and the (green) reweighted $B^0 \to J/\psi\, K^0_{\mathrm{S}}$ decay.

A.2 Additional material of the PID-calibration studies

A.2.1 Particle identification distributions

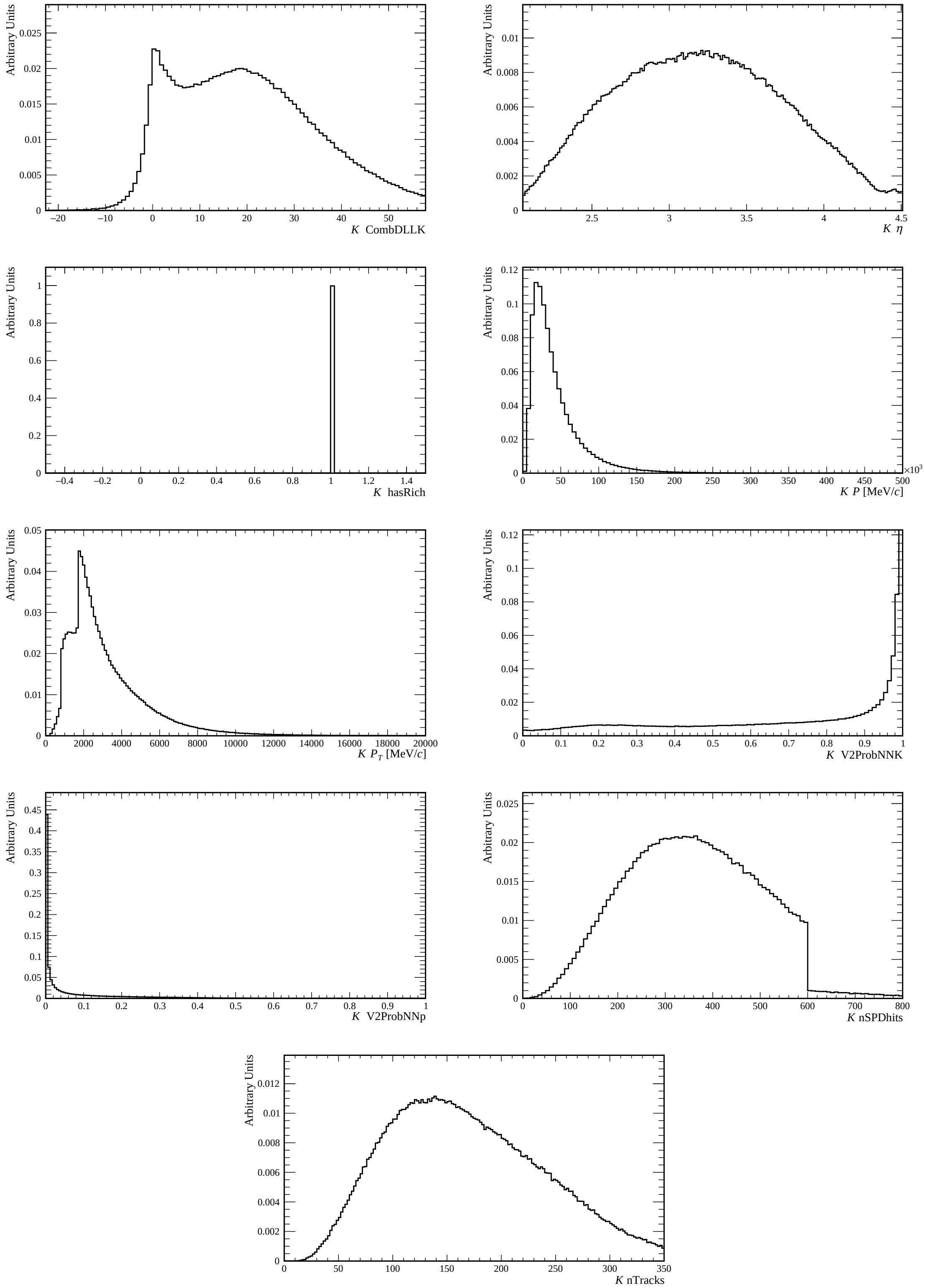

Figure A.7: PID variables used for the selection of kaon candidates in 2011.

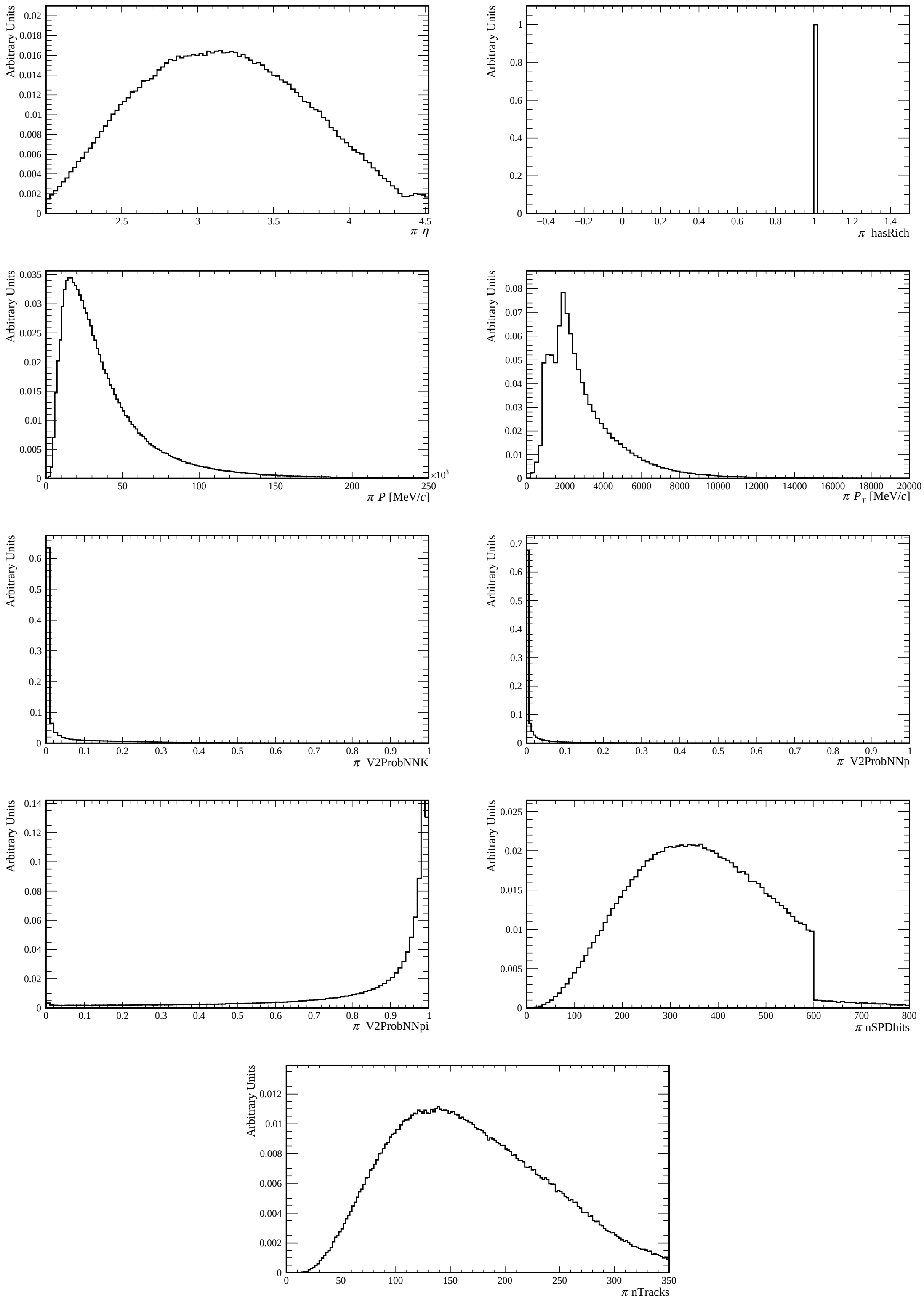

Figure A.8: PID variables used for the selection of pion candidates in 2011.

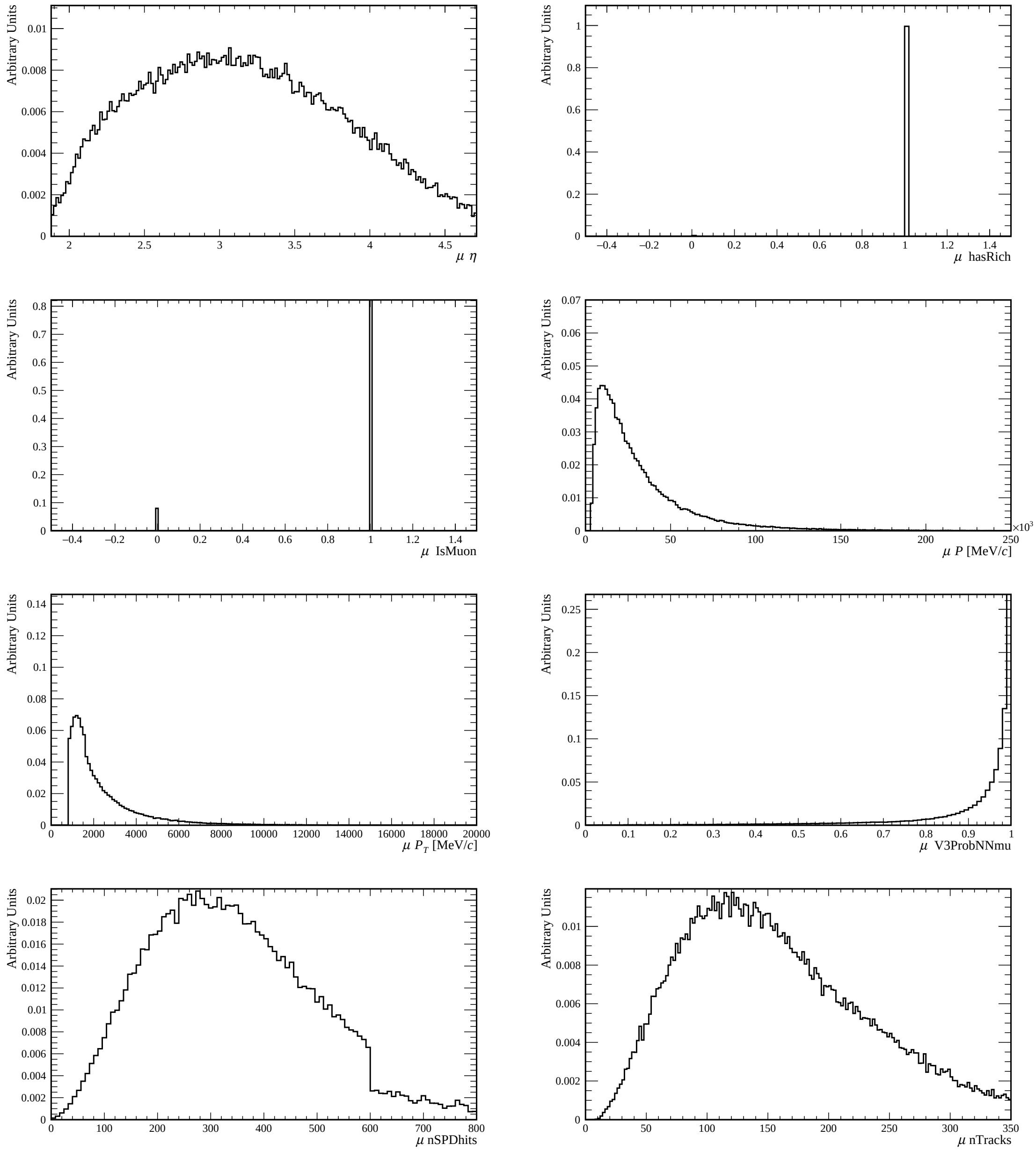

Figure A.9: PID variables used for the selection of muon candidates in 2011.

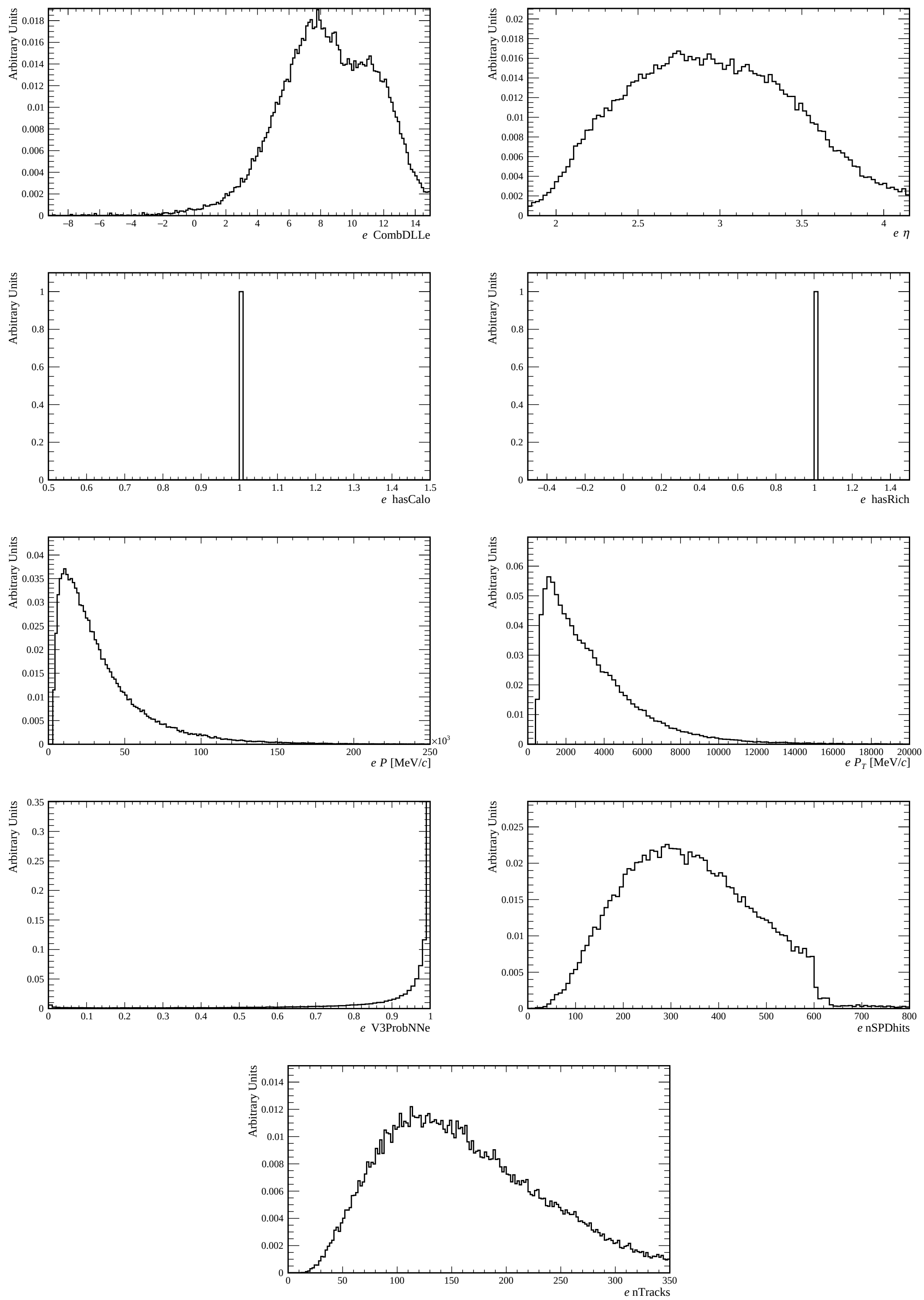

Figure A.10: PID variables used for the selection of electron candidates in 2011.

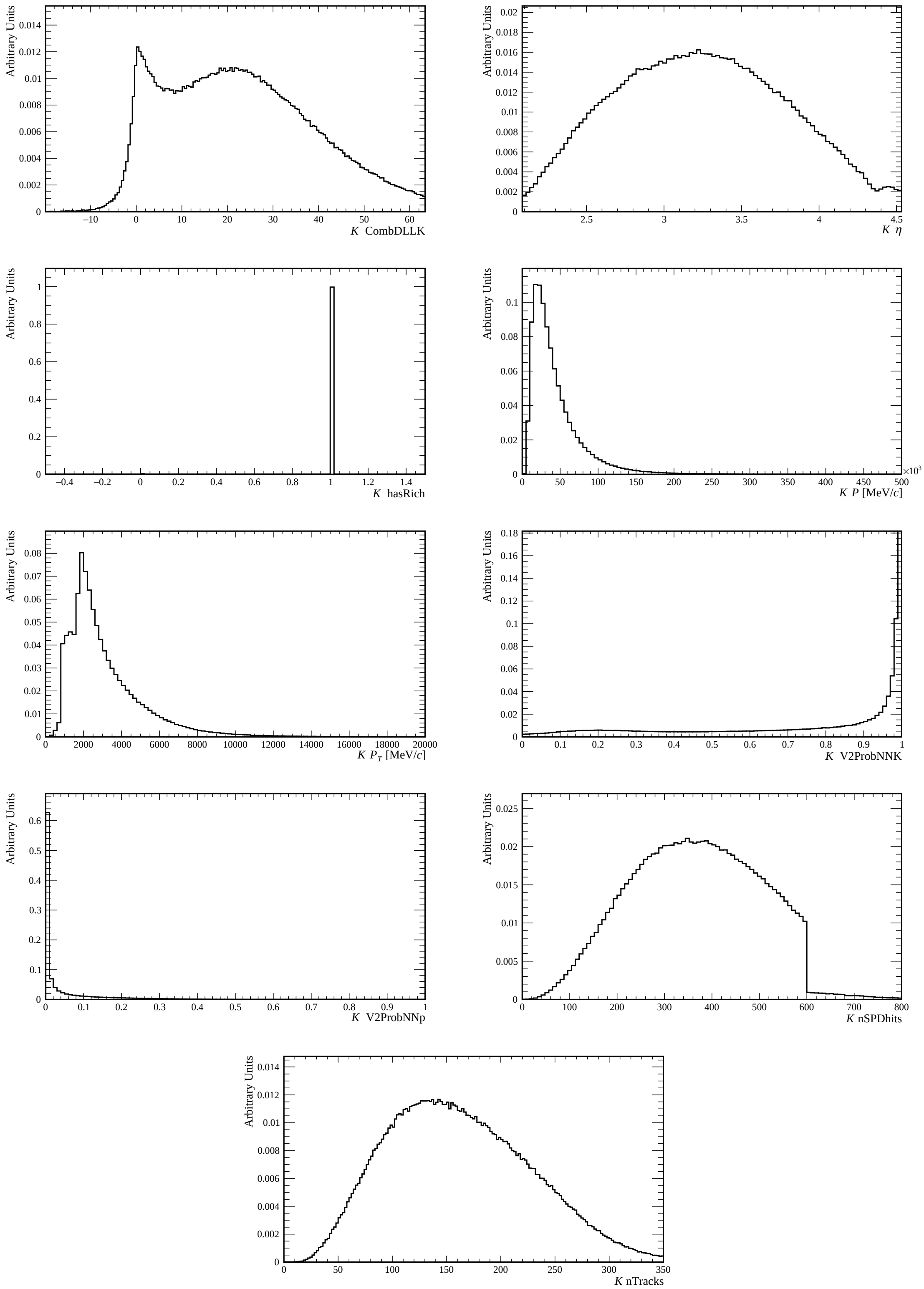

Figure A.11: PID variables used for the selection of kaon candidates in 2012.

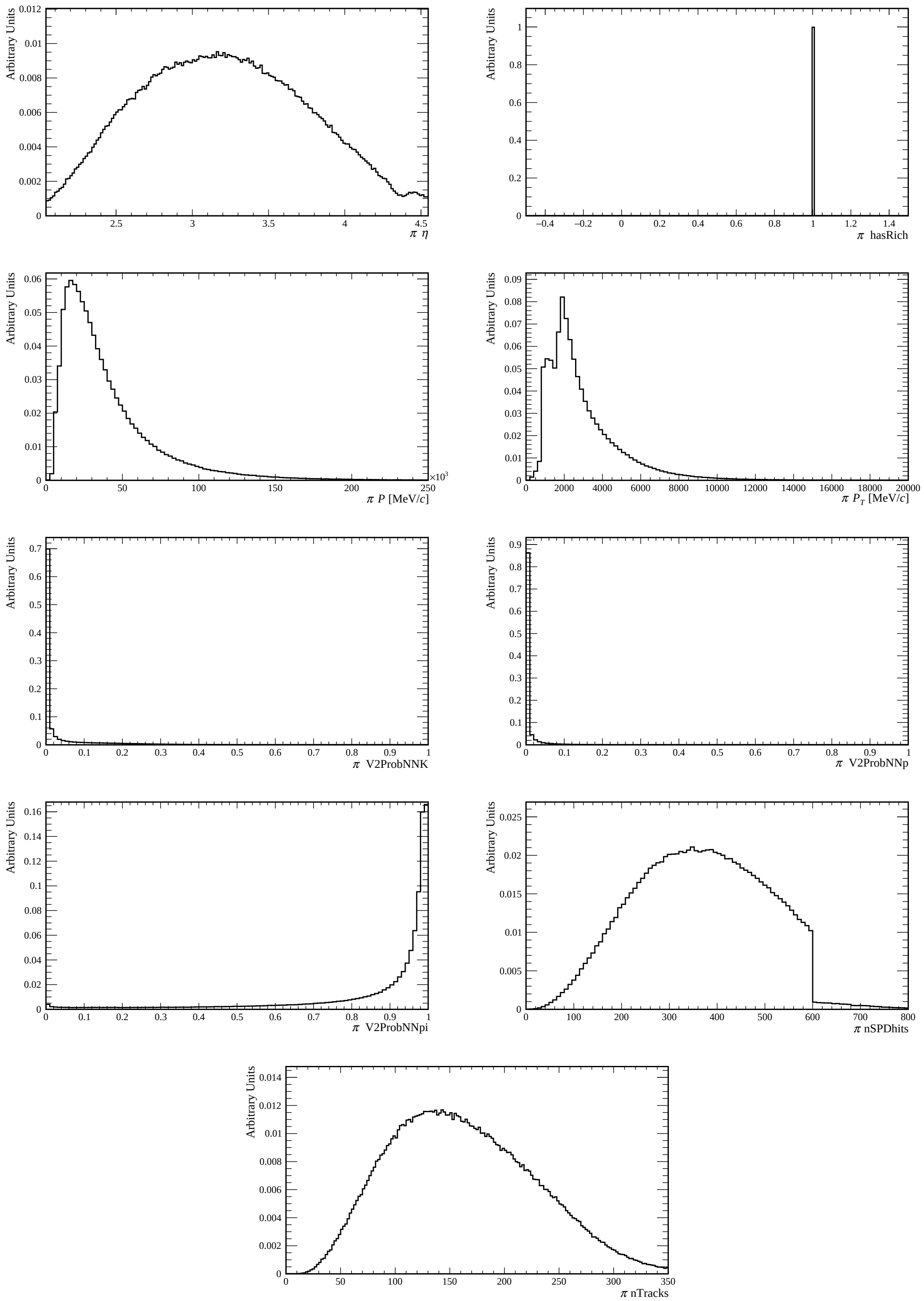

Figure A.12: PID variables used for the selection of pion candidates in 2012.

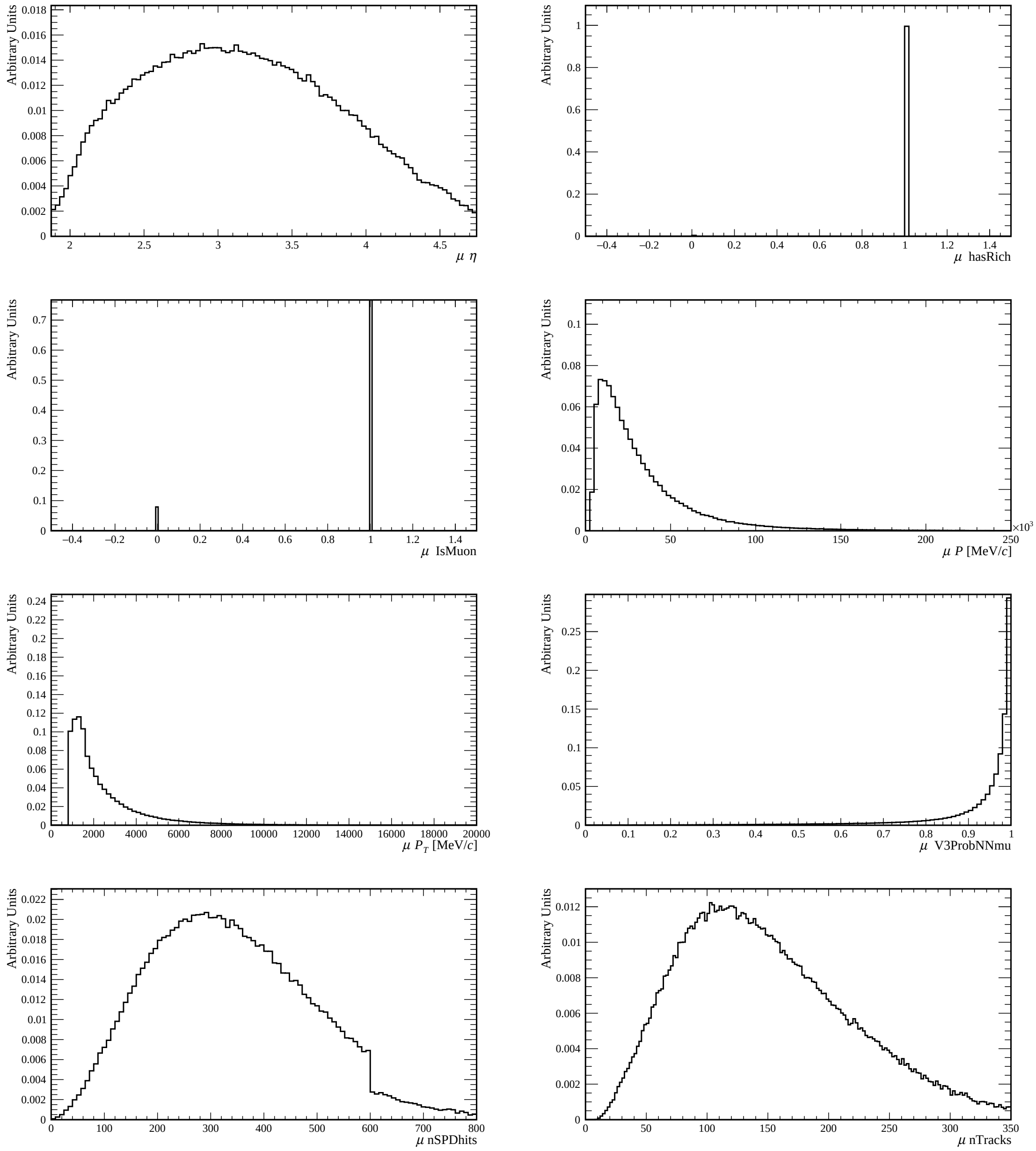

Figure A.13: PID variables used for the selection of muon candidates in 2012.

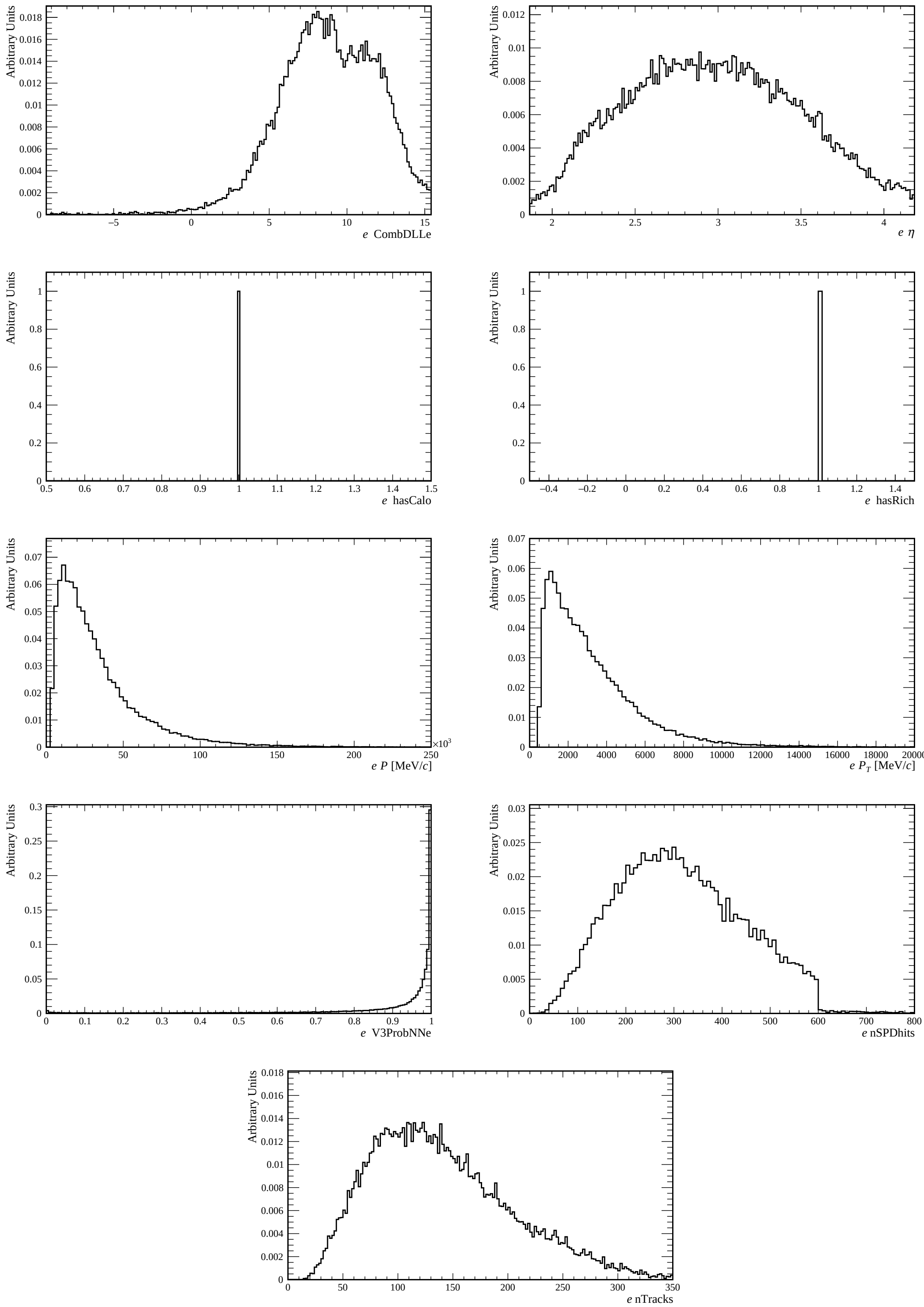

Figure A.14: PID variables used for the selection of electron candidates in 2012.

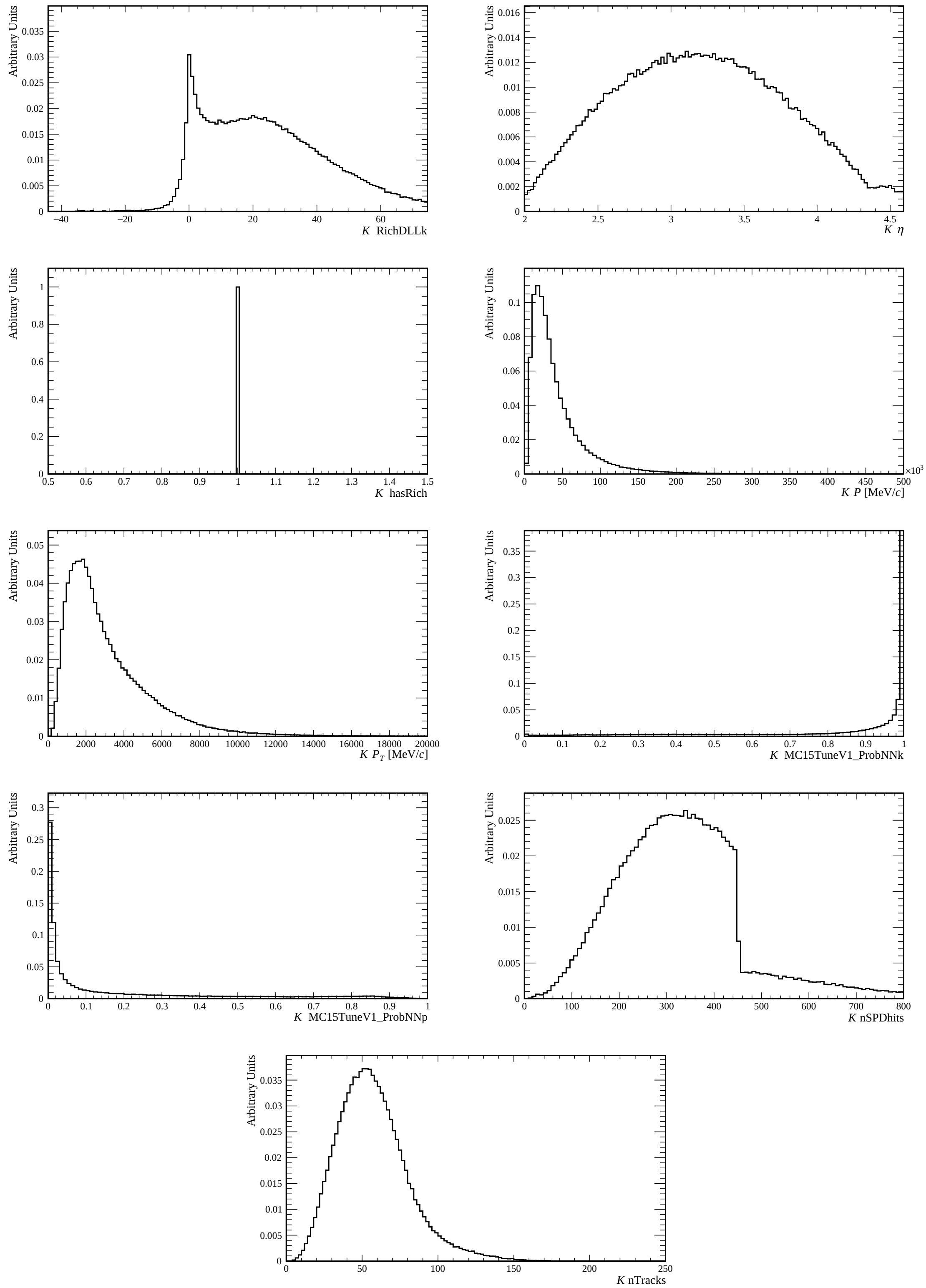

Figure A.15: PID variables used for the selection of kaon candidates in 2015.

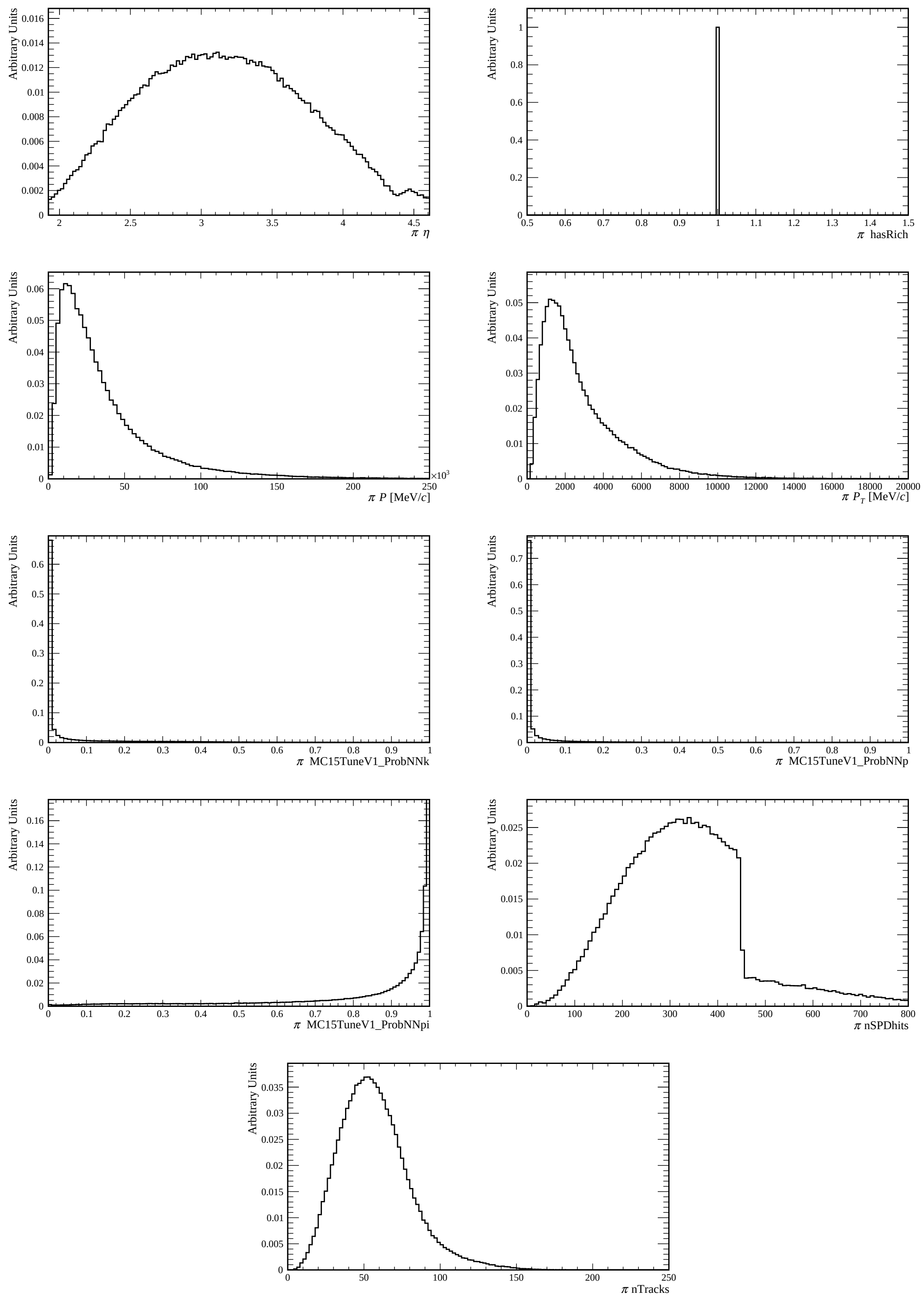

Figure A.16: PID variables used for the selection of pion candidates in 2015.

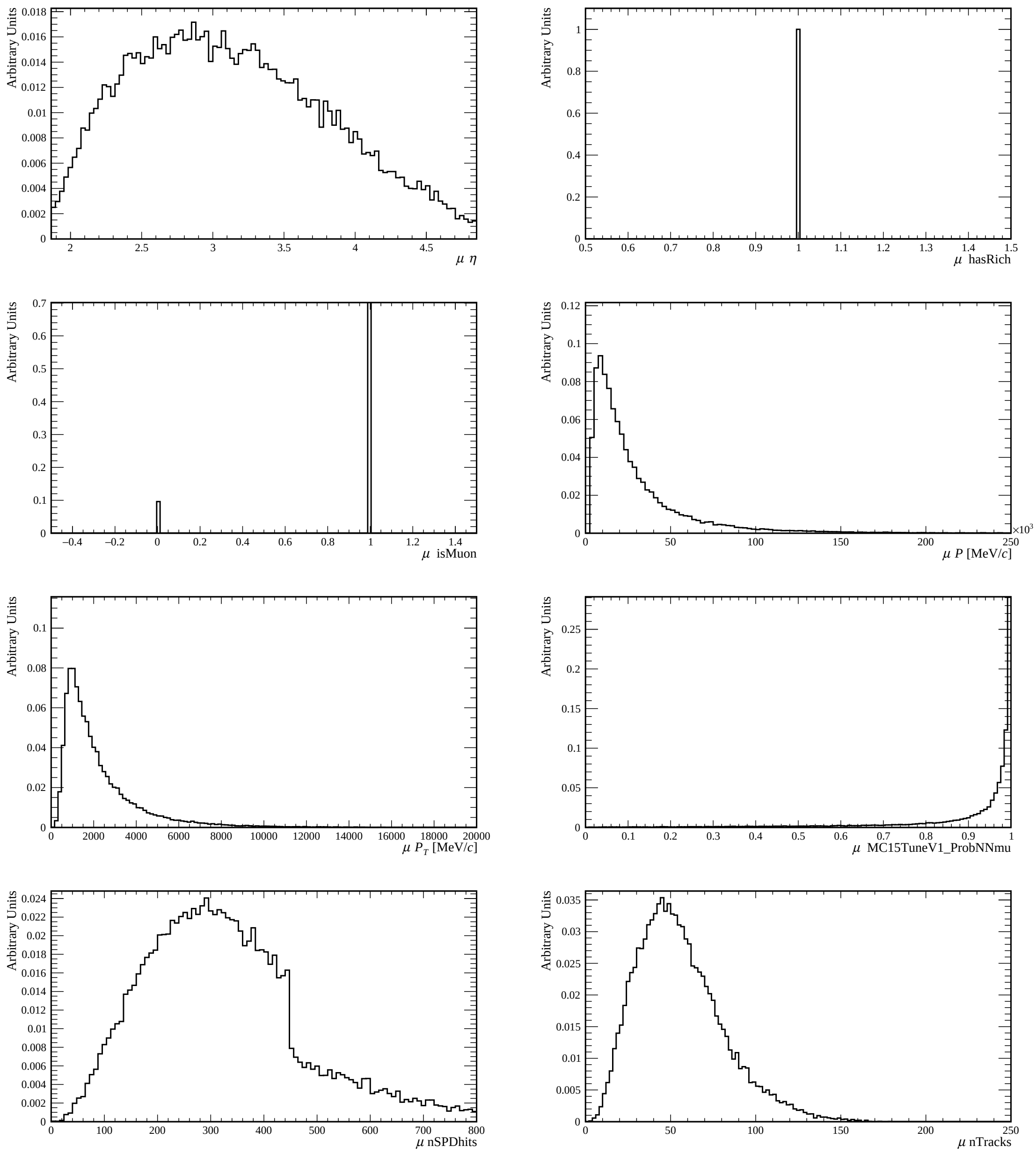

Figure A.17: PID variables used for the selection of muon candidates in 2015.

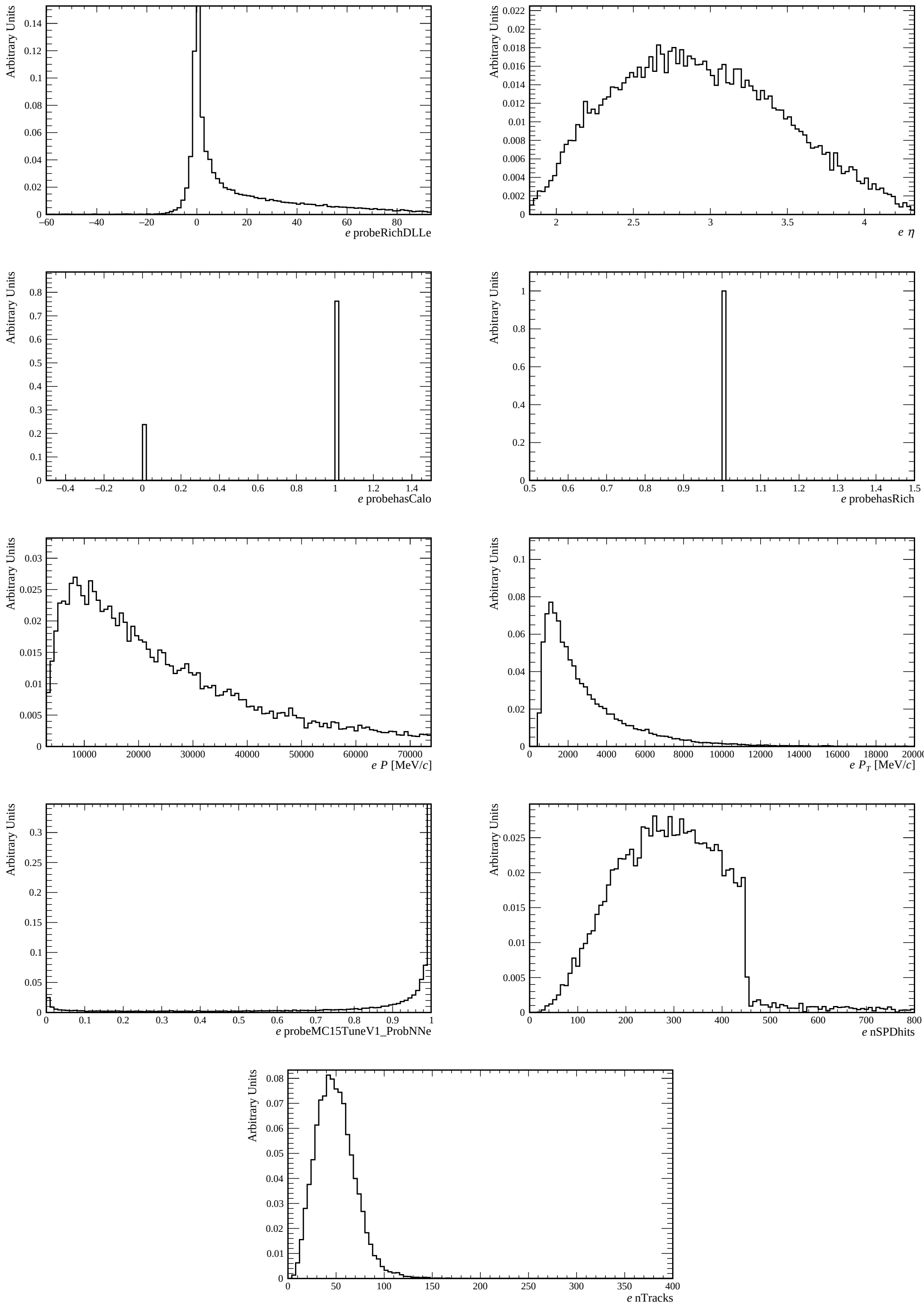

Figure A.18: PID variables used for the selection of electrons candidates in 2015.

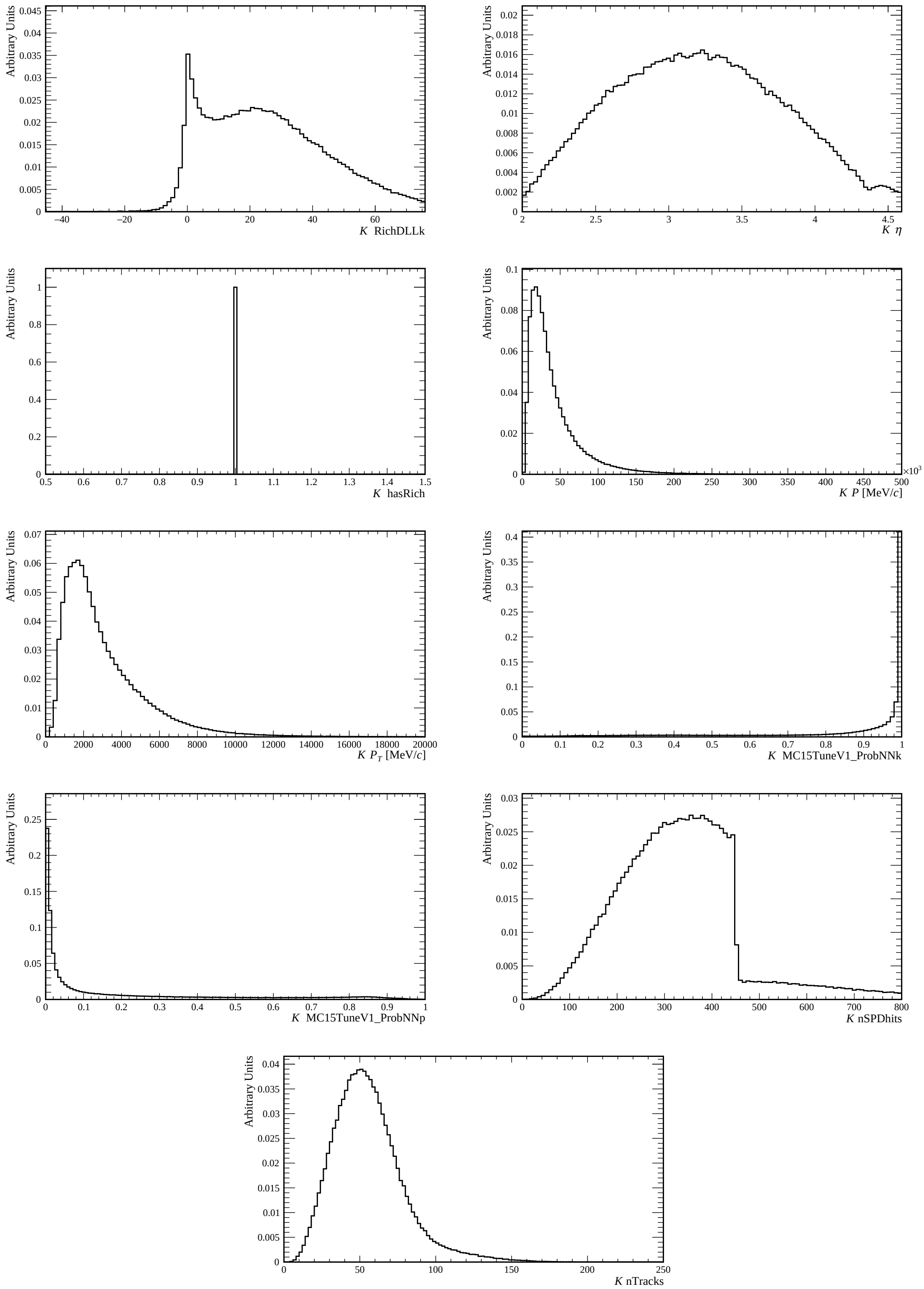

Figure A.19: PID variables used for the selection of kaon candidates in 2016.

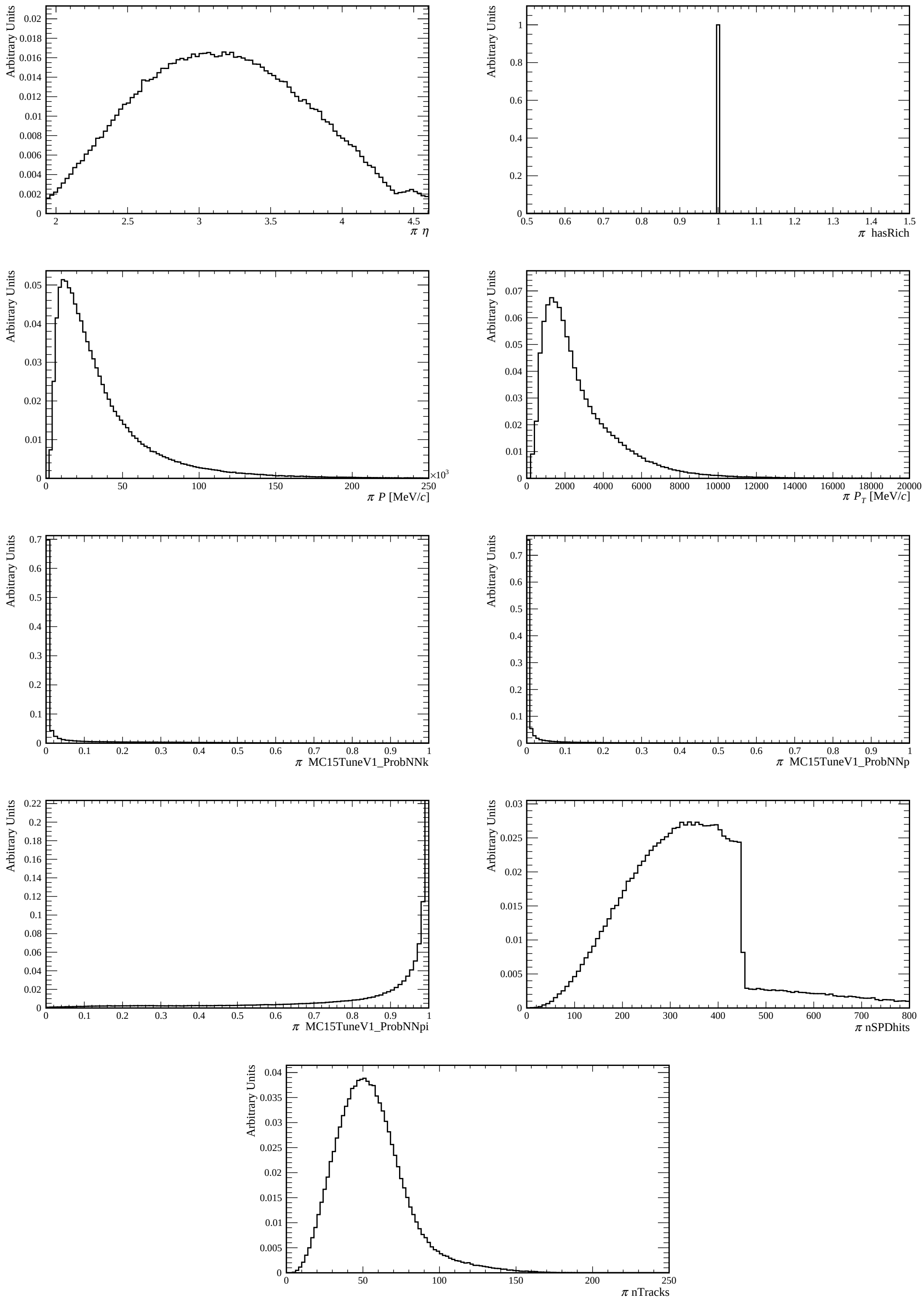

Figure A.20: PID variables used for the selection of pion candidates in 2016.

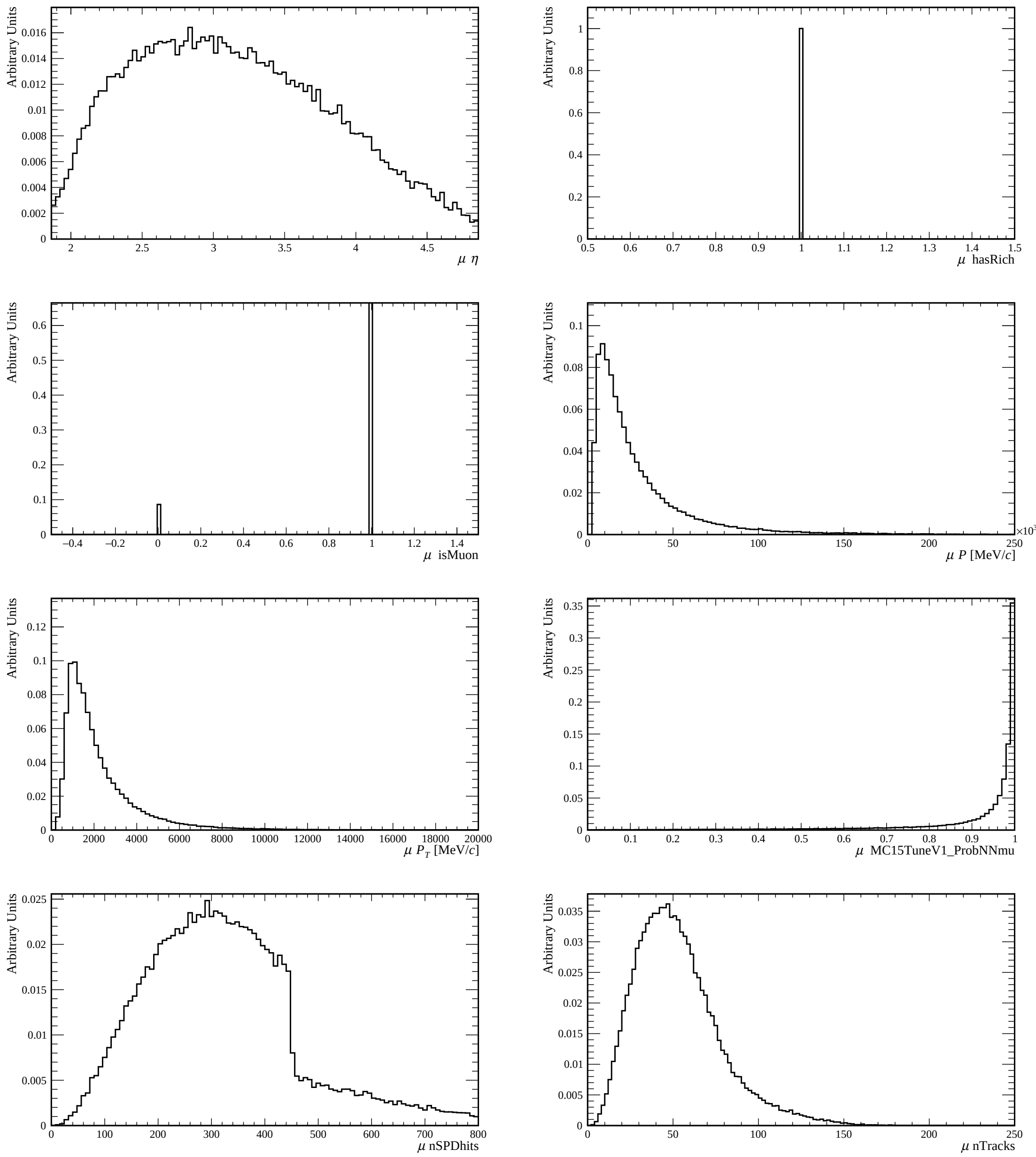

Figure A.21: PID variables used for the selection of muon candidates in 2016.

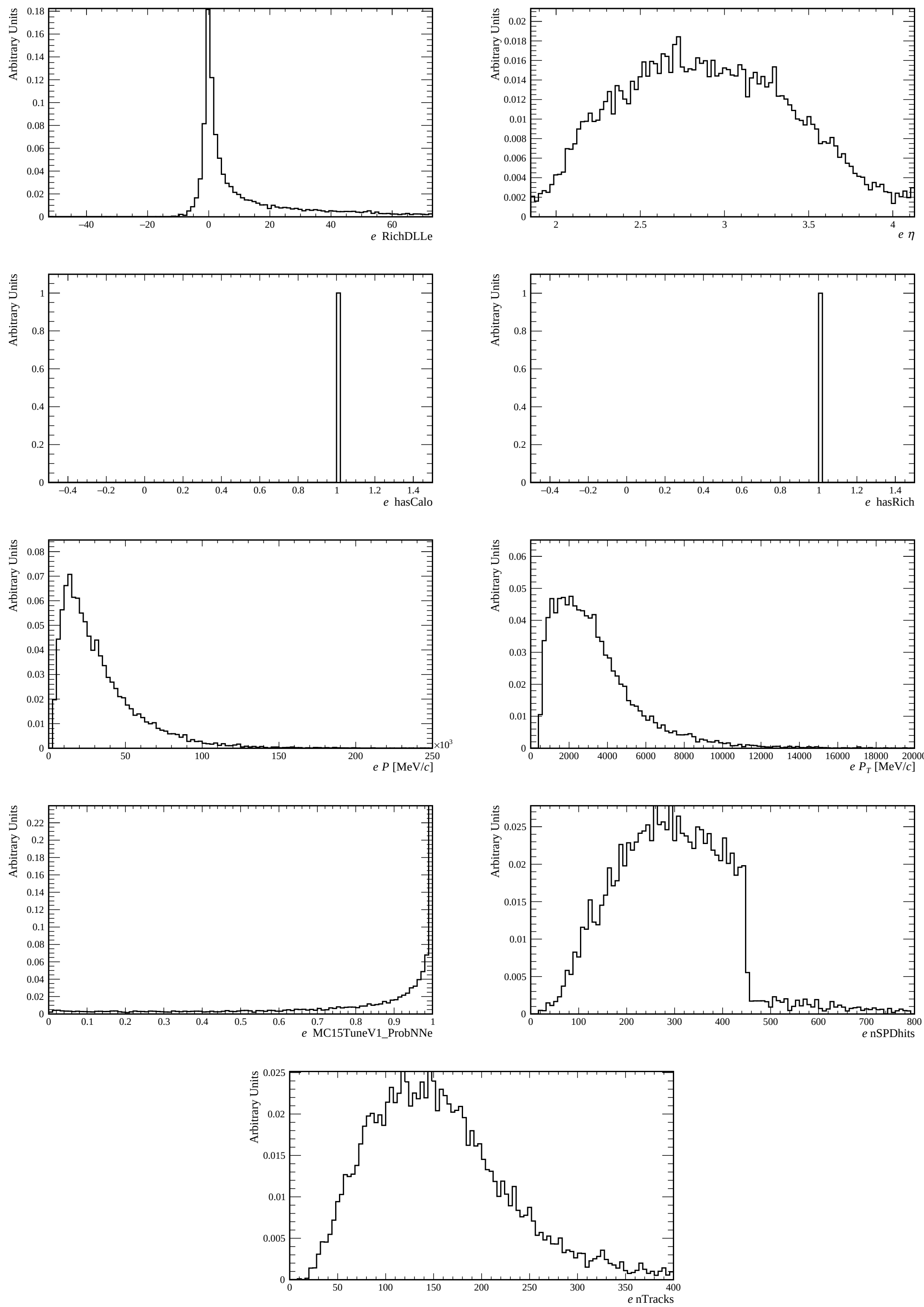

Figure A.22: PID variables used for the selection of electron candidates in 2016.

A.2.2 Efficiency plots for nSPDHits and nTracks

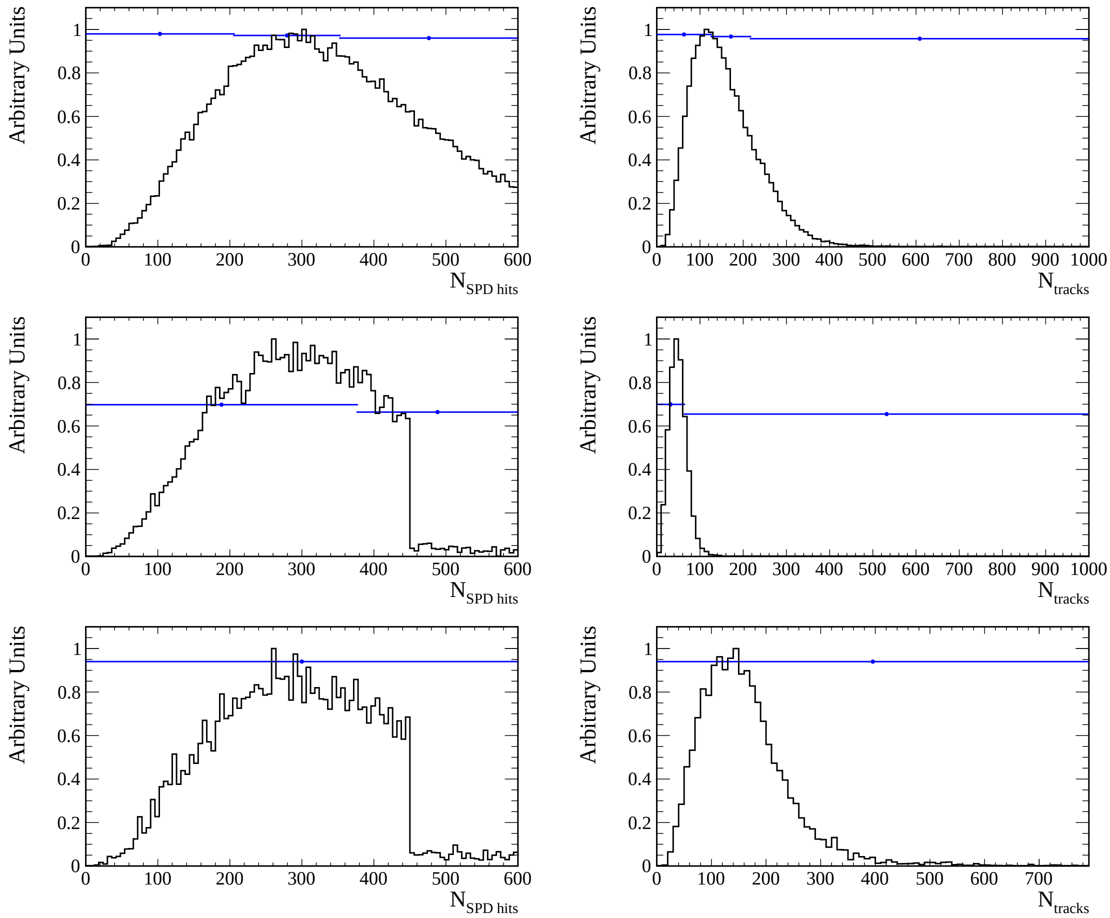

Figure A.23: PID efficiency for electron tracks as a function of the (left) nSPDHits and (right) nTracks. From top to bottom 2011 and 2012, 2015, and 2016.

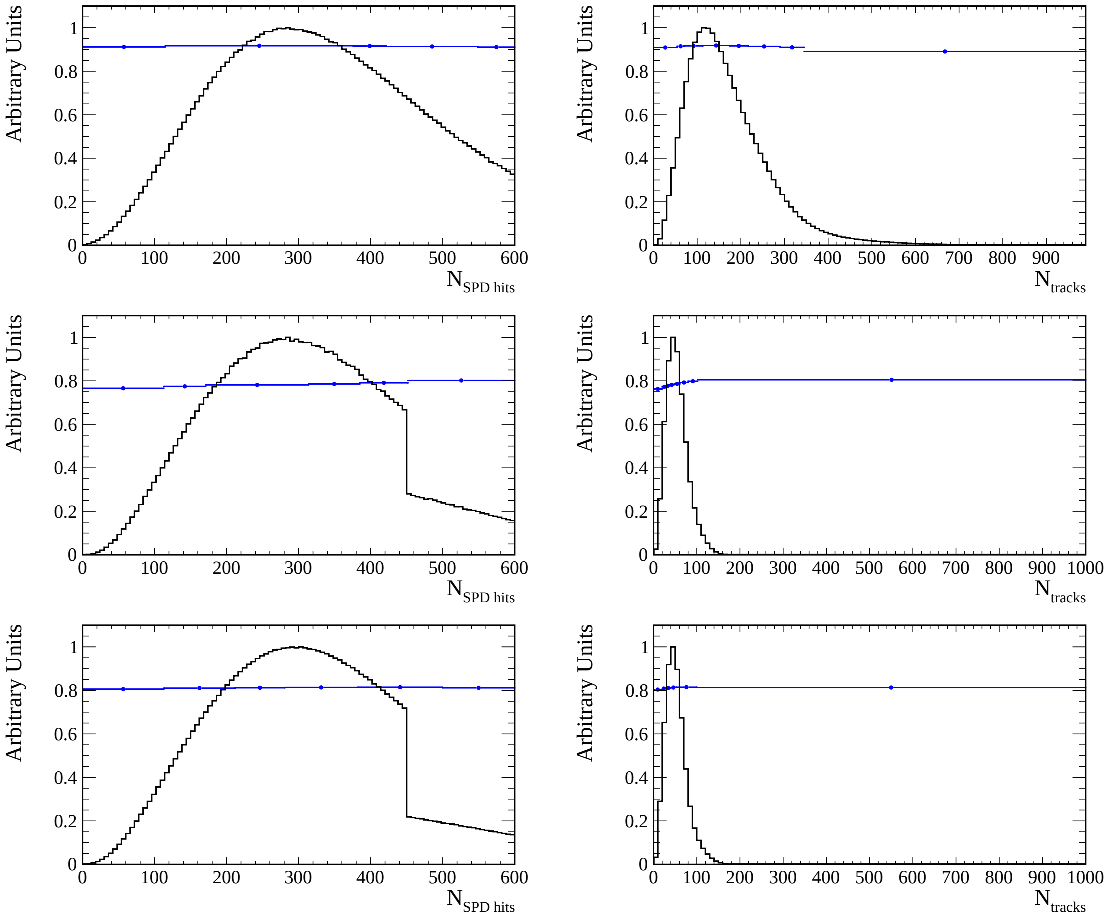

Figure A.24: PID efficiency for muon tracks as a function of the (left) nSPDHits and (right) nTracks. From top to bottom 2011 and 2012, 2015, and 2016.

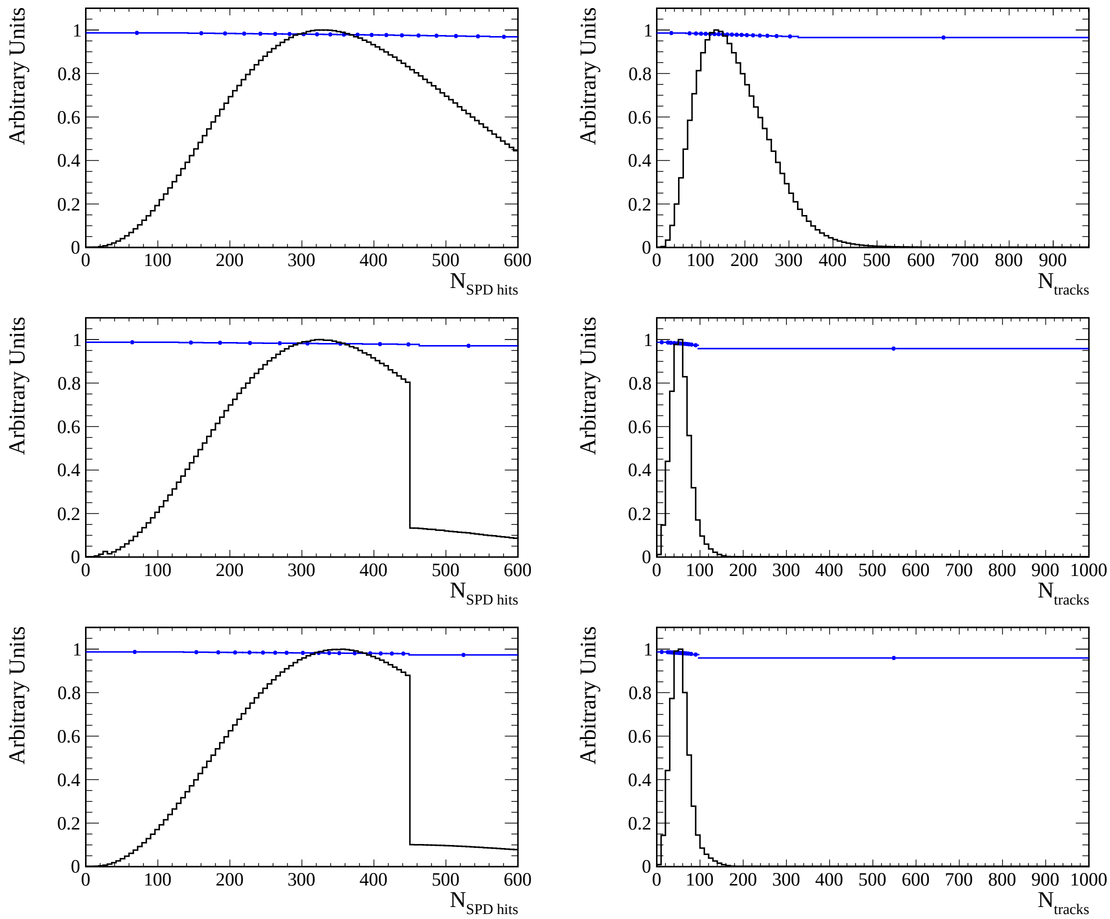

Figure A.25: PID efficiency for kaon tracks as a function of the (left) nSPDHits and (right) nTracks. From top to bottom 2011 and 2012, 2015, and 2016.

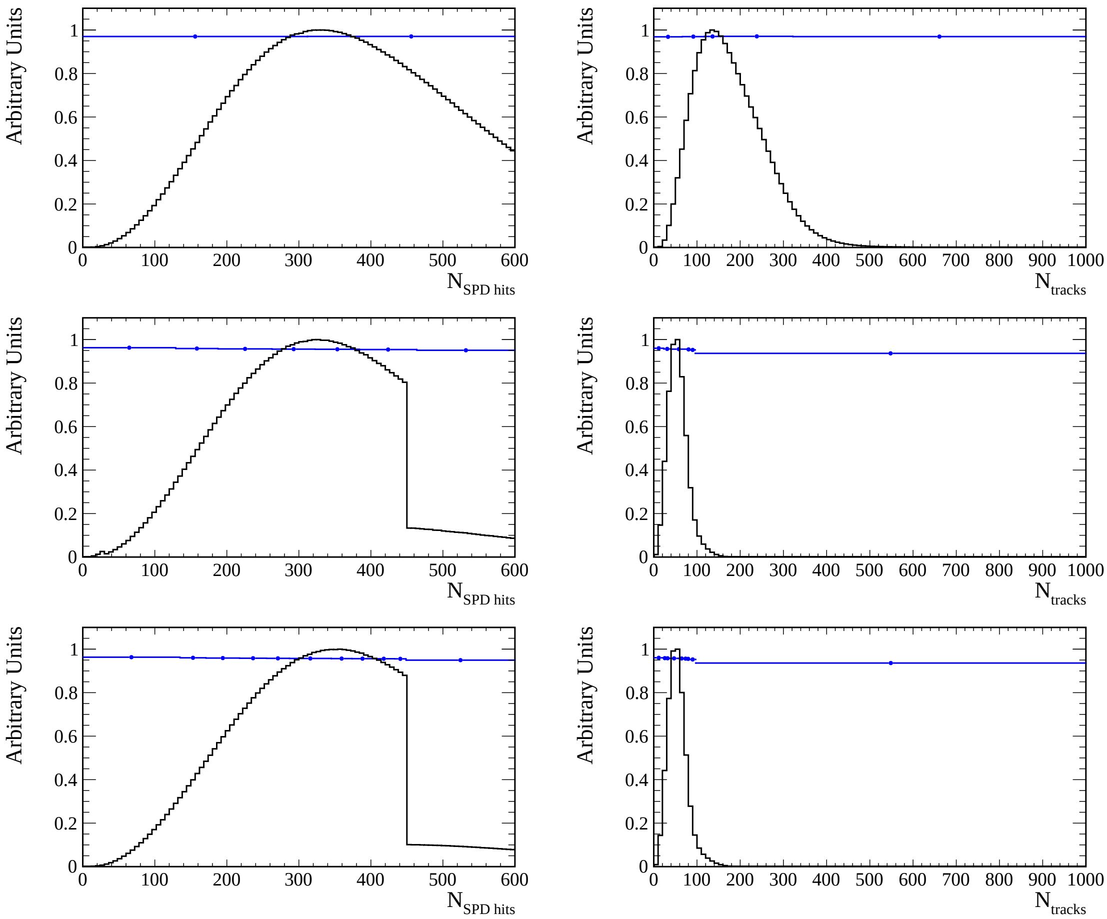

Figure A.26: PID efficiency for pion tracks as a function of the (left) nSPDHits and (right) nTracks. From top to bottom 2011 and 2012, 2015, and 2016.

Bibliography

[1] R. Aaij et al. (LHCb collaboration). "Measurement of *CP* violation in $B^0 \to J/\psi K^0_S$ and $B^0 \to \psi(2S) K^0_S$ decays". 2017. arXiv: `1709.03944`.

[2] R. Aaij et al. (LHCb collaboration). "Test of lepton universality with $B^0 \to K^{*0}\ \ell^+ \ell^-$ decays". In: *JHEP* 08 (2017), p. 55. DOI: `10.1007/JHEP08(2017)055`. arXiv: `1705.05802`.

[3] R. Aaij et al. (LHCb collaboration). "Test of lepton universality using $B^+ \to K^+\ \ell^+ \ell^-$ decays". In: *Phys. Rev. Lett.* 113 (2014), p. 151601. DOI: `10.1103/PhysRevLett.113.151601`. arXiv: `1406.6482`.

[4] M. E. Peskin and D. V. Schroeder. "An Introduction to quantum field theory". Reading, USA: Addison-Wesley, 1995. ISBN: 9780201503975. URL: `http://www.slac.stanford.edu/~mpeskin/QFT.html`.

[5] D. Griffiths. "Introduction to elementary particles". Weinheim, Germany, 2008. ISBN: 9783527406012.

[6] C. Laurent et al. "Matter and Antimatter in the Universe". In: *New J. Phys.* 14 (2012), p. 95012. DOI: `10.1088/1367-2630/14/9/095012`. arXiv: `1204.4186`.

[7] R. Aaij et al. (LHCb collaboration). "Observation of $J/\psi p$ resonances consistent with pentaquark states in $\Lambda^0_b \to J/\psi p K^-$ decays". In: *Phys. Rev. Lett.* 115 (2015), p. 72001. DOI: `10.1103/PhysRevLett.115.072001`. arXiv: `1507.03414`.

[8] P. W. Higgs. "Broken Symmetries and the Masses of Gauge Bosons". In: *Phys. Rev. Lett.* 13 (1964), p. 508. DOI: `10.1103/PhysRevLett.13.508`.

[9] C. Patrignani et al. (Particle Data Group). "Review of particle physics". In: *Chin. Phys.* C 40 (2016). and 2017 update. DOI: `10.1088/1674-1137/40/10/100001`.

[10] M. Kobayashi and T. Maskawa. "*CP*-Violation in the Renormalizable Theory of Weak Interaction". In: *Progr. Theor. Exp. Phys.* 49 (1973), p. 652. DOI: `10.1143/PTP.49.652`.

[11] D. Griffiths. "Introduction to elementary particles". Weinheim: Wiley-VCH, 2010.

[12] C. S. Wu et al. "Experimental test of parity conservation in beta decay". In: *Phys. Rev.* 105 (1957), p. 1413. DOI: `10.1103/PhysRev.105.1413`.

[13] J. H. Christenson et al. "Evidence for the 2π decay of the K^0_2 meson". In: *Phys. Rev. Lett.* 13 (1964), p. 138. DOI: `10.1103/PhysRevLett.13.138`.

[14] B. Aubert et al. (BaBar collaboration). "Measurement of *CP*-Violating Asymmetries in B^0 Decays to *CP* Eigenstates". In: *Phys. Rev. Lett.* 86 (2001), p. 251. DOI: `10.1103/PhysRevLett.86.2515`.

[15] A. Abashian et al. (Belle collaboration). "Measurement of the *CP* Violation Parameter $\sin 2\varphi_1$ in B_d^0 Meson Decays". In: *Phys. Rev. Lett.* 86 (2001), p. 2509. DOI: 10.1103/PhysRevLett.86.2509.

[16] G. C. Branco et al. "*CP* Violation". In: *Int. Ser. Monogr. Phys.* 103 (1999).

[17] M. S. Sozzi. "Discrete symmetries and CP violation: From experiment to theory". Oxford, UK, 2008. ISBN: 9780199655427.

[18] J. Charles et al. "*CP* violation and the CKM matrix: assessing the impact of the asymmetric B factories (and online update)". In: *Eur. Phys. J. C* 41 (2005), p. 1. DOI: 10.1140/epjc/s2005-02169-1.

[19] S. Faller et al. "The golden modes $B^0 \to J/\psi K^0_{\mathrm{S,L}}$ in the era of precision flavour physics". In: *Phys. Rev.* D79 (2008), p. 14030. DOI: 10.1103/PhysRevD.79.014030. arXiv: 0809.0842.

[20] M. Jung. "Determining weak phases from $B \to J/\psi P$ decays". In: *Phys.Rev.* D86 (2012), p. 53008. DOI: 10.1103/PhysRevD.86.053008. arXiv: 1206.2050.

[21] R. Fleischer. "Penguin effects in $\phi_{d,s}$ determinations". 2012. arXiv: 1212.2792.

[22] Y. Amhis et al. "Averages of b-hadron, c-hadron, and τ-lepton properties as of summer 2016". 2016. arXiv: 1612.07233.

[23] B. Aubert et al. (BaBar collaboration). "Measurement of Time-Dependent *CP* Asymmetry in $B^0 \to c\bar{c}K^{(*)0}$ Decays". In: *Phys. Rev.* D79 (2009), p. 72009. DOI: 10.1103/PhysRevD.79.072009. arXiv: 0902.1708.

[24] I. Adachi et al. (Belle collaboration). "Precise measurement of the *CP* violation parameter $\sin 2\phi_1$ in $B^0 \to (c\bar{c})K^0$ decays". In: *Phys.Rev.Lett.* 108 (2012), p. 171802. DOI: 10.1103/PhysRevLett.108.171802. arXiv: 1201.4643.

[25] R. Aaij et al. (LHCb collaboration). "Measurement of *CP* violation in $B^0 \to J/\psi K^0_{\mathrm{S}}$ decays". In: *Phys. Rev. Lett.* 115 (2015), p. 31601. DOI: 10.1103/PhysRevLett.115.031601. arXiv: 1503.07089.

[26] S. L. Glashow et al. "Weak Interactions with Lepton-Hadron Symmetry". In: *Phys. Rev. D* 2 (1970), p. 1285. DOI: 10.1103/PhysRevD.2.1285.

[27] W. Altmannshofer et al. "Interpreting Hints for Lepton Flavor Universality Violation". In: *Phys. Rev.* D96 (2017), p. 55008. DOI: 10.1103/PhysRevD.96.055008. arXiv: 1704.05435.

[28] G. Hiller et al. "More model-independent analysis of $b \to s$ processes". In: *Phys. Rev.* D69 (2004), p. 74020. DOI: 10.1103/PhysRevD.69.074020. arXiv: hep-ph/0310219.

[29] M. Bordone et al. "On the Standard Model predictions for R_K and R_{K^*}". In: *Eur. Phys. J.* C76 (2016), p. 440. DOI: 10.1140/epjc/s10052-016-4274-7. arXiv: 1605.07633.

[30] W. Altmannshofer et al. "Quark flavor transitions in $L_\mu - L_\tau$ models". In: *Phys. Rev. D* 89 (2014), p. 95033. DOI: 10.1103/PhysRevD.89.095033.

[31] B. Gripaios et al. "Composite leptoquarks and anomalies in B-meson decays". In: *JHEP* 2015 (2015), p. 6. DOI: 10.1007/JHEP05(2015)006.

[32] S. Descotes-Genon et al. “Global analysis of $b \to s\ell\ell$ anomalies”. In: *JHEP* 06 (2016), p. 92. DOI: 10.1007/JHEP06(2016)092. arXiv: 1510.04239.

[33] B. Capdevila et al. “Hadronic uncertainties in $B \to K^*\mu^+\mu^-$: a state-of-the-art analysis”. In: *JHEP* 04 (2017), p. 16. DOI: 10.1007/JHEP04(2017)016. arXiv: 1701.08672.

[34] B. Capdevila et al. “Assessing lepton-flavour non-universality from $B \to K^*\ell\ell$ angular analyses”. In: *JHEP* 10 (2016), p. 75. DOI: 10.1007/JHEP10(2016)075. arXiv: 1605.03156.

[35] N. Serra et al. “Measuring the breaking of lepton flavor universality in $B \to K^*\ell^+\ell^-$”. In: *Phys. Rev.* D95.3 (2017), p. 35029. DOI: 10.1103/PhysRevD.95.035029. arXiv: 1610.08761.

[36] D. van Dyk et al. “EOS (”delta456” release)”. 2016. DOI: 10.5281/zenodo.159680. URL: https://doi.org/10.5281/zenodo.159680.

[37] A. Bharucha et al. “$B \to V\ell^+\ell^-$ in the Standard Model from light-cone sum rules”. In: *JHEP* 08 (2016), p. 98. DOI: 10.1007/JHEP08(2016)098. arXiv: 1503.05534.

[38] W. Altmannshofer et al. “Status of the $B \to K^*\mu^+\mu^-$ anomaly after Moriond 2017”. In: *Eur. Phys. J.* C77.6 (2017), p. 377. DOI: 10.1140/epjc/s10052-017-4952-0. arXiv: 1703.09189.

[39] D. Straub et al. “flav-io/flavio v0.19”. 2017. DOI: 10.5281/zenodo.292991. URL: https://doi.org/10.5281/zenodo.292991.

[40] S. Jäger et al. “Reassessing the discovery potential of the $B \to K^*\ell^+\ell^-$ decays in the large-recoil region: SM challenges and BSM opportunities”. In: *Phys. Rev.* D93 (2016), p. 14028. DOI: 10.1103/PhysRevD.93.014028. arXiv: 1412.3183.

[41] A. Augusto Alves Jr. et al. (LHCb collaboration). “The LHCb detector at the LHC”. In: *J. Instrum.* 3 (2008), p. 8005. DOI: 10.1088/1748-0221/3/08/S08005.

[42] R. Aaij et al. (LHCb collaboration). “LHCb Detector Performance”. In: *Int. J. Mod. Phys.* A30 (2015), p. 1530022. DOI: 10.1142/S0217751X15300227. arXiv: 1412.6352.

[43] L. Evans et al. “LHC Machine”. In: *J. Instrum.* 3 (2008), p. 8001. URL: http://stacks.iop.org/1748-0221/3/i=08/a=S08001.

[44] O. S. Brüning et al. “LHC Design Report”. CERN Yellow Reports: Monographs. CERN, 2004. URL: https://cds.cern.ch/record/782076.

[45] G. Rumolo et al. “LHC experience with different bunch spacings in 2011 (25 , 50 and 75 ns)”. In: *Proceedings of Workshop on LHC performance* (2012), p. 89. URL: https://cds.cern.ch/record/1492581.

[46] G. Aad et al. (ATLAS collaboration). “Observation of a new particle in the search for the Standard Model Higgs boson with the ATLAS detector at the LHC”. In: *Phys. Lett.* B716 (2012), p. 1. DOI: 10.1016/j.physletb.2012.08.020. arXiv: 1207.7214.

[47] S. Chatrchyan et al. (CMS collaboration). “Observation of a new boson at a mass of 125 GeV with the CMS experiment at the LHC”. In: *Phys. Lett.* B716 (2012), p. 30. DOI: 10.1016/j.physletb.2012.08.021. arXiv: 1207.7235.

[48] CERN Technology Department. 2017. URL: http://te-dep-epc-oms.web.cern.ch/te-dep-epc-oms/operation-en/operation.stm.

[49] LHCb collaboration. "$b\bar{b}$ production angle plots". 2014. URL: http://lhcb.web.cern.ch/lhcb/speakersbureau/html/bb_ProductionAngles.html.

[50] G. Barrand et al. "GAUDI — A software architecture and framework for building HEP data processing applications". In: *Comput. Phys. Commun.* 140 (2001), p. 45. DOI: http://dx.doi.org/10.1016/S0010-4655(01)00254-5.

[51] "The MOORE Project". 2017. URL: http://lhcb-release-area.web.cern.ch/LHCb-release-area/DOC/moore/.

[52] "The BRUNEL Project". 2017. URL: http://lhcb-release-area.web.cern.ch/LHCb-release-area/DOC/brunel/.

[53] "The DAVINCI project". 2017. URL: http://lhcb-release-area.web.cern.ch/LHCb-release-area/DOC/davinci/.

[54] R. Brun and F. Rademakers. "ROOT: An object oriented data analysis framework". In: *Nucl. Instrum. Meth.* A389 (1997), p. 81. DOI: 10.1016/S0168-9002(97)00048-X.

[55] W. Verkerke et al. "The ROOFIT Toolkit for Data Modeling". 2017. URL: http://roofit.sourceforge.net.

[56] "The GAUSS Project". 2017. URL: http://lhcb-release-area.web.cern.ch/LHCb-release-area/DOC/gauss/.

[57] D. J. Lange. "The EvtGen particle decay simulation package". In: *Nucl. Instrum. Meth.* A462 (2001), p. 152. DOI: 10.1016/S0168-9002(01)00089-4.

[58] T. Sjöstrand et al. "PYTHIA 6.4 physics and manual". In: *JHEP* 2006 (2006), p. 26. DOI: 10.1088/1126-6708/2006/05/026. arXiv: hep-ph/0603175.

[59] S. Agostinelli et al. "GEANT4 — a simulation toolkit". In: *Nucl. Instrum. Methods. Phys. Res. A* 506 (2003), p. 250. DOI: http://dx.doi.org/10.1016/S0168-9002(03)01368-8.

[60] "The BOOLE Project". 2017. URL: http://lhcb-release-area.web.cern.ch/LHCb-release-area/DOC/boole/.

[61] R. Aaij et al. (LHCb collaboration). "B flavour tagging using charm decays at the LHCb experiment". In: *JINST* 10 (2015), p. 10005. DOI: 10.1088/1748-0221/10/10/P10005. arXiv: 1507.07892.

[62] R. Aaij et al. (LHCb collaboration). "New algorithms to tag the flavour of B^0 mesons using pions and protons". In: *Eur. Phys. J.* C77.4 (2016), p. 238. DOI: 10.1140/epjc/s10052-017-4731-y. arXiv: 1610.06019.

[63] R. Aaij et al. (LHCb collaboration). "Opposite-side flavour tagging of B mesons at the LHCb experiment". In: *Eur. Phys. J.* C72 (2012), p. 2022. DOI: 10.1140/epjc/s10052-012-2022-1. arXiv: 1202.4979.

[64] LHCb collaboration. "Flavour Tagging Schemes". URL: https://twiki.cern.ch/twiki/bin/viewauth/LHCb/SBpublic.

[65] L. Breiman et al. "Classification and regression trees". Belmont, California, USA: Wadsworth International Group, 1984.

[66] J. Wimberley (LHCb collaboration). "Calibrating flavor tagging algorithms with binomial regression". 2017. URL: https://cds.cern.ch/record/2242398.

[67] M. Pivk et al. "splot: A statistical tool to unfold data distributions". In: *Nucl. Instrum. Meth.* A555 (2005), p. 356. DOI: 10.1016/j.nima.2005.08.106. arXiv: physics/0402083.

[68] W. D. Hulsbergen. "Decay chain fitting with a Kalman filter". In: *Nucl. Instrum. Meth.* A552 (2005), p. 566. DOI: 10.1016/j.nima.2005.06.078. arXiv: physics/0503191.

[69] F. Pedregosa et al. "Scikit-learn: Machine Learning in Python". In: *J. Mach. Learn. Res.* 12 (2011), p. 2825.

[70] R. E. Schapire et al. "A decision-theoretic generalization of online learning and an application to boosting". In: *Jour. Comp. and Syst. Sc.* 55 (1997), p. 119. DOI: 10.1006/jcss.1997.1504.

[71] D. M. Santos et al. "Mass distributions marginalized over per-event errors". In: *Nucl. Instrum. Meth.* A764 (2014), p. 150. DOI: 10.1016/j.nima.2014.06.081. arXiv: 1312.5000.

[72] A. Rogozhnikov. "Reweighting with Boosted Decision Trees". In: *J. Phys. Conf. Ser.* 762 (2016), p. 12036. DOI: 10.1088/1742-6596/762/1/012036. arXiv: 1608.05806.

[73] R. Barlow. "Systematic errors: facts and fictions". 2002. arXiv: hep-ex/0207026.

[74] S. Tolk et al. "Data driven trigger efficiency determination at LHCb". 2014. URL: https://cds.cern.ch/record/1701134.

[75] O. Lupton et al. (LHCb collaboration). "Calibration samples for particle identification at LHCb in Run 2". 2016. URL: https://cds.cern.ch/record/2134057.

[76] L. Anderlini et al. (LHCb collaboration). "Computing strategy for PID calibration samples for LHCb Run 2". 2016. URL: https://cds.cern.ch/record/2199780.

[77] L. Anderlini et al. (LHCb collaboration). "The PIDCalib package". 2016. URL: https://cds.cern.ch/record/2202412.